Aerothermal Performance Analysis of Hypersonic Waverider Configurations for Rapid Interplanetary Transit Missions

a project presented to
The Faculty of the Department of Aerospace Engineering
San José State University

in partial fulfillment of the requirements for the degree
Master of Science in Aerospace Engineering

by

Christopher W. Crews-Holloway

May 2024

approved by

Dr. Periklis Papadopoulos
Faculty Advisor

Abstract

A conceptual study was conducted on the aerothermodynamic performance of various waverider geometries supporting an aero-gravity assist (AGA) trajectory maneuver. A reference trajectory with fixed aero-coefficients was provided for an Earth AGA mission which implied major transit time reductions to distant bodies in the outer solar system. This report considers the design, analysis process, and performance of four different waverider aeroshell configurations capable of supporting a useful spacecraft payload for reduced transit times to distant bodies in the outer solar system. Aerodynamic performance and heating is analyzed along different points of the AGA trajectory for various configurations with use of NASA's Configuration Based Aerodynamics software. This analysis shows waverider configuration performance and provides insights to the feasibility of the maneuver in Earth's atmosphere for transit reduction. The aerodynamic performance results for the four waveriders are be discussed in detail, and findings showed the elliptical configuration had the best aerothermal performance of all waverider configurations considered in this report. The elliptical waverider aeroshell with a nose radii of $R_n = 0.1$ had the lowest C_D, which lead to the highest L/D performance at over 1.5. This peak performance occurred at an AoA above 5° through a value of 20°. Convective heat rate dominated on the elliptical configuration, and total heat flux proved to be lower by more than 850 W/cm^2, with a value of roughly 5365 W/cm^2. Rectangular nose configurations had slight discrepancies in performance and higher heating levels than the elliptical configurations. Results indicated that Earth AGA should be feasible to provide large transit time reductions to interplanetary destinations, but high fidelity tools are required to confirm this assumption.

Acknowledgments

I would like to acknowledge Dr. Periklis Papadopoulos for his advice on this project and for his close guidance during my time at San Jose State University. It has been an honor to work directly with Dr. Papadopoulos and to learn from his expertise across many disciplines as an Aerospace Engineering graduate student over the past two years.

The inspiration for this Master's project came from the opportunity of working with Analytical Mechanics Associates, Inc. as an Aerothermal Analyst supporting aeroshell design and simulations of hypersonic flight environments for an AGA trajectory maneuver to a distant planetary object. I would like to acknowledge Jim Arnold, former NASA Ames Thermal Protection Systems division chief and ESTRAD Project Manager Dave Cornelius for their invaluable support during this project. Their insights and expertise on space mission design for AGA trajectories, orbital mechanics, and thermal protection systems. Their guidance and the continued opportunity to work with industry experts at NASA Ames and Analytical Mechanics Associates, Inc has provided incredible insights to the mission design process and driven academic growth.

I would like to acknowledge Dr. Dave Kinney of NASA Ames for his advice on the Gmsh workflow, mesh sizing, physics assumptions, and limitations of the Configuration Based Aerodynamics software utilized for project analysis. I would like to further acknowledge research scientists Dr. Dinesh Prabhu and Dr. David Saunders of NASA Ames for their time supporting verification and validation of CBAERO results with high fidelity CFD simulations. Dr. Prabhu and Dr. Saunders provided incredible feedback to the mesh refinement process, aerothermodynamic design considerations, verification and validation of simulation results, as well as the sizing of thermal protection systems for hypersonic vehicles and re-entry systems. I would additionally like to acknowledge Dr. Gary Allen for his time and shared expertise on the subjects of orbital mechanics, interplanetary trajectories, and thermal protection system design process. It has been an honor to work with and learn from top tier experts in industry.

I would like to thank fellow San Jose State Aerospace Master's student Anton Kulinich for his guidance on data post-processing with Python, expertise with Genesis Flight Mechanics Simulation and Trajectory software, and his knowledge with scientific computing in the Linux environment. I would also like to thank Aerospace Master's student Travis George for advice with Solidworks to create watertight surface features and providing insight on best practices for rapid model parameterization.

Table of Contents

List of Tables

List of Figures

Nomenclature

B	Inverse scale height of atmosphere
C_D	Coefficient of drag
C_L	Coefficient of lift
C_m	Coefficient of pitching moment
C_P	Coefficient of pressure
c_p	Specific heat at constant pressure
c_v	Specific heat at constant volume
L/D	Lift-to-drag ratio
Re	Reynolds number
R_n	Nose bluntness radii
K	Atmosphere dependant radiative heat constant
K_n	Knudsen Number
p	Static pressure
q_∞	Dynamic pressure
$\dot{q}_{\text{conv}}$	Convective heating
$\dot{q}_{\text{rad}}$	Radiative heating
h	Enthalpy
$\hat{n}$	Normal unit vector
R	Universal gas constant
S	Reference area
T	Temperature
$V_{s/c}$	Heliocentric velocity of spacecraft
V_p	Heliocentric velocity of planet
$V_{\infty 1}$	Hyperbolic velocity, approach of spacecraft
$V_{\infty 2}$	Hyperbolic velocity, exit of spacecraft
ΔV_∞	Change in velocity due to atmospheric drag
V_{pr}	Velocity, propulsive burn
α	Angle of attack
β	Shock angle
ρ	Density
ε	Emissivity
μ	Viscosity
γ	Ratio of specific heats
λ	Mean free path
σ	Stefan-Boltzmann constant
ν	Prandtl-Meyer function
θ	Shock deflection angle
Θ	Turn angle through atmospheric flight
Φ	Total AGA turn angle

Acronyms

ADB	Aerodatabase
AGA	Aerogravity assist
AMA	Analytical Mechanics Associates, Inc.
AoA	Angle of attack
MAnE	Mission Analysis Environment
C3	Characteristic launch energy
CAD	Computer aided design
CBAERO	Configuration Based Aerodynamics
CFD	Computational fluid dynamics
CG	Center of gravity
DAC	Direct Simulation Monte Carlo Analysis Code
DLPR	Data Parallel Line Relaxation Code
DSMC	Direct Simulation Monte Carlo
HEEET	Heatshield for Extreme Entry Environments Technology
FMF	Free molecular flow
GA	Gravity assist
LEO	Low earth orbit
NEQAIR	Nonequilibrium Radiative Transport and Spectra Program
OML	Outer mold line
SHARP-L1	Slender Hypervelocity Aerothermodynamic Research Probe - Lifting Entry 1
TNO	Trans-Neptunian object
TRAJ	The Trajectory Program
TRL	Technology readiness level
TPS	Thermal protection system
UHTC	Ultra-high temperature ceramics
1D	One dimensional
2D	Two dimensional
3D	Three dimensional

Chapter 1: Introduction

1.1 Purpose

The design of low cost systems supporting mobility to, through, and from space is required to enhance our understanding of the solar system. As early as 2025, the Artemis Missions are set to enable human return to the moon for the first time in more than fifty years, with goals to enable human expansion across the solar system. This exciting vision comes with a steep cost, as NASA is projecting to spend $93 billion USD on the Artemis efforts from FY2012 through FY2025. The cost of an Artemis launch projects to be $4.1 billion for a single flight cadence per year, highlighting the importance of affordable space access [1]. A sustainable long term exploration plan is required to pave the way for future manned mission as humans plan to explore the celestial bodies beyond Earth.

In the present day, humans have many unanswered questions about our origin story, the solar system, and our galactic surroundings. Scientists and astronomers are actively seeking to answer if we are alone in this universe, as the search continues for signatures of life and clues which might imply the existence of biological organisms outside of planet Earth. These answers are readily obtainable, yet depend on a deeper understanding of the other planets, moons, and distant bodies in our solar system. Deep space exploration is an effective method humans can use to better understand the distant worlds around us [2], but limited headway has been made finding concise conclusions due to excessive costs, launch vehicle constraints, and transit time requirements associated with space access and interplanetary travel.

To promote space exploration and better understanding of our surroundings, strides must be made to improve the reusability of launch and space transportation systems in an efficient, cost effective manner. Earth's atmospheric hypersonic flight environment, vehicle design requirements, and the implementation of trajectory maneuvers must be closely understood to reduce transit times to distant planetary bodies. The reference trajectory used for analysis indicated a transit time reduction of 7 years to the dwarf planet of Haumea, one of the fastest spinning large objects in our solar system [3].

The purpose of this project is to complete a conceptual level aero-thermodynamic analysis upon waverider aeroshell configurations as they undergo hypersonic re-entry flight conditions during in atmosphere trajectory maneuvers known as aerogravity assist (AGA). This trajectory concept has been researched for decades, and when blended with propulsive maneuvers, it can significantly reduce transit times for missions to distant bodies in our Solar System like Pluto or Trans Neptunian Objects (TNOs). Understanding the relationships between vehicle aero-thermodynamics in the atmosphere is crucial to design reusable, robust vehicles that could enable lower cost space access and planetary exploration.

For successful interplanetary transit missions, two of the most critical aspects of the mission design are the ability maximize velocity and minimize mass. Implementation

of low cost transfer maneuvers can often reflect mission superiority and cost savings [2]. If a waverider design is optimized for the in-atmospheric flight conditions present during AGA maneuvers, it will enable faster transit opportunities that do not currently exist with gravity assist trajectories maneuvers and present launch vehicle capabilities. This technique has a significant payoff for high energy missions to outer planets, as it significantly reduces the flight duration and eliminates additional propulsive requirements for orbital insertions [4]. This project will focus on the engineering design process of waverider aeroshell configurations and provide conceptual aero-thermal results of four hypersonic waveriders configurations. The goal of this project is understand critical aspects of waverider design and analyze the feasibility of the AGA maneuver in Earth's atmosphere to help lay the groundwork for rapid solar system travel.

1.2 Motivation

For efficient exploration of our own solar system, we need low cost access to space. Unfortunately, the lack of reusability with our launch vehicles and spacecraft systems drive costs to excessive heights while hindering high cadence, flexible operations. As SpaceX has made impressive strides for reusability in the launch industry by landing their first stage, the second stage of current vehicle architecture is discarded in space producing orbital debris after completion of the specified mission.

Critical limiting factors affecting space access are cost, volume, and weight as payloads are constrained by the nose cone fairing and performance of the launch vehicle. The characteristic energy (C3) of a launch vehicle determines its propulsive capability, influencing the spacecraft's trajectory and the energy it will require to reach specific orbits and interplanetary destinations. These limitations impact the overall mission design requirements of the spacecraft system, influencing factors like the payload weights, sizing, and propulsive capabilities. As a spacecraft embarks on its journey through the solar system, flight with traditional chemical based propulsion systems will require long transit times to distant bodies in our solar system. The transit time constraint coupled with the limiting factors of space access hamper research and current understanding of the phenomena in our surrounding universe.

These limitations motivated a deeper analysis into the design considerations of reusable vehicles for space access that utilize trajectory maneuvers to reduce transit time. System reusability coupled with reduced transit times will better enable more efficient space missions at lower costs. Aerodynamic and aero-thermodynamic performance of the waverider configurations are of utmost importance to this study, and will be explored for hypersonic atmospheric flight supporting AGA trajectories. This will allow for the discussion of conceptual results to better inform waverider design recommendations and future research given current launch vehicle constraints and advancements in thermal protection systems (TPS).

The environmental challenges presented with AGA trajectory conditions are critical for setting feasible baseline vehicle requirements and determining system design. Knowledge of the design and engineering analysis process of hypersonic waverider vehicle configurations for atmospheric flight on Earth will enable a more comprehensive understanding of distant bodies in our solar system. If waverider configurations are optimized to survive AGA flight conditions, fast interplanetary transit will be enabled to support scientific research and human understanding of our surroundings.

1.3 Proposed Objectives

To complete the proposed scope of work, a detailed background on the aero-thermodynamic conditions present during AGA trajectory maneuvers and hypersonic atmospheric flight is needed to ensure concept feasibility. The equations governing these topics will be discussed in detail in the mathematical model section of this report. The critical design parameters required to drive optimization of waverider aeroshell configurations are presented. The influence of these parameters on hypersonic flight performance while sustaining survivable heating conditions are of utmost interest to understand the feasibility of AGA trajectory maneuvers. Quantitative results regarding these trade offs are provided and discussed.

To accomplish the proposed conceptual analysis, four different waverider configurations are considered at four different nose bluntness values. Each model starts from a similar dimensioned wedge-cone geometry with a variable nose bluntness range from 0.1 m to 0.25 m in 50 mm increments. Computational studies are implemented to investigate two waverider aeroshell nose configurations; rectangular and elliptical. Two additional trim configurations are considered for the rectangular nose vehicle. These four waverider configurations are studied computationally across the specified nose bluntness range to understand trends of drag losses vs heating of the aeroshell undergoing the AGA trajectory maneuver. Results for the variation in performance of the configurations are explored for the expected flight conditions at points along a reference AGA trajectory. Trends in performance and variation across the configurations are discussed, and recommendations are provided for future work.

1.4 Literature Review

To achieve proposed objectives with this project, a detailed literature review of the AGA trajectory maneuver, hypersonic aero-thermodynamics, considerations for the aerothermal design of waverider aeroshells, and thermal protection systems is required to better understand the theoretical design framework for the waverider aeroshell undergoing an atmospheric trajectory maneuver.

1.4.1 The Aero-gravity Assist Trajectory Maneuver

The AGA trajectory maneuver is known to reduce interplanetary transit times, acting to optimize the change in velocity, Δv, obtained by a flyby of a celestial body with an atmosphere to minimize the flight duration of the mission at hand. This maneuver has the potential to yield a much higher Δv and turn angle than a pure planetary gravity assist trajectory maneuver, offering more flexible mission design. Utilization of an AGA maneuver allows for deep space exploration at low launch energy and short flight times. Multiple planetary AGA flybys can be used in single mission, allowing for extremely fast missions that require low launch energies [5].

Gravity assist (GA) maneuvers are a common practice to reduce transit time and propellant mass requirements for interplanetary missions [6]. However, there are limitations to how sharp the trajectory can bend around the given planet, which ultimately constrains the outbound Δv of the spacecraft. GA maneuvers change the spacecraft velocity as they pass by celestial bodies, as the gravitational field from the body influ-

ences the spacecraft's speed. However, for planets besides Jupiter and Saturn, there will only be a small change in Δv of the spacecraft from a gravity assisted maneuver [7]. Propulsive assistance can support both GA and AGA assisted trajectories as an energy recovery burn, acting to improve efficiency of the maneuver with a propulsive burn to increase the outbound Δv of the spacecraft during a planetary flyby. The fundamental difference seen with aero-gravity assist technique when compared to traditional gravity assist trajectories is the spacecraft enters the planetary atmosphere of the body upon its hyperbolic approach and exits the atmosphere to a modified hyperbolic trajectory relative to the planetary body [8]. The lift vector of the vehicle must point downwards towards the planet so the body can dive inside the atmosphere to optimize the turn angle and exit velocity during the maneuver. The AGA trajectory is a possible solution to increase the efficiency of traditional GA maneuvers if the mission passes a planetary body with an atmosphere. The differences in these trajectory maneuvers can be seen in Fig. 1.1

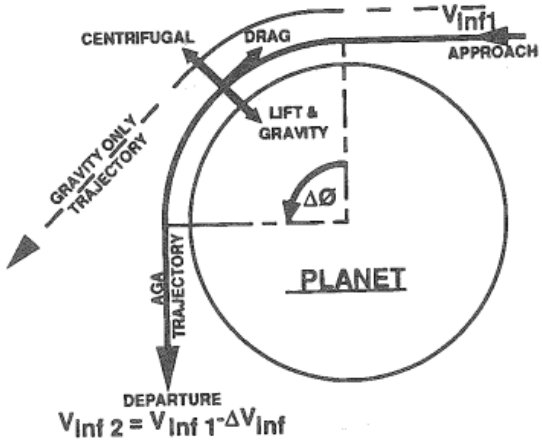

Figure 1.1: Comparison of an aero-gravity assist maneuver to a gravity assist maneuver [4].

As implementation of single or multiple AGA maneuvers are quite advantageous to enable shorter time of flight, there are critical challenges that still must be overcome for feasible implementation. The high incoming flow velocity involved with AGA missions translates to high acceleration and heating loads on the spacecraft [5]. As the vehicle engages in an atmospheric flyby at hypersonic velocities, some of the kinetic energy is dissipated into heat. The heating rate and subsequent total heat load are critical mission aspects, and depend on how deep the vehicle flies through the atmosphere [9].

Atmospheric depth and time of flight influence are critical to understanding the aerothermal environmental conditions experienced by the aeroshell during the AGA maneuver. Constraints for the thermal environment like peak stagnation heating and total heat load must be considered for material selection and trajectory design. Mechanical constraints regarding flight acceleration loads must be reasonable for structural limits of the vehicle, on-board payloads, and supportive instrumentation. These factors enable determination of survivable AGA flight corridors for different planetary bodies based on input atmospheric entry conditions and desired outputs. To achieve larger turn angles, the path angle of the spacecraft must be steeper through the atmosphere, leading to significantly more heating and drag experienced by the vehicle.

For any AGA maneuver, a robust thermal protection system (TPS) and aeroshell will be required for the spacecraft to survive entry to the planetary atmosphere. If the

mission is implementing multiple AGA maneuvers and the aeroshell TPS has ablative properties, material will degrade from the aeroheating with each successive atmospheric maneuver. This ablation will alter the external geometry of the aeroshell, hence affecting aerodynamic properties of the vehicle, as the external geometry of the vehicle. To minimize the heating experienced during atmospheric flight, proper aero-thermodynamic design of the nose bluntness of the aeroshell is required. Understanding the aerothermal environment is crucial for TPS material selection and sizing to enable survivable AGA missions.

To maximize the effectiveness of an AGA maneuver, the drag losses during the atmosphere path must be minimized. Vehicle aerodynamics during hypersonic flight must provide a high lift-to-drag ratio (L/D), as this is critical to mission success [8]. Obtaining a high L/D for hypersonic flight is done by using a waverider shaped aeroshell to house the spacecraft payload [6]. Examples of three typical geometric waverider configurations are depicted in Fig. 1.2

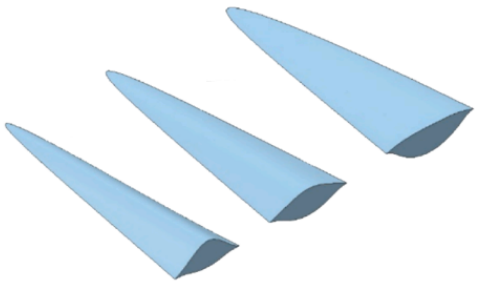

Figure 1.2: Typical geometric waverider configurations [10].

Hypersonic aerodynamics is critical for AGA maneuvers, as aerodynamic lifting forces are at play once the spacecraft encounters the atmosphere. The interplanetary vehicle is travelling at hypersonic velocities when it makes contact with the upper atmosphere, allowing for the modifications to the orbital trajectory [11]. An aero-gravity assisted flight uses the aerodynamic lifting forces of atmospheric gas molecules to redirect the velocity while minimizing energy losses. Waverider vehicle designs are ideal for the high L/D requirement for the trajectory maneuver, as energy losses due to atmospheric drag must be minimized while energy is gained through lift from grazing the outer layer gas molecules found in the atmosphere of the flyby planet. High L/D vehicles are able to fly an extended range in the atmosphere by pointing the lift vector downwards, enabling higher turn angles by altering the forces acting on the body to change the original orbit. An example AGA technology demonstration mission with an Earth departure and return found that for a flyby of both Venus and Mars, the maneuver required a maximum vehicle L/D of 3.015 [12].

1.4.2 Hypersonic Aero-thermodynamics

Hypersonic flow regimes are considered to begin at speeds of Mach 5. At hypersonic velocities, understanding topics of boundary layer characteristics, physical gas dynamics, and high temperature phenomena become critically important. For the application of vehicle design, the key hypersonic aero-thermodynamics disciplines include aerodynamic forces and surface interactions, convective and radiative aeroheating, as well as fluid dynamics topics like shock interactions, high temperature gas dynamics, flow separation and

reattachment [13]. Atmospheric effects at different altitudes as well as vehicle geometry and orientation also play crucial roles in understanding the hypersonic flight environment, influencing the design considerations for the spacecraft aeroshell.

As an aero-gravity assist trajectory maneuver brings the spacecraft inside the planet's atmosphere during a flyby, detailed understanding of the vehicles interactions from hypersonic atmospheric flight is critical to properly design an aeroshell that will survive. There are two types of atmospheric entry trajectories from space; ballistic and lifting, which control the design requirements of the flight vehicle. For AGA, a lifting entry trajectory is of consideration, as the primary force being generated is perpendicular to the flight path, acting to lift the vehicle body. Noted previously, a main design parameter for an AGA maneuver is the lift-to-drag ratio, which is the critical design variable for an atmospheric lifting entry. While drag is present throughout this entry maneuver due to gas molecules in the atmosphere, the resultant flight path can be continuously adjusted throughout the flyby to change both the vertical motion and flight direction. High L/D values will produce lower acceleration loads during atmospheric entry, but are subject to long duration atmospheric flight with continuous heating [14]. Peak temperatures experienced during a lifting entry are lower than a ballistic entry, but since the vehicle flies through the atmosphere for a longer duration, the total heat load absorbed may be higher. This has critical implications for TPS design, as management for the total heat load over the duration of the atmospheric flight of the vehicle is of utmost importance.

The high temperature gas in a hypersonic flow field strongly influences the forces acting on the surface of the vehicle (pressure and skin friction) and the energy flux (heat transfer) of the flight environment [15]. The energy flux from the hypersonic flow correlates directly to heat transfer rate and total heat load encountered by the vehicle. Aerodynamic forces and moments experienced by the vehicle during flight are resultant from the pressure and skin friction forces endured over the complete flight period.

The vehicle design requirements are dictated by the high temperature effects which dominate the hypersonic flight regime. Aeroheating comes from the kinetic energy of a high-speed, hypersonic flow field as it is dissipated by the influence of friction within the boundary layer. This extreme dissipation which occurs in a hypersonic boundary layer is what creates very high temperatures, as internal vibration energy is excited within the gas molecules causing dissociation and ionization within the gas. Upon atmospheric reentry at hypersonic speeds, the external geometry of the vehicle creates different heating effects based on its shape. For a sharp leading edge object like a cone or slender wedge, the shock is attached to the front point and diverges geometrically out according to the body's geometry. For this configuration, stagnation point heating is direct heating as no shock layer of gas can dissipate the energy present on the body undergoing hypersonic flight. In the case of vehicles, the forebody shape usually has a rounded blunt profile to create a bow shock in front of the body and a viscous shock layer between the shock and body [16]. Accurate prediction of environmental effects is critical to properly allocate design requirements for vehicles flying at hypersonic velocities [15]. The pressure distributions are critical for assessment of structural loads for the vehicle, while the peak heat rate and total heat load are mapped over the vehicle surface as part of the TPS design process.

For hypersonic flight vehicles, the bluntness of the windward facing edge significantly impacts heat rates on the vehicle and other shock wave behavior [17]. Vehicle geometry with sharp leading edges will experience extremely high temperature flow behavior. An example illustration of a waverider with blunted leading edges of $R_n = 10$ mm can be seen in Fig. 1.3

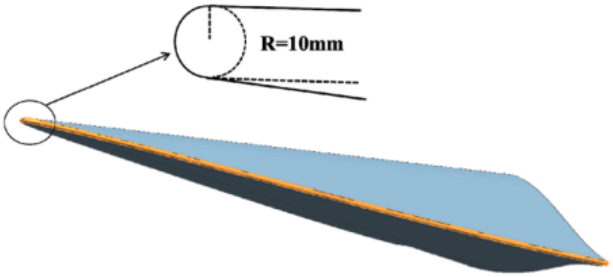

Figure 1.3: Blunted leading edge of waverider geometry [10].

The bow shock wave created in the nose region during hypersonic flight is normal or nearly normal to the vehicle, creating a gas temperature behind the shockwave that is quite high [17]. Blunt bodies generate stronger shock waves, leading to efficient energy dissipation at the cost of maneuverability and increased losses to drag [18] as the blunt nose moves the extremely hot shock layer further away from the body wall. The shock waves convert kinetic energy to the flow regime, resulting in heating of the gas, molecular dissociation, and ionization. Most of the energy is conducted into the vehicle wake and is propagated downstream of being transported to the surface of the vehicle [18]. For these reasons, blunt vehicle faces with low ballistic coefficients are optimal for heat reduction, as they create an increased distance between from shockwave detachment to the surface vehicle.

The aeroheating experienced in the hypersonic flight environment can be both convective and radiative. Convective aerodynamic heating comes from the heat transfer of the hot boundary layer to the cooler surface. Radiation heating occurs when the shock-layer temperature is high enough that the thermal radiation emitted by the gas itself begins influencing the aerothermal environment, with radiation being produced by excited atoms and molecules in the shock layer [18]. Radiation heat transfer begins to occur with high entry speeds over 7 km/s, as the energy is sufficient to dissociate and ionize gas to form a hot plasma in the shock layer region, radiating heat to the vehicle structure [16]. It is critical to understand the balance of convective and radiative heating, as thermal protection systems must be designed for the specific heat transfer mechanism. Heat transfer rate vs flight velocity for a vehicle at an altitude of 60 km and $R_n = 4.5m$ is shown in Fig. 1.4. As noted, the velocity threshold which radiative effects begin to noticeable contribute begins above 7 km/s, but this heat flux is not dominant until higher speeds. As velocities exceed 11 km/s, the fraction of heating due to radiation increases sharply. The air in front of the vehicle becomes ionized forming a plasma which emits intense energy to the vehicle, significantly increasing the fraction of heating from radiation. The equations which govern stagnation point heating on the waverider aeroshell are discussed in Chapter 4.

Variations in the composition and density of the planetary atmosphere at different altitudes play a significant role in determining the heat transfer to the vehicle. Peak hypersonic aerodynamic heating will always occur at altitudes where the flow behaves as a continuum, but the vehicle will first encounter rarefied flow due to the low molecular density in early atmosphere. The parameter that characterizes low density flows is the Knudsen number, which is the ratio of the mean free path of gas molecules to the characteristic length of the vehicle [19]. The Knudsen number relation is give below in equation

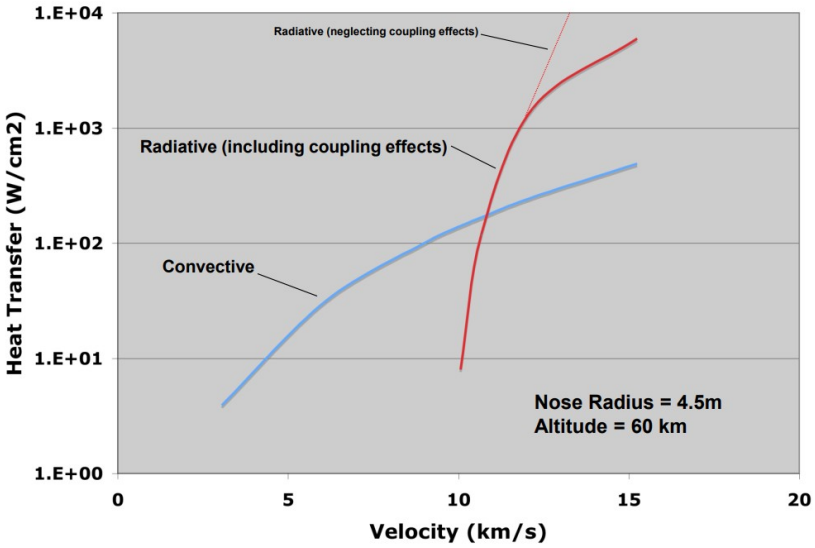

Figure 1.4: Comparison of radiative and convective stagnation-point heat transfer with flight velocity [18].

1.1.

$$K_n = \frac{\lambda}{L_{\text{char}}} \tag{1.1}$$

It is a critical criteria to examine in order to determine to what extent low density flow effects are important. At upper levels of the atmosphere, the density of air molecules is much lower, meaning that the mean free path (average distance between vehicle collision air molecules) is relatively large. Characteristic length is important to the Knudsen number, as it defines the physical scale of the aeroshell. Looking at an altitude of 342,000 ft, the mean free path (λ) is one foot compared to microscope value at sea level value of 2.9979×10^{-8}ft [17]. Above altitudes of 300,000 ft (92 km), the flow in the nose region of vehicles cannot be treated by the same assumptions given in a continuum flow, as they will break down due to free molecular flow (FMF) aerodynamics [17].

At high altitudes for vehicles with small nose or wing leading edge radii, these regions experience low density flow phenomena which alter heating behavior [19]. The specific value of the Knudsen number, K_n, governs the three flight regimes experienced- the FMF regime, the transition regime, and the continuum regime. This comparison of Knudsen number vs. altitude is depicted graphically in Fig. 1.5 and summarized in in Table 1.1. The flow is in the continuum regime when the Knudsen number is below 0.01. From 0.01 to about 1 the flow is considered in transition flow. Altitudes where a vehicle may experience transition flow is between 80 and 140 km. Free molecular flow occurs above a Knudsen number of 1. At altitudes above 130 km, the air molecules can be on the order of 100 meters apart.

A hypersonic vehicle undergoing AGA will first move into the rarefied flowfield where molecular impacts on the surface are begin to be important. Next, the vehicle encounters the transition regime which takes into account slip effects on the vehicle, before reaching the continuum regime of the atmosphere [17]. The continuum region is where Navier-Stokes equations hold, and once the transition regime is reached, slip effects must be included. As notated, affects of FMF begin around a value of $K_n = 1.0$.

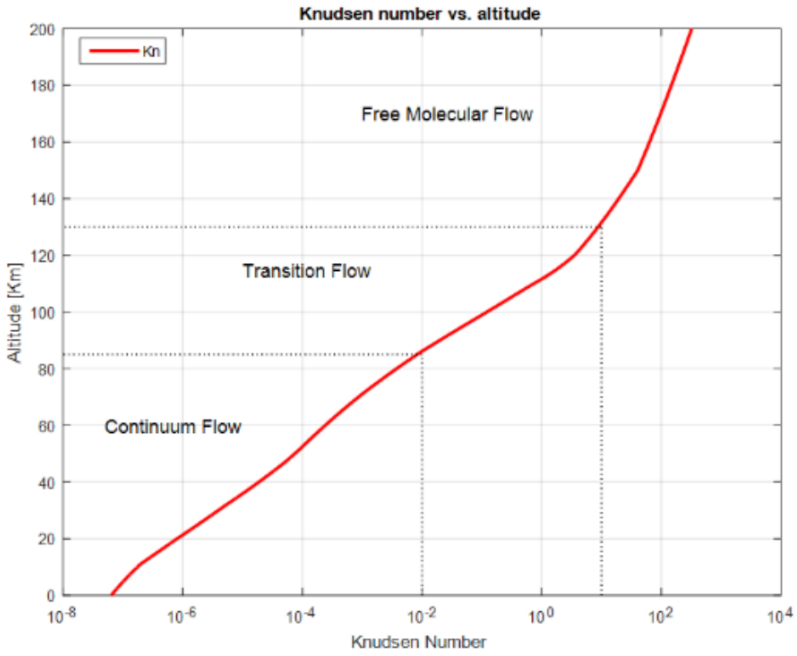

Figure 1.5: Knudsen number vs. altitude flow regime plot with characteristic length scale of 1 meter [20].

It is seen that for a very small K_n, a continuum flow exists, and for a large K_n FMF is experienced by the vehicle. Length is a governing factor in computing the Knudsen number, larger vehicles experience continuum flow to higher altitudes than small vehicles. For high altitude hypersonic flight, proper treatment of leading-edge flow by low density methods is important to consider during analysis [17]. Knudsen number correlations to the three flow regimes can in Table 1.1.

Table 1.1: Flow regimes based on Knudsen number.

Flow regime	**Knudsen number (K_n)**
Continuum	$K_n < 0.2$
Transition	$0.03 < K_n < 1.0$
Free molecular	$K_n \geq 1.0$

1.4.3 Waverider Design Considerations

As the AGA trajectory and hypersonic aero-thermodynamic environment have been discussed in detail, inspiration for the selected geometric design of the waverider aeroshell is explored in this section. For hypersonic vehicles, high lift to drag ratio is a key design objective to enable larger down and cross range capabilities. An efficient waverider design with high L/D is difficult to achieve for hypersonic flight conditions as severe wave drag and friction drag will exist. As Mach number increases for supersonic and hypersonic regimes, the waverider L/D reaches a limit that restricts improvement this aerodynamic performance [10]. A successful AGA maneuver is dependent on whether the aeroshell configuration will supply the required lift with a small corresponding drag value. If drag is prohibitively high, energy losses will negate the advantages of the AGA maneuver [11], thus L/D is critical to maximize.

The waverider is defined by a supersonic or hypersonic vehicle that has a shock wave attached along its leading edge. The name comes from the fact that the vehicle is riding atop of the shockwave, leading to a higher L/D when compared to generic hypersonic vehicle configurations [21]. Original waverider configurations are generated with a sharp leading edge that supports the shock wave while minimizing drag. Yet for practicality purposes with hypersonic flight, the leading edge must blunted for heating, manufacturing, and handling [10].

The aero-assisted and modified hyperbolic trajectories can be represented with equations that are functions of L/D, the importance of a high lift-to-drag ratio is clear. Maximum angular deflection of the trajectory and the exit velocity at the end of transit through an atmosphere is directly proportional to L/D, as it was observed that increasing L/D ratio served to decrease the velocity decrement during the atmospheric transit of the vehicle [21]. Waveriders tend to have large wetted surface areas, so trade offs between wave drag and friction must be accounted for in the L/D optimization process. Significant viscous drag can result from the large surface area, and low volumetric efficiencies can present challenges for packaging and payload integration [22]. A waverider shape derived for shock attachment, high volume, and a maximum L/D can be seen in Fig. 1.6

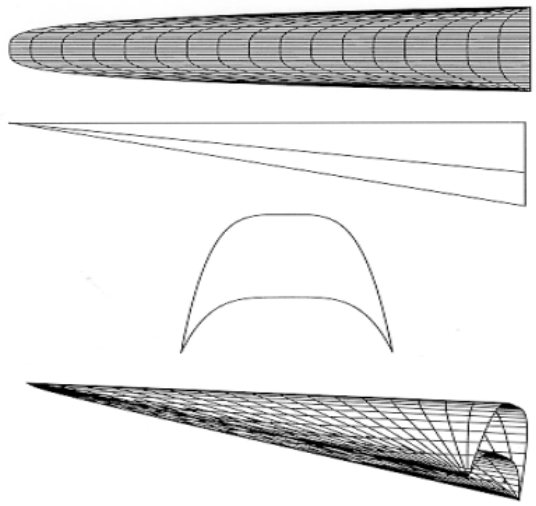

Figure 1.6: Waverider shape derivation [22].

For hypersonic flight, sharp leading edges offer advantages in aerodynamic performance as they induce minimum drag and offer higher crossrange during reentry. However, a major drawback is they are subject to severe aero-thermodynamic loads [23]. Increasing the leading edge bluntness of the waverider showed significant aerodynamic performance degradation in the L/D of the aeroshell, but reduces the convecting heating rate in the high-speed environment [4]. Aerodynamic performance and aero-heating characteristics are highly sensitive to the bluntness of the leading edge [24], thus trade-offs from the bluntness effects must evaluated. Blunting leading edges of the waverider will decrease lift and increase drag, which reduce L/D [10], but are critical for waverider leading edges as it must be able to survive the hypersonic environment present during the AGA maneuver.

Common design inspiration for waveriders comes from using known flowfields to construct vehicle surfaces with predefined aerodynamic properties. In this sense, the

waverider is a simple solution to the general, highly-nonlinear problem of hypersonic aerodynamics [25]. The design procedure for a waverider capable of a wide speed range includes three main parts: designing and solving the basic flow field, tracing a group of streamlines in the basic flow field, and lofting all the streamlines to generate the upper surface and compression stream surface [26]. Completing all three steps in this waverider design procedure is outside the scope of this conceptual report, but NASA's Configuration Based Aerodynamics (CBAERO) software [27] is used to generate the flow field and tracing streamlines over the body of the waverider. CBAERO enables accurate aerodynamic performance predictions and makes estimates on the thermal environment experienced by the aeroshell.

In essence, waveriders must be supersonic shapes designed for bow shockwave attachment to the leading edge of the body. A best practice is designing waveriders directly or inversely from the flowfield conditions they will experience during flight. This provides a common methodology for waverider generation; starting with a known flow associated with a chosen shape in a supersonic or hypersonic free stream conditions [22]. With this framework, simple shapes are a good starting point for generating the external geometry of a waverider.

Two shapes that are commonly used initially for the waverider design are wedges and cones. A simple wedge geometry allows for ease of calculation for the flows shockwave, while providing high lift upon the body. Conically derived waveriders have been used extensively as they tend to have higher volumetric efficiency than the wedge-derived forms, yet still lead to relatively simple analytical solutions [22].

In the early 2000's, NASA Ames Research Center (NASA-ARC) had an ongoing research program for the development of Ultra High Temperature Ceramics (UHTC) for next generation reusable launch vehicles. It was believed that the UTHC's might enable design of vehicle leading edges with temperature above Advanced Carbon-Carbon, opening up possibilities of hypersonic vehicle design with sharp leading edges to increase aerodynamic performance [28].

NASA-ARC proposed a flight test for demonstrating the feasibility of a sharp leading edge hypersonic reentry vehicle. The major goal of the demonstration mission was to test and advance technology readiness levels (TRL) of the UHTC heat shield which might enable design of non-ablative sharp leading edges for hypersonic vehicles. The geometry of this technology demonstrator, known as the Slender Hypervelocity aero-thermodynamic Research Probe - Lifting Entry 1 (SHARP-L1), was selected to be a hybrid cone-wedge based on the trade-offs between hypersonic aerodynamic performance (L/D) and volumetric efficiency (cost) [29]. The proposed SHARP-L1 vehicle geometry is displayed in Fig. 1.7

The SHARP-L1 is not a waverider by definition, as this cone-wedge hybrid geometry was proposed for a NASA TPS demonstration. The external geometry was chosen for the vehicle, as it was designed for high lift in atmospheric reentry [22]. The trade-off analysis implemented for the geometry selection was known as the Hankey optimization. This optimization showed that increasing hypersonic L/D decreased the volumetric efficiency for an optimal wingless geometry design [29]. The Hankey optimization which balances these two performance parameters be seen below in Fig. 1.8.

While the SHARP-L1 technology demonstrator was not funded for actual test flights, additional research was performed on the proposed baseline configuration to determine its flight performance. The SHARP-L1 lifting entry configuration was designed with a 1 mm radius leading edge and followed low earth orbit (LEO) re-entry trajectory

Figure 1.7: Proposed SHARP-L1 geometry with hybrid cone-wedge geometry [30].

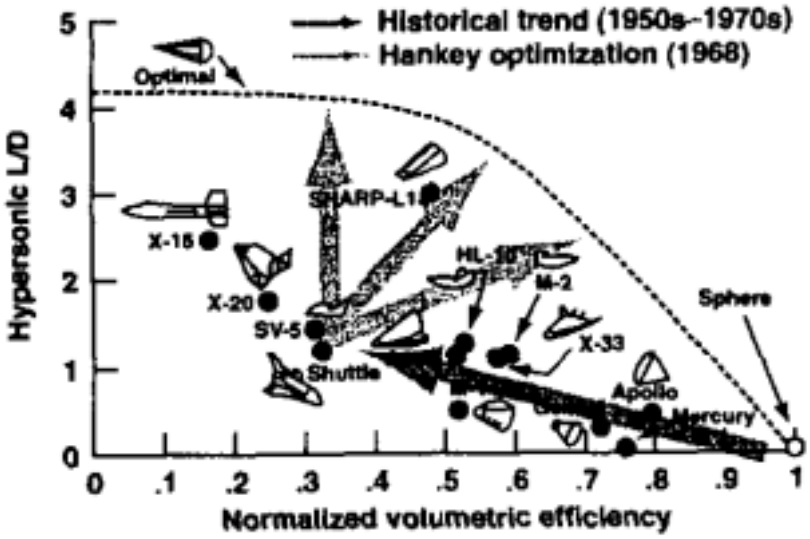

Figure 1.8: Hankey optimization comparison of hypersonic aerodynamic performance versus volumetric efficiency [29]

conditions similar to the Space Shuttle for computational studies [30]. In Starkey's analysis, pressure contours were generated from specified atmospheric flight conditions with CFD over a structured mesh grid topology of the vehicle, and suggestions were made for geometric improvements based on the results.

Major findings in this analysis were that overheating would occur along the sides of the vehicle for a portion of the re-entry trajectory, leading to unacceptable heating rates for non-ablative TPS. As the angle of attack increases for the vehicle, the pressure and temperature gradients on the lower surface of the vehicle increased compared to the upper surface due to flow spillage. Additionally, severity of leading edge shockwave/boundary layer interaction increased as angle of attack changed from zero to twenty degrees [30].

The solution to this unacceptable heating predicament may be one of the LEO re-entry trajectory conditions used in the feasibility study. This led to the investigation of

the performance of additional geometric design configurations as possible solutions to the heating problem [30]. These trajectory conditions are starkly different from those experienced during AGA, but this analysis provides critical insight for geometry optimization of the aero-thermodynamic conditions experienced by a high L/D hypersonic vehicle.

The major design parameters for this technology demonstrator is coupling high performance aerodynamic properties while maintaining useful volumetric efficiency for the aeroshell; exploration of waverider configurations for the vehicle geometry is a logical next step [30]. The waverider vehicles depend on a sharp leading edge for the shock attachment, so such a vehicle could still serve as a demonstrator to increase the TRL of UHTC thermal protection systems. Simple concave and convex waverider models were generated for comparison by Starkey [30], having the same volume, length, and width to the baseline SHARP-L1 vehicle. Little difference was found between concave and convex waverider, showing that vastly different configurations can have similar aerodynamics. The waveriders had increased L/D values when compared to the SHARP-L1, as well as reduced heating rates associated with the pressure leakage [30].

For the design of an aeroshell supporting AGA trajectory maneuvers, high performance hypersonic aerodynamics are a key requirement to maximize transit time reduction and limit required launch energy. Volumetric efficiency considerations are vital to support meaningful payload integration for such missions. Configuration variants of the SHARP-L1 geometry is used as a starting point for this conceptual aero-thermodynamic feasibility study.

1.4.4 Thermal Protection Systems

Thermal protection systems are critical for surviving atmospheric reentry, as hypersonic flow regimes will induce intense heating to the body of the vehicle. The kinetic energy of the vehicle dissipates into thermal energy as the vehicle enters the atmosphere, but only a small fraction of the thermal energy is transferred to the entry system [18]. While the thermal transfer fraction is dependant on vehicle size, shape, velocity and the aerodynamic regime, only 1% to 5% of the total thermal energy is transferred near peak heating [18]. For example, the temperature in the nose region of the Apollo reentry capsule heated the gas to approximately 11,000 K travelling at Mach 36 [17]. If all of the thermal energy were to be transferred from the gas to the reentry body, then it would likely vaporize or have severe damage [18]. To counter the intense thermal flux and heat accumulation on the aeroshell in the reentry environment, special materials and structural design techniques are utilized for the TPS.

Aerothermal modeling must be coupled to TPS design, as the TPS must allow the vehicle to survive the predicted environment. One critical design factor is the instantaneous heat flux at a specific point on the vehicle, known as the heat rate. The other factor is the heat load, which is the integration of the heating rate over the time of the trajectory [18]. The heat flux, along with pressure and shear stress, is used to select TPS material while heat load determines the thickness [18].

The three main types of TPS in consideration for a waverider aeroshell are passive, active, and ablative. The mission scenario and atmospheric flight path will drive the final material selection and sizing for the vehicle. NASA's Planetary Mission Entry Vehicles Quick Reference Guide contains high-level mission characteristics of past entry systems [31], providing critical data on reentry trajectory, geometry, aerothermal, TPS, and recovery systems as a benchmark for the design of entry vehicles for Earth and

Mars. While current research is ongoing and geared towards improvements to other novel thermal protection concepts like flexible or magnetic TPS, they are not discussed in this report.

Passive thermal protection systems are reusable, reliant upon reradiation to reject heat and low thermal conductivity to limit thermal penetration [18]. Coatings are an example which can be used to increase emissivity of the material or reduce catalycity of the surrounding high temperature gas molecules. The Space Shuttle TPS had seven main layers, with layers of tiles and materials to provide thermal insulation for up to 100 missions [32]. Active thermal protection systems are also reusable, with plumbing systems or active transpiration for heat rejection. However, active thermal systems are quite complex and are not often considered due to low technology readiness levels [18]. Ablative thermal protection systems are non-reusable, as they slowly burn off and use convection to keep the spacecraft within a safe temperature [32].

Due to the properties of hypersonic flow during reentry, ablative heat shields are an efficient option for thermal shielding [32]. A graph with a comparison of reusable and ablative TPS is seen in Fig. 1.9. This graphic displays the velocity of the reentry body versus atmospheric environmental conditions experienced during the mission which is critical to inform TPS selection for the vehicle.

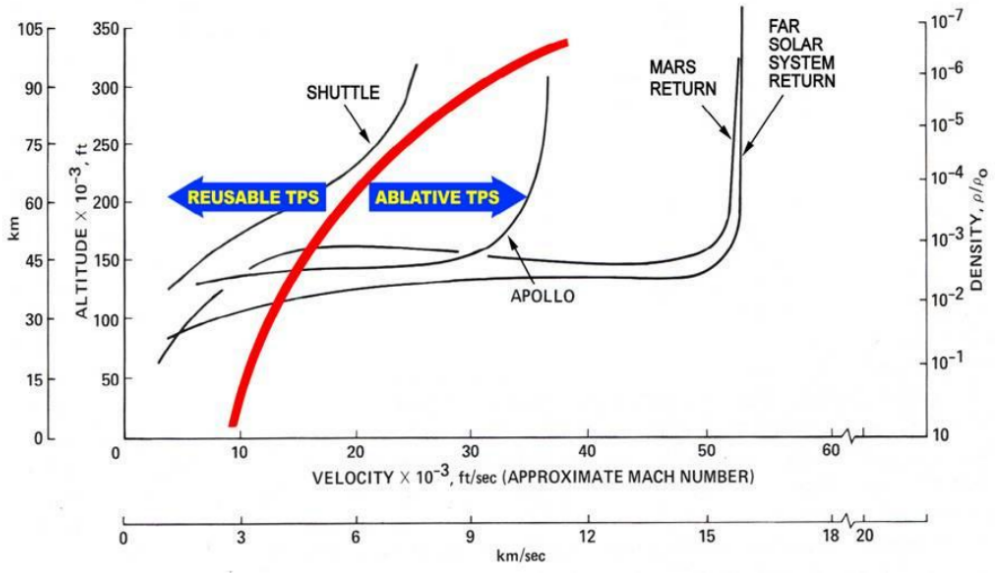

Figure 1.9: Comparison graph of velocity versus altitude and density for TPS selection [18].

Ablation is the process of absorbing energy by removal of surface material by melting, vaporization, sublimation, or chemical reaction [18]. An ablative heat shield will cover the external walls of the vehicle, having varying thickness depending on the predicted thermal environment. The ablative TPS layer will vaporize off the body to protect the vehicle, corroding away as it soaks up large amounts of thermal energy. The process of convection occurs because of the corroding layer, known as a pyrolysizing layer, is made of reinforced composites impregnated with organic resins [32]. As the composite skin pyrolysizes, it produces a residue layer called char, which forms to create a second level of heat protection [32]. A diagram of the ablation process can be seen in Fig. 1.10.

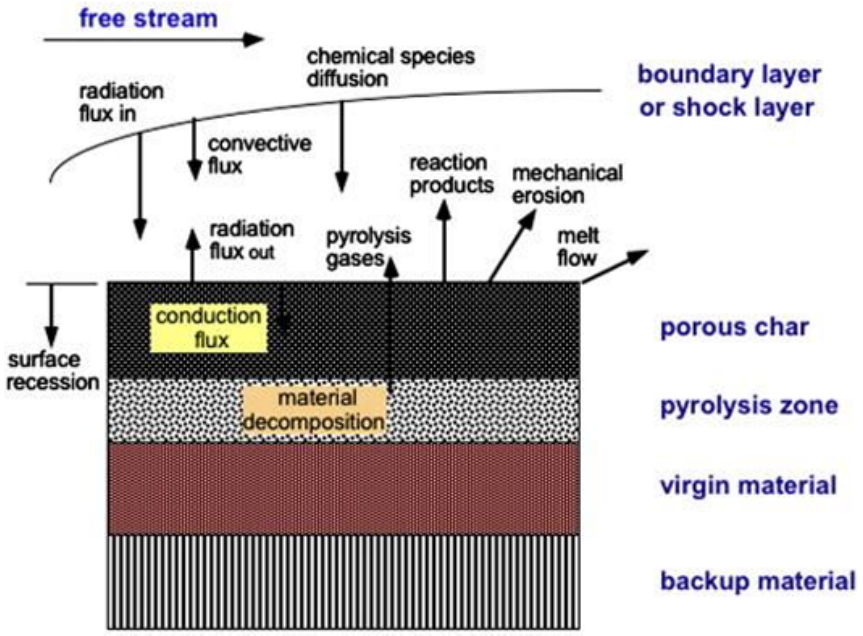

Figure 1.10: Diagram of the ablation process [32].

Ablative TPS options can be common solutions for severe aero-thermodynamic loads in hypersonic flow environments, but this thermal protection option will degrade aerodynamic properties of the vehicle which are crucial to maintain to perform useful AGA trajectory maneuvers. Non-ablative TPS is best for integration with the aeroshell as degradation of the external geometry will reduce aerodynamic performance, limiting the effectiveness of the AGA maneuver. Finding a balance between limiting aerodynamic drag experienced on the aeroshell while keeping the thermal environment at a survivable level for the TPS is critical for effective implementation of aero-gravity assist trajectory maneuvers.

1.5 Methodology

The scope of work for this project entailed creation of CAD models for the four waverider configurations with variable nose bluntness. Each model is parametric to enable rapid variation of the bluntness of the waverider aeroshell for both the rectangular and elliptical nose cases. Then, flight trajectory conditions are analyzed with CBAERO software to replicate flight conditions of a AGA trajectory maneuver. This reference trajectory assumes a constant L/D ratio of 1.5 and finds a transit time reduction of 7 years, reducing a 19 year trip to Haumea to 12 years [3] as seen in Fig. 1.11. This was found using the Mission Analysis Environment (MAnE) to model interplanetary trajectories. This project only considers the Earth AGA portion of the mission to Haumea.

To get the Solidworks CAD model compatible for analysis with CBAERO, the model must be saved as a .step file and loaded into Gmsh [33] to generate a surface mesh over the outer mold line (OML) of the waverider aeroshell. The mesh is saved as a .bdf file format from Gmsh so it is compatible to be read by CBAERO software. The simulation on the meshed geometry is then set up and run inside the CBAERO solver in the Linux environment. Post processing and plotting of the data produced in CBAERO

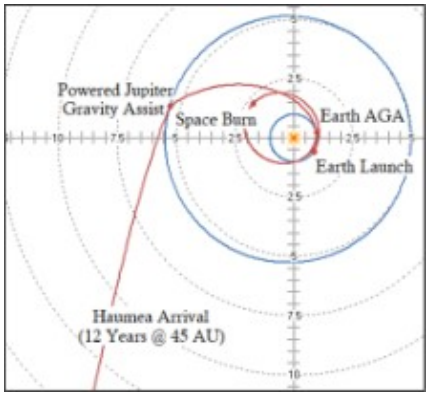

Figure 1.11: MAnE AGA flight trajectory for 7 year transit reduction to Haumea [3]

is completed with Python.

CBAERO is used to determine the aerodynamic coefficients of the waverider and to make estimates on the thermal environment experienced by the waverider aeroshell. This software is a conceptual level software utilized for preliminary analysis as it produces an un-anchored aero database based off solving ordinary differential equations on streamlines over the panels found on the imported surface mesh of aeroshell. For truly accurate thermal models, this data it must be anchored to high fidelity models to verify the weighting of the thermal heating on the vehicle OML [34].

Computational Fluid Dynamics (CFD) is a crucial tool which can anchor the aerodynamic coefficients, acting to validate and verify the thermodynamic behavior of the aeroshell during the trajectory maneuver. CFD provides closely accurate results for aerothermal behavior in the continuum flow regime, but the problem gets compounded with low density high mach flows. For a high fidelity heating model of an AGA trajectory maneuver, the solver must include a Direct Simulation Monte Carlo (DSMC) code like DAC [35] to make correct assumptions for rarefied and transitional flow regimes when the Kundsen number falls below $K_n = 0.003$ during high altitude flight.

To generate a high fidelity aerothermal database for the waverider configurations across the entire AGA trajectory, more powerful softwares including DLPR [36], NEQAIR [37], TRAJ [38], and DAC would be required to accurately model present atmospheric conditions and close the loop on the complete engineering design for an AGA mission. As access to such solvers is restricted without government contract work, high fidelity simulations to anchor conceptual results found in CBAERO will not be able to be produced for the scope of this project. The conceptual aerothermal performance results of the waverider configurations of interest will be discussed and plotted graphically.

A discussion on the variation between performance of different waveriders and resulting feasibility implications of the different aeroshell configurations for AGA will conclude this report. This allows for recommendations to be made on what geometric waverider configurations perform best for Earth AGA mission scenarios, laying groundwork for high fidelity models to anchor the produced data. Continued work would enable ground rules to be placed upon fast transit missions and map different planetary flight corridors beneficial for AGA maneuvers.

Chapter 2:

Hypersonic Waverider Design

The focus of this chapter is upon modeling the geometric design configurations of waverider aeroshell models for analysis with CBAERO. The CAD design workflow is first explained in detail for the for the rectangular nose baseline aeroshell configurations. The geometric parameterizations in the design process and other waverider configuration models are be discussed. CAD models of the four waverider aeroshells can be seen below, with design metrics and methodology of each specific aeroshell discussed in depth.

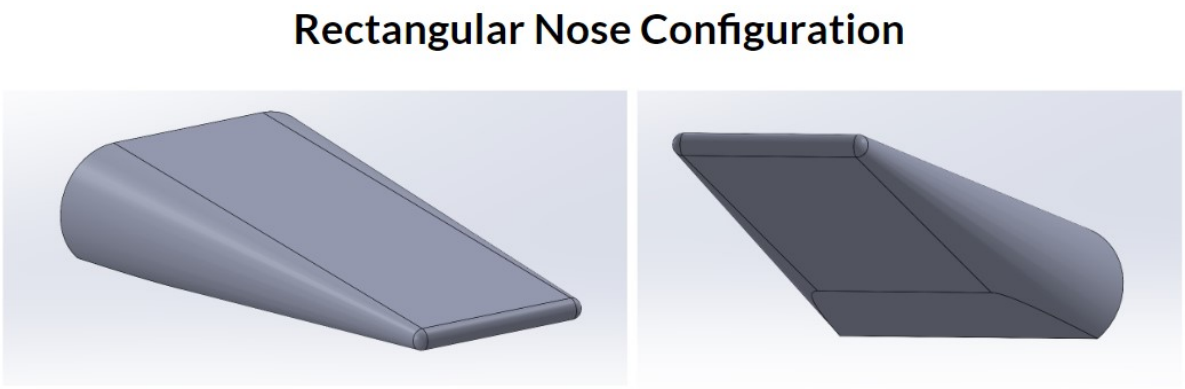

Figure 2.1: Rectangular nose waverider configuration with $R_n = 0.1$m

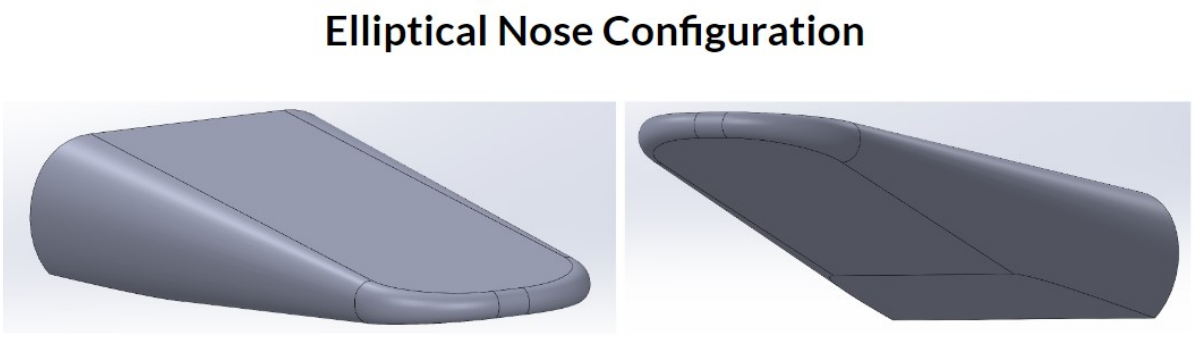

Figure 2.2: Elliptical nose waverider configuration with $R_n = 0.1$m

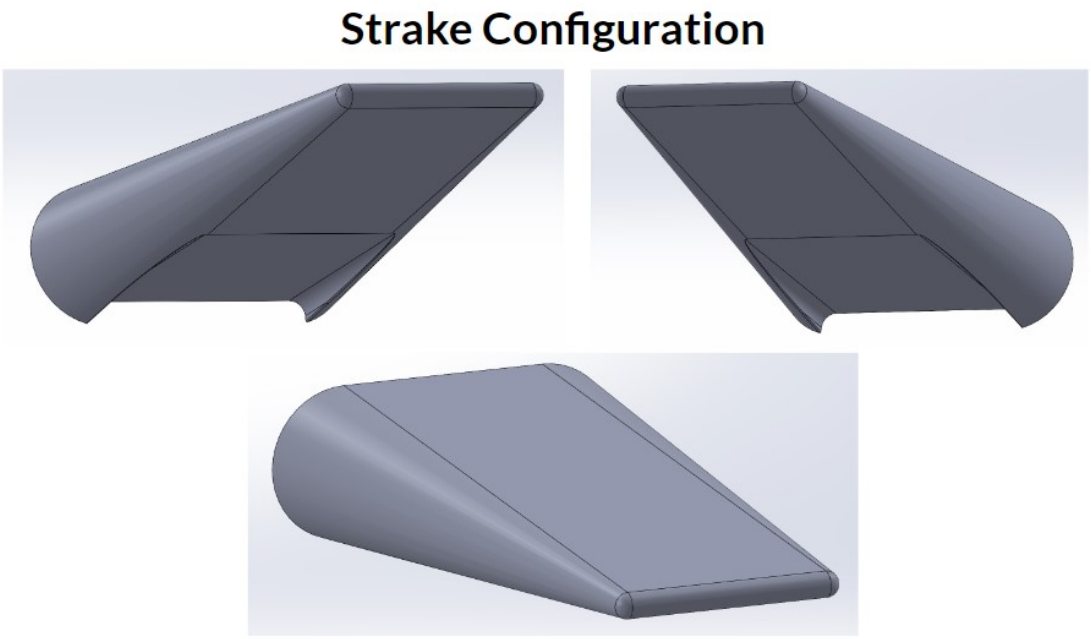

Figure 2.3: Rectangular nose waverider strake configuration with $R_n = 0.1$m

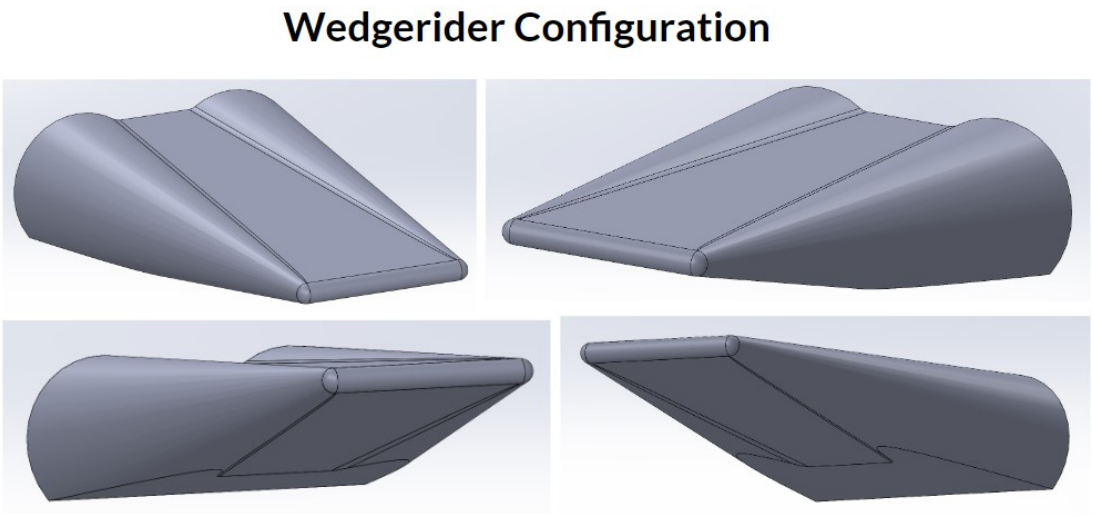

Figure 2.4: Wedgerider configuration with $R_n = 0.1$m

2.1 Waverider Design Point of Departure

The geometric model of the SHARP-L1 vehicle was first created in the SolidWorks CAD environment. This aeroshell geometry was based initially off an existing .igs files provided by Analytical Mechanics Associates, Inc. from prior analysis work on the SHARP-L1 model. The files were used previously by NASA-ARC in the early 2000's for aerodynamic performance analysis on the SHARP-L1, so the footprint of this geometry was the initial point of departure for this project.

The vehicle sizing for the SHARP-L1 is fairly small as it's purpose was to serve as a TPS research probe, so it could not house a useful scientific payload, so it was scaled to have a main chord length of 4.8 m and a main span of 1.6 m. The dimensions of the .igs file provided a baseline for understanding the vehicle aspect ratio and wedge angle along the chord to create a watertight geometry for mesh generation. This geometry was then parameterized to rapidly drive a variety of geometric waverider configurations for aero-thermodynamic simulation analysis.

2.2 Aeroshell Configuration and Modifications

The SHARP-L1 vehicle, depicted in Fig. 1.7, has a rectangular nose with a sharp 1 mm leading edge. As this vehicle was designed for UHTC TPS TRL improvements and testing, the extremely sharp leading edge will create high, concentrated heat flux during hypersonic flight. As the radius of curvature on the nose of the vehicle increases, the convective heat flux experienced by the vehicle will be reduced by the square root of $1/R_n$. This relationship and relevant equations for aerodynamic heating during hypersonic flight will be discussed in detail Chapter 4.

For the scope of this analysis, the blunt nose radius on the front of the SHARP-L1 vehicle is varied in 50 mm increments from 100 mm up to 250 mm, as findings in Starkey's analysis found unacceptably high heating rates for the SHARP-L1 undergoing a LEO Space Shuttle return trajectory [30].

A 1 mm edge will lead to extreme heating on the waverider which is the reason for larger blunt radius values consideration. In addition to the bluntness variation on the rectangular nosed SHARP-L1 model, three other waverider aeroshell designs are analyzed in this report. All aeroshell designs share similar constants, building from the rectangular nose SHARP-L1 baseline with different external mold lines. This variation of the baseline geometry will affect the aerodynamic performance and heating on the different aeroshell bodies, and the most optimal design for AGA will be highlighted in the discussion section of the project. The aeroshell modifications from the SHARP-L1 baseline include a vehicle model with strakes added along the flap, an elliptical nose model, and the final model dubbed the "wedgerider". This configuration replicates the optimal contracting wedge geometry from Kolodziej's work, with the addition of rounded side profiles intended to create a central high lift surface along the body. The wedge geometry, front wedge angle of the vehicle, chord length, span width, and flap position were held constant among all waverider configurations.

2.2.1 Rectangular Waverider Design Parameterization

The Cartesian coordinate basis for the aeroshell geometric configurations can be seen in Fig. 2.5, and are meant to align with the basis needed for CBAERO simulations. Descriptions of the x, y, and z axis are itemized below:

- The x-axis aligns with vehicle chord, with the positive direction being in the windward direction facing in front of the vehicle.
- The y-axis aligns with vehicle height, with the positive direction being upward and opposite the flap.
- The z-axis aligns with vehicle span, with the positive direction being to the right of the aft section of the aeroshell and into the page of the schematic seen in Fig 2.5.

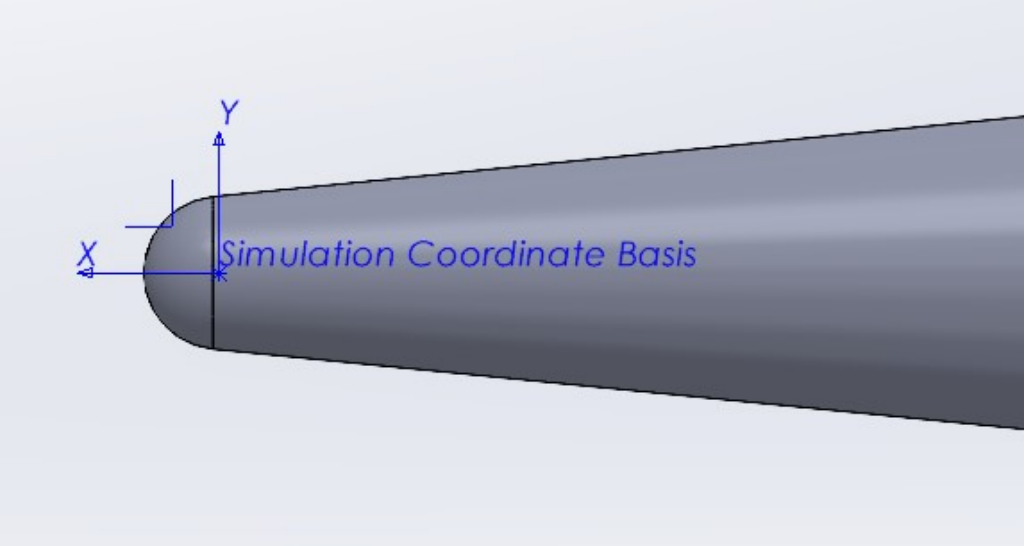

Figure 2.5: Simulation coordinate basis on nose of waverider

Once the coordinate basis is aligned in the correct direction in SolidWorks, a first sketch is created on the x-y axis to first draw the wedge profile of the waverider. A point is placed at the origin of the model, and a horizontal construction line is dimensioned to match the length of the main chord as it extends back from the location of the origin. The upper and lower wedge lines are drawn at a vertical distance from the origin which matches the nose bluntness radius of the given waverider model. The nose radius dimension is parameterized to enable rapid changes for different waverider nose bluntness. The top and bottom wedge lines are set at an angle of 5.63 degrees to match the total wedge width of 11.26 degrees of the SHARP-L1 .igs file. The vehicle nose is then drawn as a semi-circle to match the parameterized blunt nose. A tangency condition is enforced between the wedge lines and blunt nose semi-circle to ensure smooth transition along the nose of the waverider. This sketch can be seen in Fig. 2.6 is then extruded along the mid-plane of the z-axis to match the length of the main span of the waverider. The extruded wedge profile is displayed in Fig. 2.7

The next sketch is used to create the conical sides of the vehicle. A reference plane is first created on the side of the extruded wedge, which becomes the reference plane for this sketch. The convert entities feature is used to redraw the centerline and top

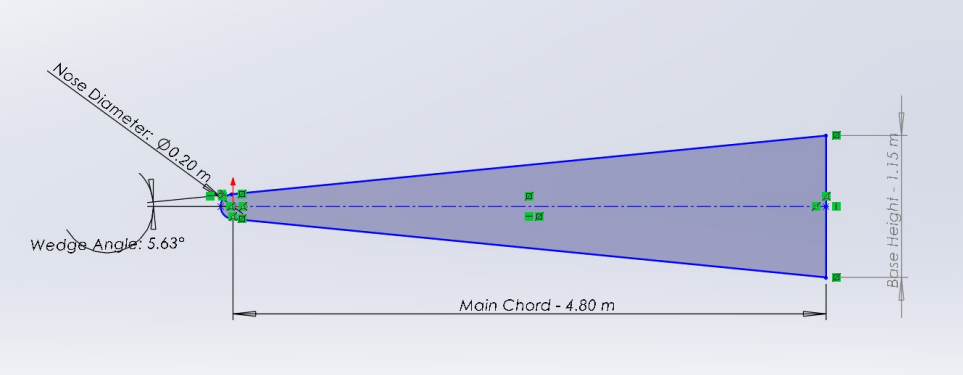

Figure 2.6: Initial wedge profile sketch

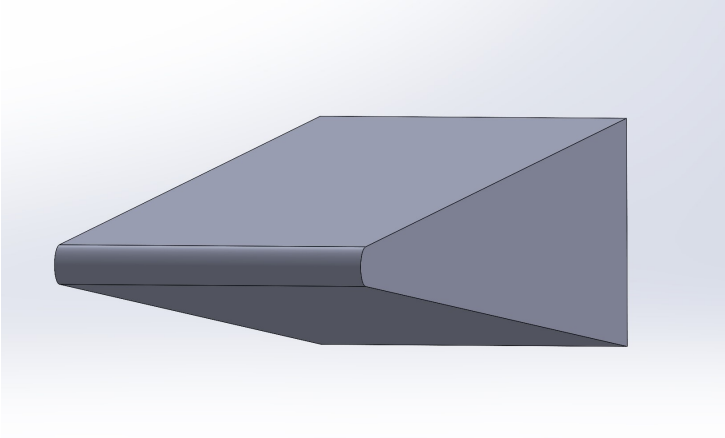

Figure 2.7: Extruded wedge profile

outline of the vehicle, as shown in Fig. 2.8. A 360 degree revolve feature is used with the centerline acting as the axis of revolution to create one conical side of the vehicle. This feature is then mirrored across the central axis, creating the baseline wedge-cone geometry as depicted in Fig. 2.9.

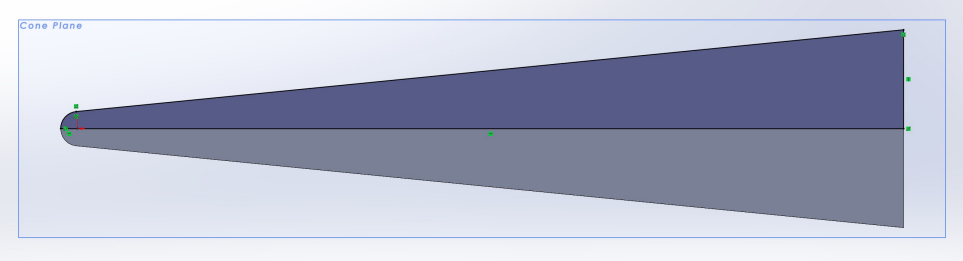

Figure 2.8: Conical side profile sketch

Next, a sketch is made on the back face of the vehicle to denote the location to place the flap. A straight line for construction is ran from the center of the vehicle to the bottom of the wedge. From the construction line endpoint on the bottom of the wedge, a point is placed at a distance of 150 mm up from the bottom edge of the vehicle seen in Fig. 2.10. This point and the central construction line will be used to define a reference plane on the y-z axis for the flap to be sketched upon.

Once the flap plane is created, a square box is sketched covering the back half of

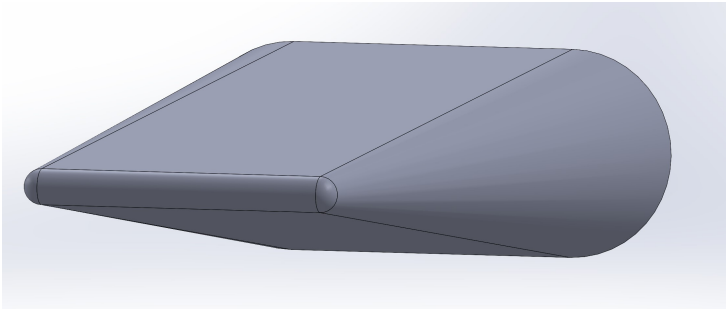

Figure 2.9: Wedge-cone waverider profile

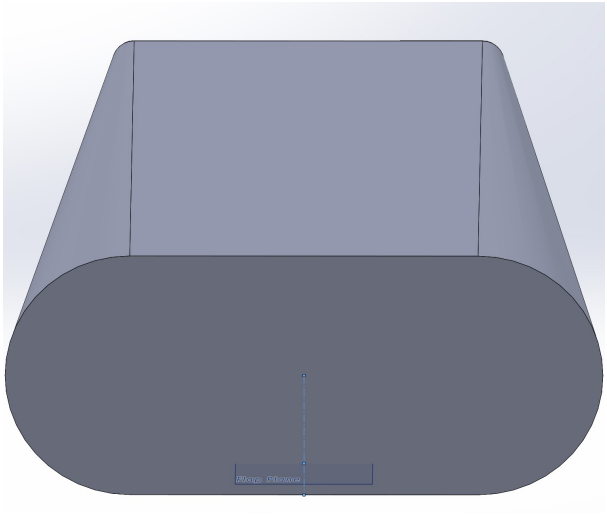

Figure 2.10: Flap plane location

the vehicle. The box can extend beyond the tail of the vehicle and will create a flat cut from the location of flap plane down along the aft of the vehicle. A cut extrude is used to create the flap depicted in Fig. 2.11, and due to the wedge angle of the vehicle, it will have a constant length for rectangular and elliptical waverider variants. This project does not consider controllability or stability of the waverider vehicles, but this flat region along the base of the vehicle is where control surfaces and various flaps could be integrated to the waverider.

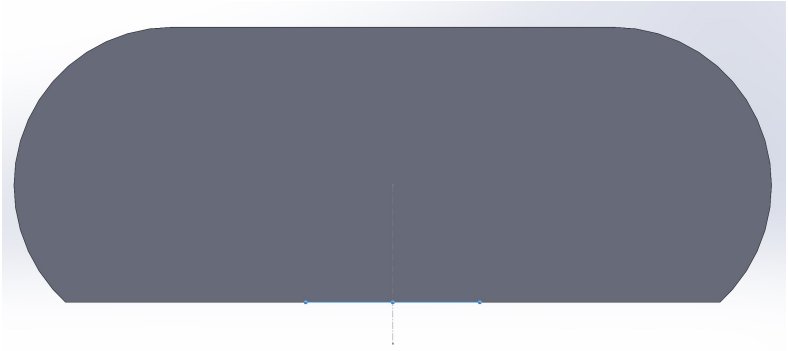

Figure 2.11: Aft view of waverider with flap cut

This SolidWorks workflow is used for the basic geometric design of all wedge-cone waverider models used for analysis in this project. As CBAERO requires a reference

area of the vehicle, another plane was created at a distance of 1.5 m from the x-z top plane. Again, the convert entities feature was used and a trace was made of the entire top profile of the vehicle. This sketch was then extruded to have a small thickness to create a 3D feature for the projected area of the waverider depicted in Fig. 2.12. The measure feature was then utilized to evaluate the area of this projected area, which was input to the CBAERO simulation.

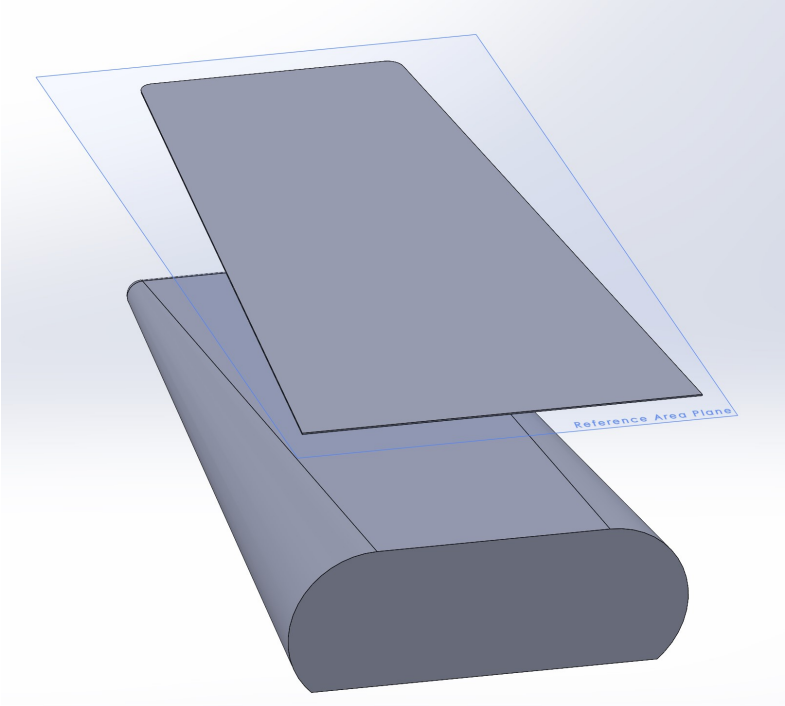

Figure 2.12: Reference area extrusion of waverider

2.2.2 Elliptical Design Model

The elliptical waverider has the most geometric variance from the baseline design workflow. After extruding the main wedge geometry of the waverider, a sketch is made on the X-Z plane to create the elliptical nose profile. The central region of the elliptical nose is set to a constant of 0.25m, and a constant curved spline curvature is used to create the shoulders at a distance of 0.6m from the tip of the nose along the chord of the vehicle, as seen by the blue tracing in Fig. 2.13. This feature is cut from the extruded wedge to form the elliptical nose feature on the wedge depicted in Fig. 2.14.

Figure 2.13: Top view of sketch to cut elliptical nose

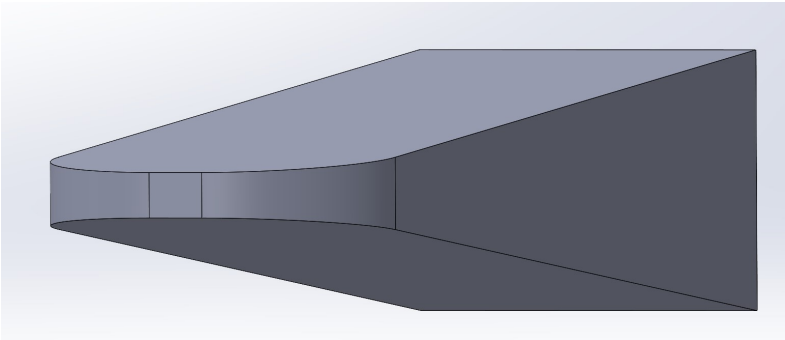

Figure 2.14: Elliptical waverider wedge profile

The conical sides of the elliptical waverider were then created around the edge of the extruded wedge using the boundary surface feature with a tangent to face condition at a distance of 3 inches, seen in Fig. 2.15. This boundary surface was applied to the other side, the front shoulder regions, and the constant front nose profile section of the geometry depicted in Fig. 2.16 for close replication to the span of the rectangular waverider models. A surface plane surface feature is then applied to the aft of the vehicle so that all surface features can be stitched together and made to be a solid, watertight geometry for meshing.

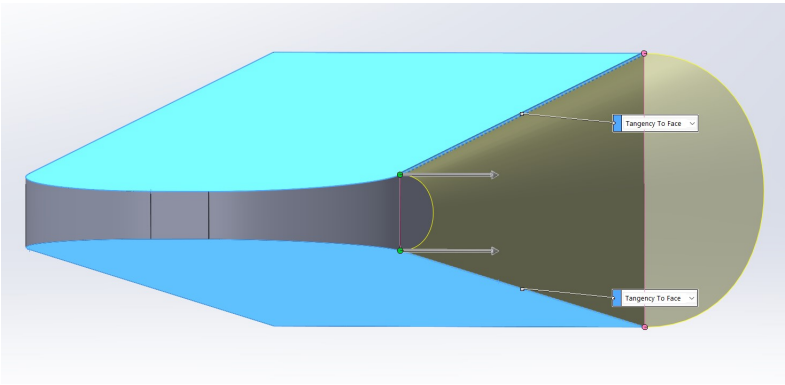

Figure 2.15: Boundary surface feature to create conical sides of elliptical waverider

The flap of the elliptical vehicle is then extruded on the flap plane of the waverider, which is placed at the same position on the aft of the vehicle as the rectangular nose model. Similarly, a sketch is made above the elliptical vehicle profile to find the projected reference area value needed for all CBAERO simulations.

2.2.3 Strake Design Model

In Starkey's analysis on the SHARP-L1, he proposed a vehicle configuration that added simple bolt-on, shock attachment strakes. The strakes would act to isolate the lower surface flowfield from the upper surface of the flowfield during high AoA maneuvers, adding a waverider-esque quality to the aeroshell without completely changing the rectangular nose configuration [30].

The proposed geometry with the strake modification can be seen in 2.17. While preliminary results found viscous wave drag would increase as a result to the addition of strakes, this geometry modification provided improved vehicle lift and was found to be

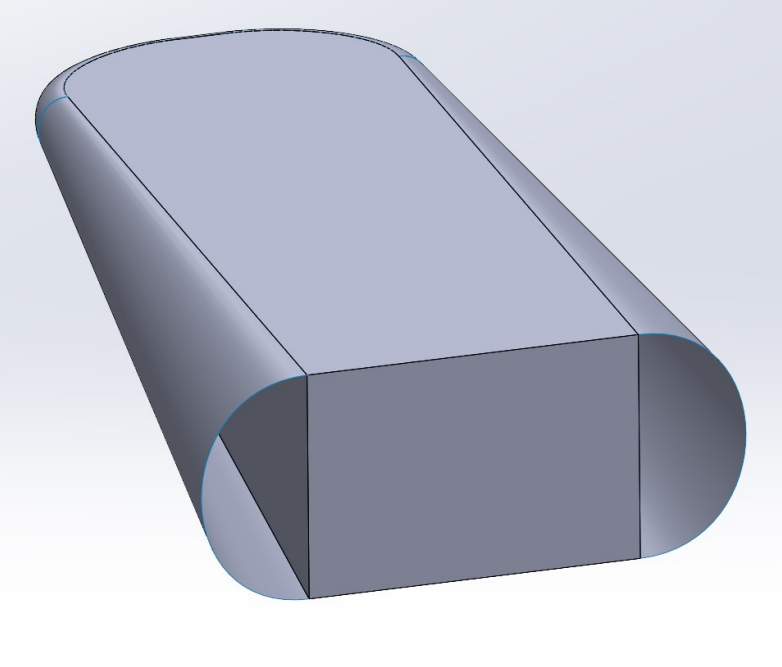

Figure 2.16: Elliptical waverider profile with surface features

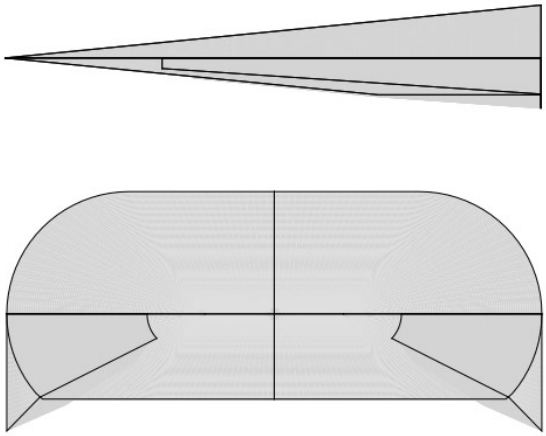

Figure 2.17: Strake modifications to SHARP-L1 vehicle configuration [30]

a good solution over most AoA [30]. These results inspired a rectangular nosed strake variant to be designed in SolidWorks for performance analysis.

The aeroshell with added strakes is modeled identically to the rectangular nosed vehicle up until the flap cut is made. The cut flap extrude is positioned on the flap plane at the same height on the base of the vehicle as the other aeroshell variants, but the width of this rectangular sketch that cuts the flap off the back of the vehicle is not as wide as the total span like it is on the rectangular and elliptical waverider aeroshell variants. The width of the cut is fixed to be 1.9m, as be seen in Fig. 2.18. This sketch is extruded to model the strakes, making the aft of the aeroshell appear as it does in Fig. 2.19.

With hopes to reduce heating levels on the strake sharp leading edges, a fillet of 0.125m is imposed on the sharp rectangular corner inside the width of the flap and a fillet of 0.01m is placed on the sharp pointed tip on the strakes. This final configuration of the

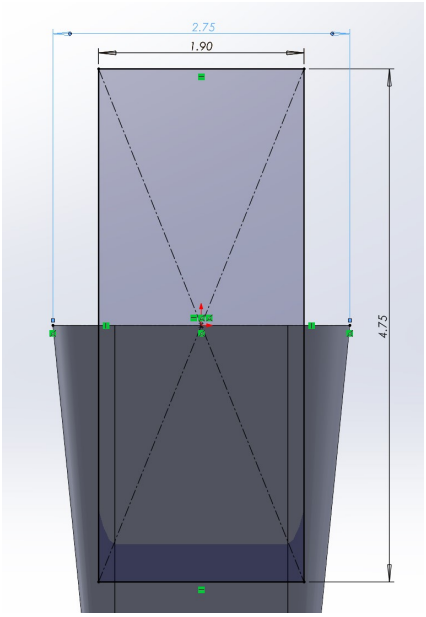

Figure 2.18: Strake cut sketch on flap plane of $R_n = 0.1$ configuration

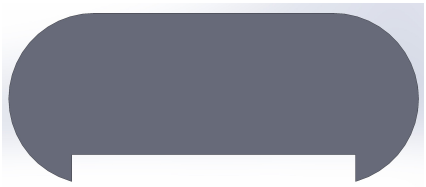

Figure 2.19: Strake cut extrude on flap plane of $R_n = 0.1$ configuration

aft of the vehicle is shown in Fig. 2.20

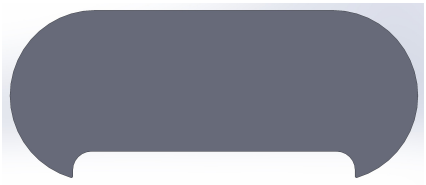

Figure 2.20: Aft view of final strake aeroshell configuration

2.2.4 Wedgerider Design Model

The final waverider aeroshell configuration which has been named the wedgerider, takes inspiration from Kolodziej's developmental work on the SHARP-L1 geometry. This aeroshell increases weathercock stability by reversing the taper and changing from a expanding wedge to a contracting wedge geometry [29] displayed in Fig. 2.21.

Similarly, this geometry is derived from the rectangular nose aeroshell, but has modifications to the sketch which creates the conical sides of the vehicle. The side profile sketch was increased by a length of 0.125m to extend beyond the top height of the wedge for all nose bluntness configurations, shown in Fig. 2.22.

This sketch was similarly revolved and mirrored across the center of the aeroshell, to mimic a contracting wedge geometry profile. Due to the increased height of the conical

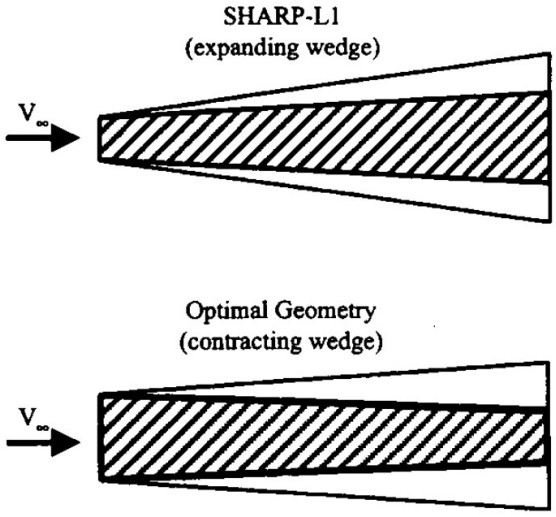

Figure 2.21: Top view of SHARP-L1 model compared to optimal contracting wedge geometry [29]

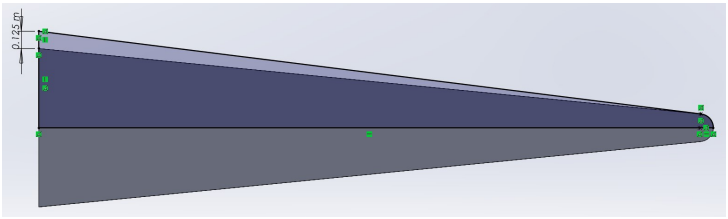

Figure 2.22: Side profile sketch of wedgerider model

side profiles, they create the optimal contracting wedge geometry and create a flat central wedge region to collimate high pressure on the vehicle with the goal of increasing lift performance. This front profile of the wedgerider is seen in Fig. 2.23

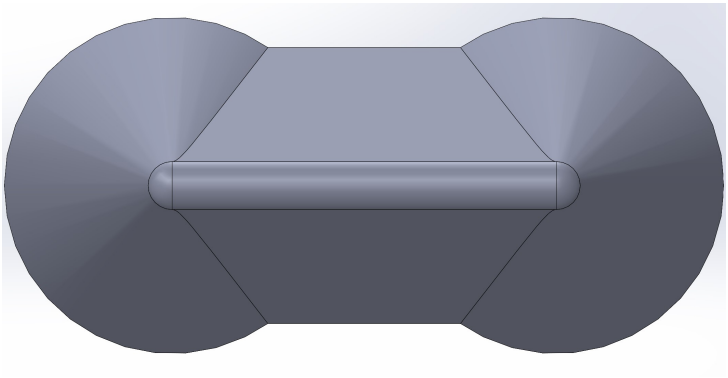

Figure 2.23: Front profile of wedgerider

The flap plane and cut extrude is again placed at the same location of the other aeroshell configurations, and cuts off the base on the along the aft of the vehicle. A fillet of 0.125m is placed upon the lines where the wedge and cone surfaces meet on the top and bottom surfaces of the aeroshell to create a smoother contour along the body of the vehicle, as depicted in Fig. 2.24.

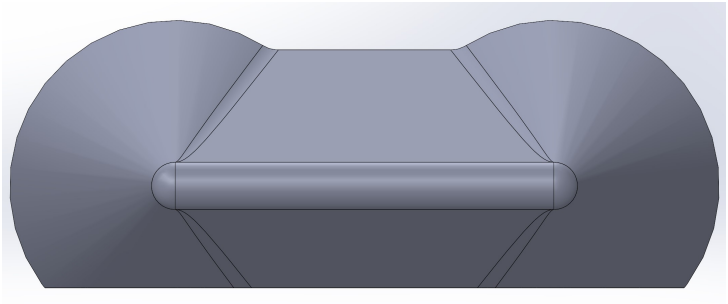

Figure 2.24: Front profile of wedgerider

2.3 Aeroshell Configuration Comparison

This section will discuss the main constants for each model, tabulate dimensions for the range of blunt nose radii across all configurations, and show figures comparing the different profile views. The first table for the rectangular aeroshell constants modeled in the SoidWorks environment are seen in Table 2.1.

Table 2.1: Rectangular nose constant parameters

Constant parameter	**Dimension value**
Flap length	∼1.522 m
Main chord	4.8 m
Main span	1.6 m
Wedge angle	11.26 deg

The constants for the elliptical configuration models are displayed in Table 2.2. Next, the constants for the configurations with strakes attached to the rectangular nose aeroshell are displayed in Table 2.3.

Table 2.2: Elliptical nose constant parameters

Constant parameter	**Dimension value**
Flap length	∼1.522 m
Main chord	4.8 m
Main span	1.6 m
Wedge angle	11.26 deg
Front nose section	0.25 m

Lastly, constants for the wedgerider configuration with a rectangular nose aeroshell are displayed in Table 2.4.

The main constants and blunted nose region can be seen on a drawing of the rectangular nose aeroshell configuration in Fig. 2.25. The parameter variation across the different nose radii of the same waverider configurations are tabulated in A.1 through A.4 in Appendix A. Variations across the different waverider configurations with the same nose radii are tabulated in A.5 through A.8 also in Appendix A of the report.

Different profile views of the waverider configurations are show below in Fig. 2.26 and Fig. 2.30. These illustrations highlight the differences between the geometric waverider aeroshell configurations for this project.

Table 2.3: Strake model constant parameters

Constant parameter	**Dimension value**
Main chord	4.8 m
Main span	1.6 m
Wedge angle	11.26 deg
Strake span	1.9 m
Strake height	0.2 m
Strake fillet	0.125 m

Table 2.4: Wedgerider model constant parameters

Constant parameter	**Dimension value**
Main chord	4.8 m
Main span	1.6 m
Wedge angle	11.26 deg
Top wedge height	0.125 m
Wedge fillet	0.125 m

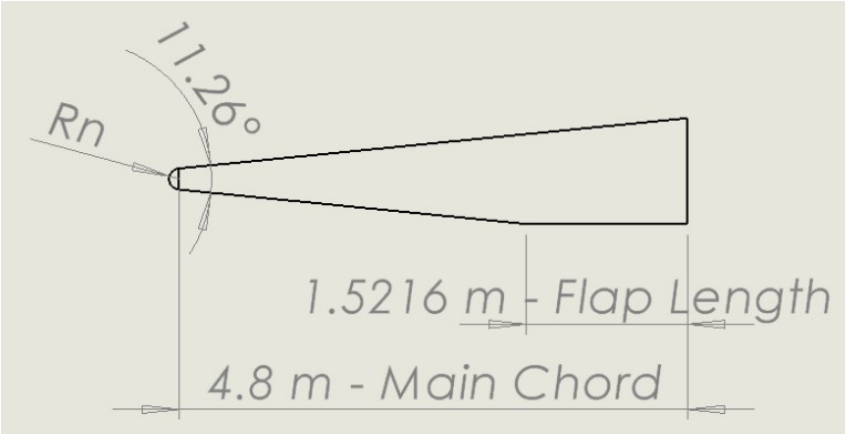

Figure 2.25: Rectangular configuration drawing of main constants and blunted nose

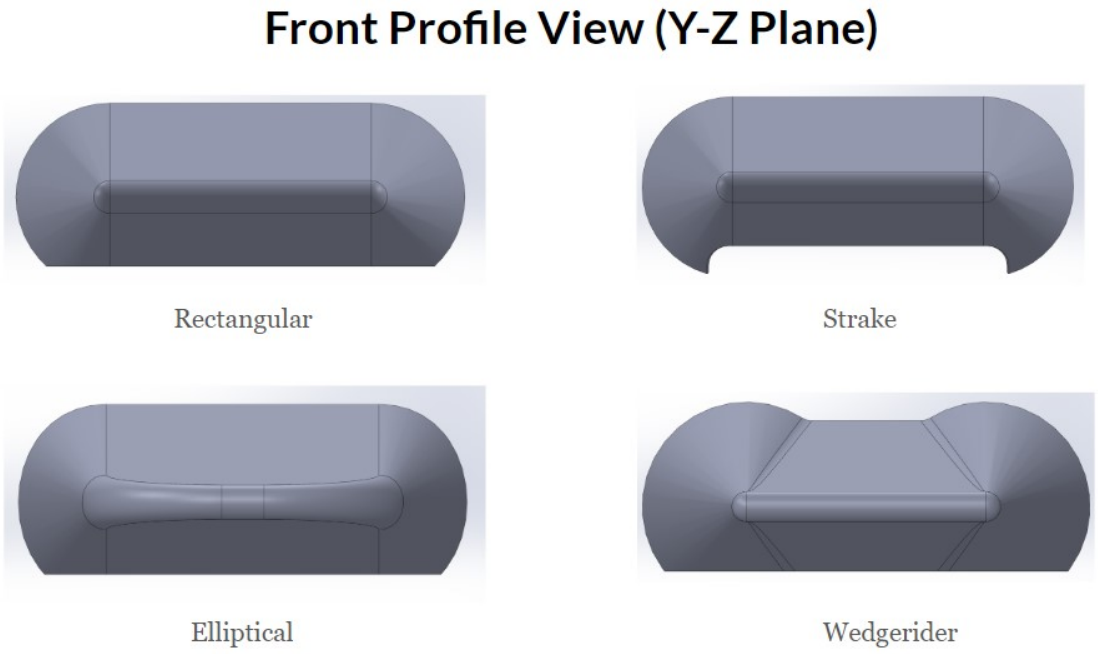

Figure 2.26: Front plane configuration of waverider models with $R_n = 0.1$m

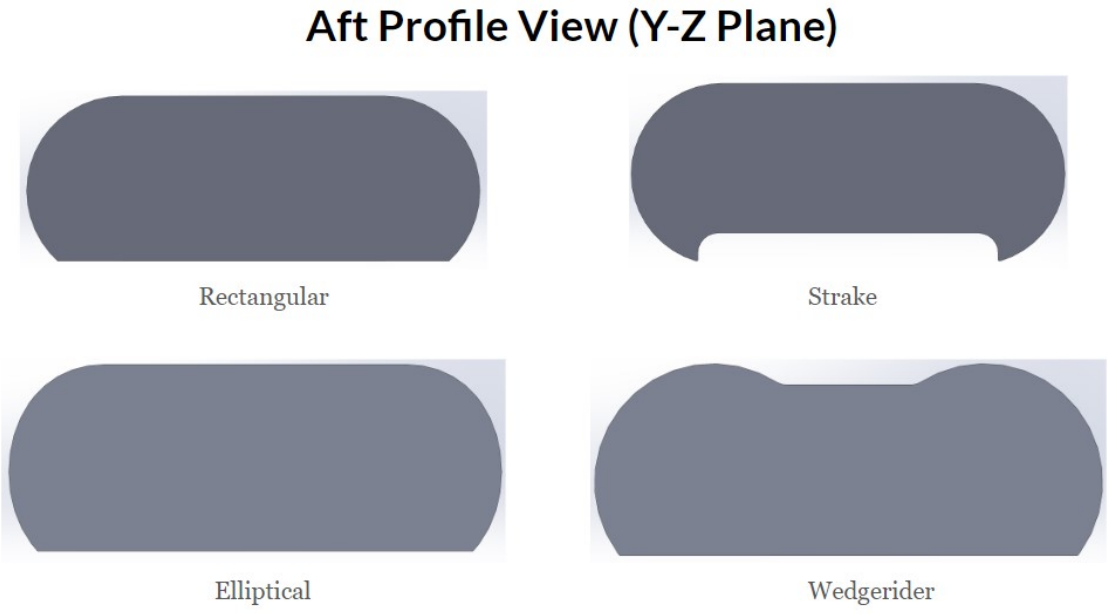

Figure 2.27: Aft plane configuration of waverider models with $R_n = 0.1$m

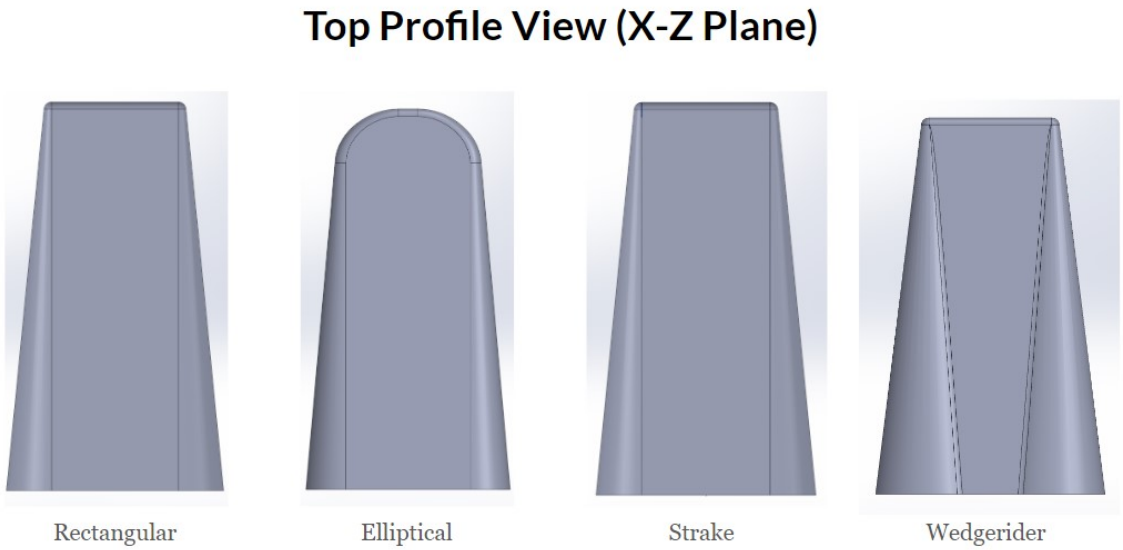

Figure 2.28: Top plane configuration of waverider models with $R_n = 0.1$m

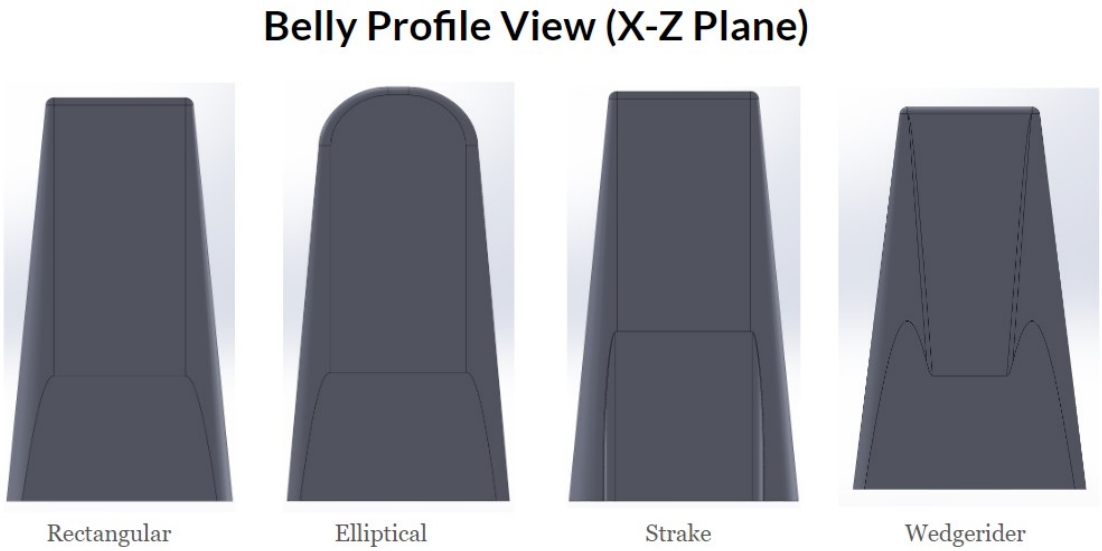

Figure 2.29: Belly plane configuration of waverider models with $R_n = 0.1$m

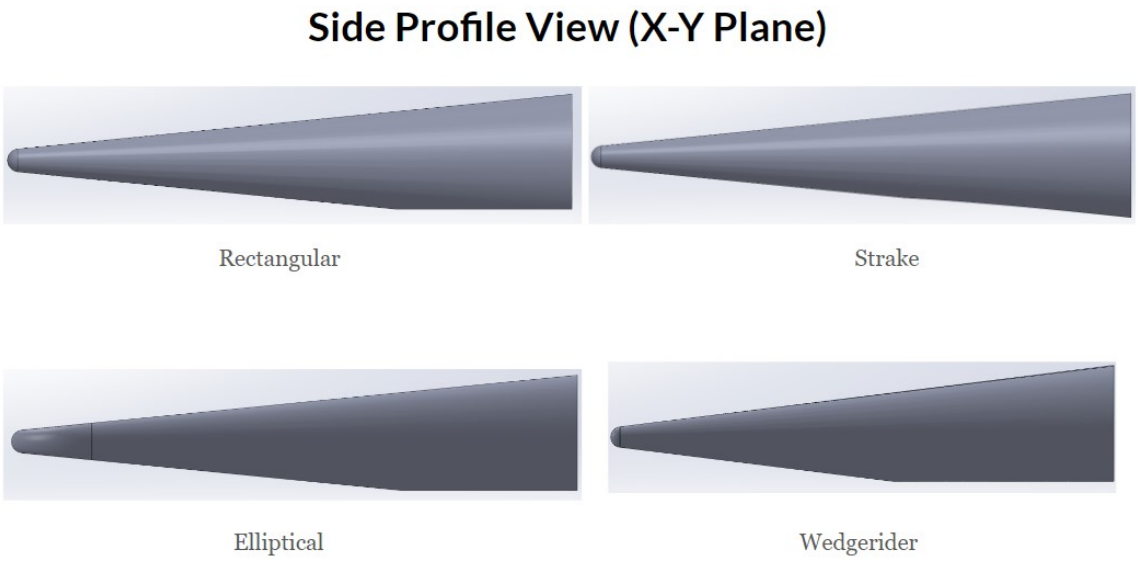

Figure 2.30: Belly plane configuration of waverider models with $R_n = 0.1$m

Chapter 3:

Waverider Aeroshell Mesh Creation

3.1 Surface Meshing

To generate the surface mesh of the various waverider aeroshells analyzed in this project, the program Gmsh was used with .step files exported from the SolidWorks CAD software environment. Gmsh is an open source 3D finite element grid generator with a built-in CAD engine and post-processor [33]. All 2D surface meshes were created in Gmsh, as this program provides a fast, user-friendly meshing tool with parametric input and advanced visualization capabilities [33]. This chapter will discuss the meshing workflow in Gmsh release version 4.21.2 and mesh sizing study in CBAERO for a single waverider aeroshell.

3.1.1 Gmsh Workflow

The Gmsh workflow is quite fast and user friendly; it allows for different .step files to be meshed quickly and exported to the correct file type for analysis in CBAERO. After the Gmsh software is downloaded in the Linux environment (or other relevant operating system being used for analysis), the program must be opened to create a new mesh project. This file should be saved in the desired directory folder, and then it can be merged with a CAD .step file to pull the geometry into the meshing program. All CAD files are sliced in half down the vehicle chord. The half span geometry of the waverider aeroshell is then saved as a .step file. This allows for less intensive computational analysis in CBAERO, as the results can be reflected across the half span of the vehicle. Additionally, discrepancies in symmetry on the unstructured surface mesh of the complete waverider geometric definition can impact the precision of the simulation. The imported geometry for the rectangular nose aeroshell is depicted in Fig. 3.1.

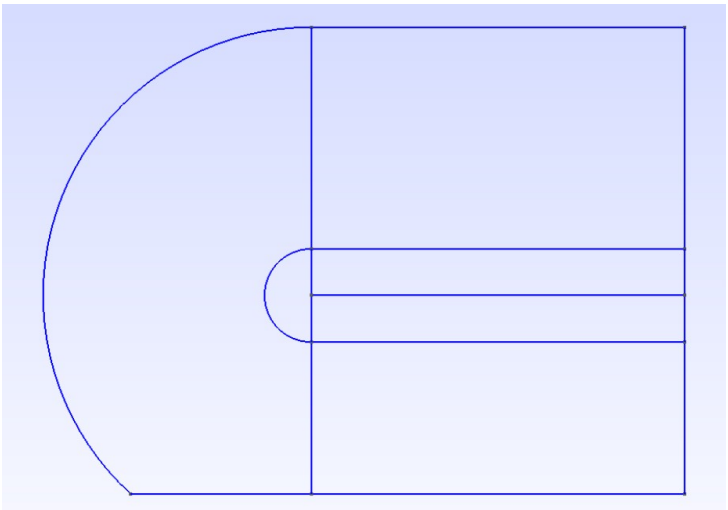

Figure 3.1: Gmsh interface after merging the .step file into the program

To create the mesh, the Mesh module tab must be expanded and the 1D option under the Define section should be selected first. This creates a set of nodes around the outline of the imported geometry, seen in Fig. 3.2. Next, the options menu under tools must be selected for the mesh module as this allows for the general selection of mesh algorithm and element sizing, advanced settings to compute element sizes from curvature regions of the geometry, and allows for changes to the visualization settings.

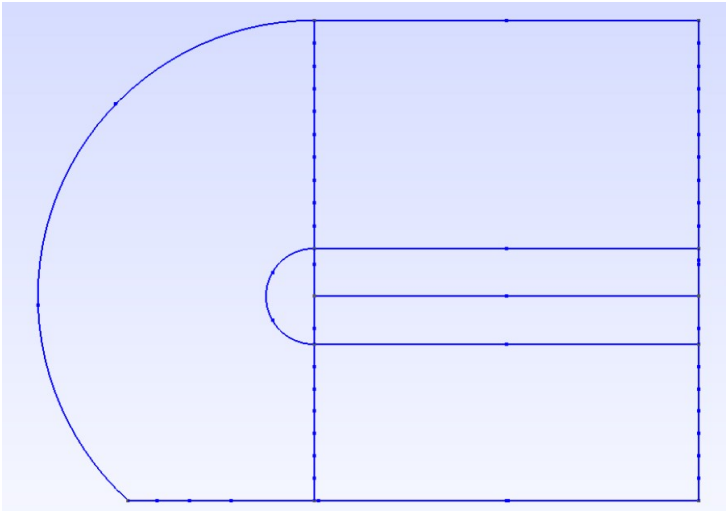

Figure 3.2: Gmsh initial visualization of 1D node mesh

In the general tab of this mesh options menu, the 2D algorithm should be set to MeshAdapt with a simple 2D recombination algorithm. The min element size should be set to zero, and the mesh study looks at the difference between a max element size of 50 and 100 mm. In the visibility tab, the nodes, 2D element edges, and 2D element faces should all be selected. Under the advanced tab of the mesh options menu, the element sizes can be computed by the curvature so a number of points must be input. The mesh study will look at variations of 30, 45, and 60 points around the curvature of the rectangular nose $R_n = 0.1m$ aeroshell.

After selecting these desired options under tools for the mesh module, the 1D option can be selected again, and a one dimensional mesh will regenerate based on the refined settings shown in Fig. 3.3.

Next, the 2D option is selected, which generates a two dimensional surface mesh over the imported geometry as depicted in Fig. 3.4 and Fig. 3.5. This unstructured mesh file then can be exported for CBAERO analysis as a Nastran .bdf file. The mesh can be exported to any desired directory, and the extension .bdf must be added to ensure a readable format for CBAERO. This .bdf file must be saved in the free field format, and then can be read by the surfview command in CBAERO when setting up the geometry mesh file orientation and tagged regions for analysis.

3.2 Mesh Study for CBAERO Analysis

A mesh quality study was performed on the rectangular nosed waverider case with a nose bluntness of $R_n = 0.1m$ in CBAERO. The goal of this study was to look at possible variance in results on the number of element points around the curvature of the body and maximum element sizing of the surface mesh. Dr. Kinney stated that a smooth,

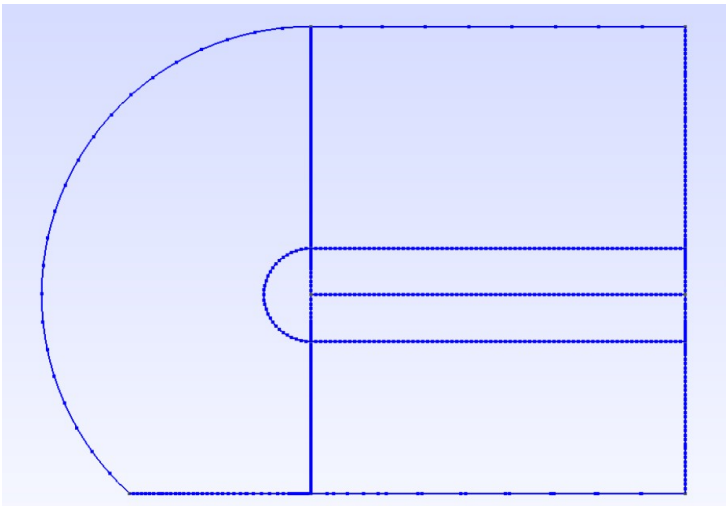

Figure 3.3: Gmsh refined visualization of 1D node mesh

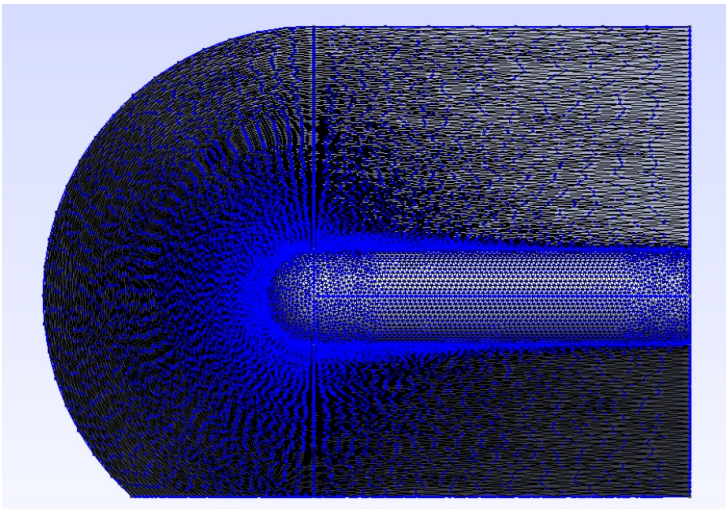

Figure 3.4: Front view of 2D refined mesh on rectangular nose waverider aeroshell

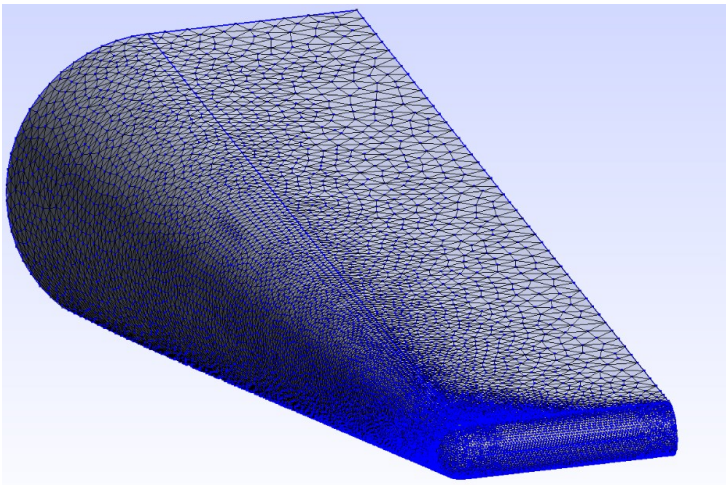

Figure 3.5: Front side profile view of 2D refined mesh

symmetric is best to minimize deviations in computational results. The surface mesh does not require excessive points along the vehicle for a accurate CBAERO solution, however the leading edge of the aeroshell nose requires a finer mesh to reduce noise and allow attachment lines to pass through the surface. The assumptions and the underlying physics of CBAERO will be further discussed in Chapter 5.

For the mesh study, an element sizing of 30, 45, and 60 points around the aeroshell curvature and maximum element sizing of 50 and 100 mm were analyzed. These curvature points and maximum element sizing were smaller than what is required of CBAERO per Dr. Kinney's direction, and results proved to be uniform across all test cases. Results of the mesh study for two cases along a reference AGA trajectory are presented in this section.

The first case of the mesh study is at Mach 40 and an altitude of 85 km, which corresponds to a dynamic pressure of nearly 4.99×10^{-2} bars. Aerodynamic performance plots of the coefficient of lift, drag, and lift to drag ratio can be seen in Fig. 3.6, Fig. 3.7, and Fig. 3.8. All plots of varying mesh sizing and curvature points are in extremely close agreement and overlap, appearing as if only a few mesh configurations were studied while all six cases are plotted.

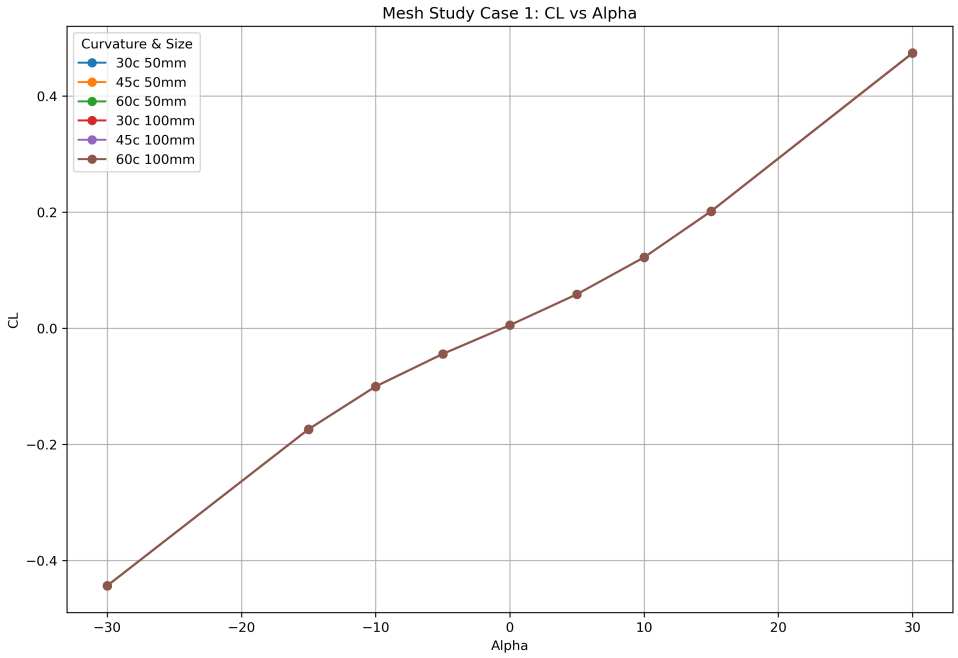

Figure 3.6: Coefficient of lift results for mesh study case 1

The second case of the mesh study is at Mach 45 and an altitude of 60 km, which corresponds to a dynamic pressure of about 0.311 bars. Like the first case, aerodynamic performance plots of the coefficient of lift, drag, and lift to drag ratio can be seen respectively in Fig. 3.9, Fig. 3.10, and Fig. 3.11. Again, extremely close agreement can be seen for the different aeroshell surface meshes.

This mesh quality study provided confidence that there was not going to be extreme variations due to the mesh sizing or curvature. For all aeroshell variants, a maximum mesh size of 100 mm was selected. For the elliptical and rectangular nose waveriders, 60 points were used to compute element size from curvature. For the waverider aeroshell model with strakes, 30 points were used to compute element size from curvature, as the

strakes on the tail and fillets presented very small regions of curvature for the mesh to cover. The wedgerider aeroshell model had 45 points to compute element size from curvature, as the fillets around the top and bottom of the vehicle created small curvature regions.

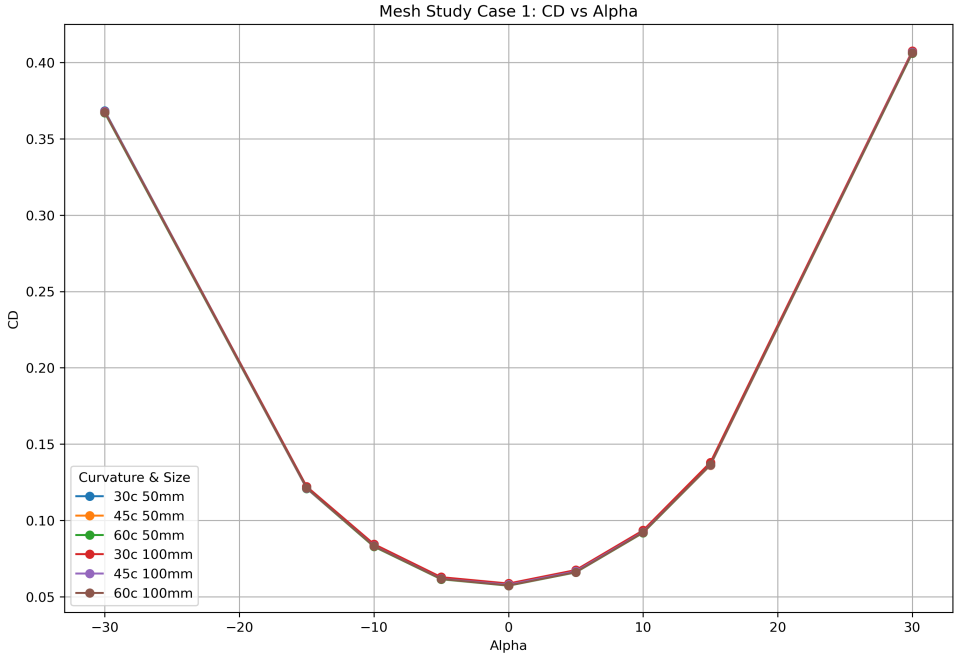

Figure 3.7: Coefficient of drag results for mesh study case 1

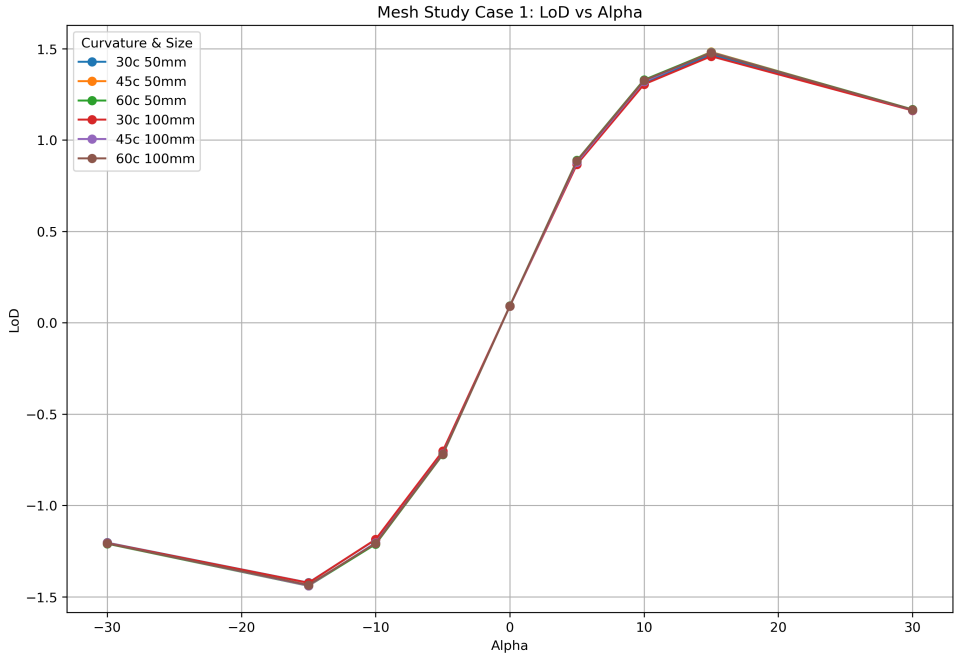

Figure 3.8: Lift over drag results for mesh study case 1

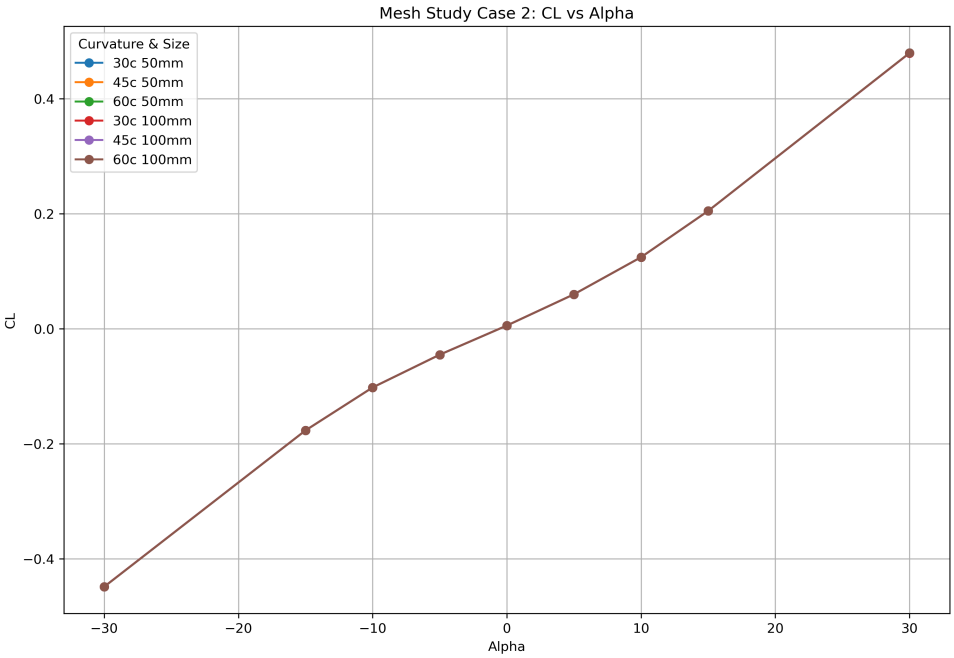

Figure 3.9: Coefficient of lift results for mesh study case 2

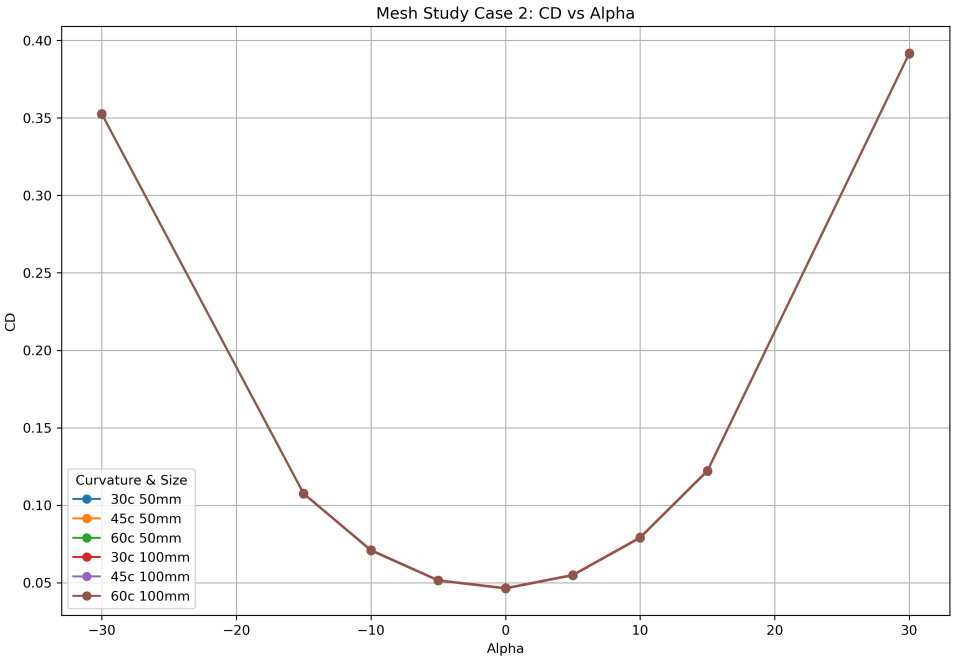

Figure 3.10: Coefficient of drag results for mesh study case 2

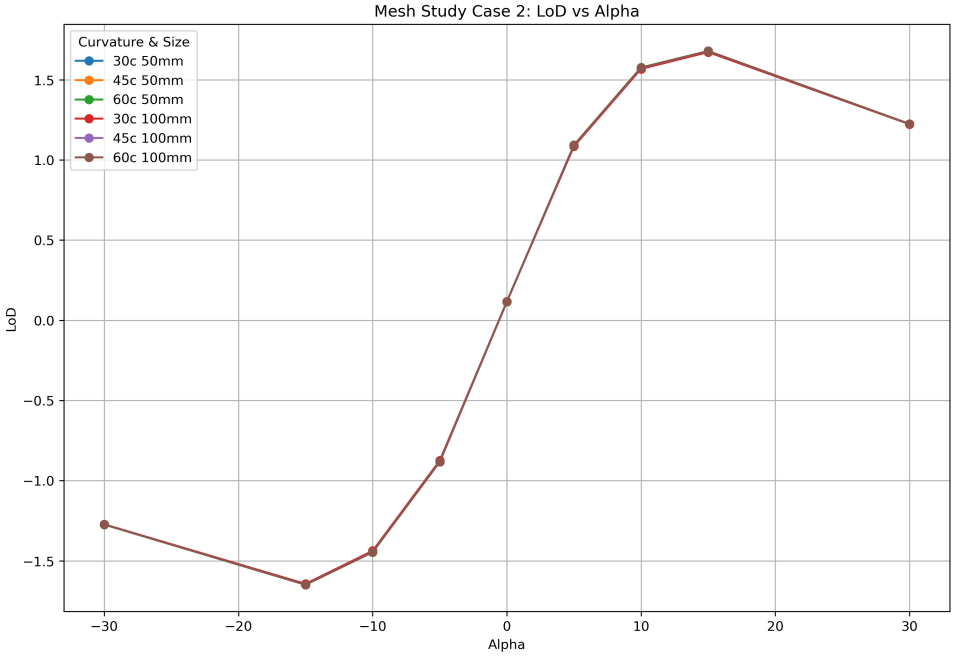

Figure 3.11: Lift over drag results for mesh study case 2

Chapter 4:

Mathematical Models

To identify waverider configurations with promising hypersonic aerothermal performance for Earth AGA, this chapter will discuss governing equations relevant to implementation of an AGA trajectory maneuver, explore critical hypersonic relations, and relevant thermal models to provide a mathematical basis of understanding for the AGA maneuver and the physical affects present in the aerothermal environment.

4.1 AGA Governing Equations

For an incoming spacecraft with relative velocity V_∞ embarking on a simple hyperbolic orbital trajectory approaching a primary gravitational source without leveraging an aeroassisted maneuver[21], it accelerates the object to a velocity

$$V(r) = \sqrt{V_\infty^2 + \frac{2\mu}{r}} \tag{4.1}$$

The spacecraft will leave the planet and return to a velocity of V_∞ after turning through an angle driven by the radius of periapsis [21], signifying the closest approach to the planetary body.

$$\delta = 2\sin^{-1}\left(\frac{1}{1+\frac{r_p V^2}{\mu}}\right) \tag{4.2}$$

A trajectory with AGA maneuver will augment the natural gravitational bending of the flight path the spacecraft [4], acting to either decrease or increase it's heliocentric velocity. The focus of this project is on an AGA maneuver which increases the spacecraft velocity, as the goal is to reduce transit times to distant objects in the Solar System. The relation is best understood in terms of velocity vectors in heliocentric coordinates, shown in Fig. 4.1.

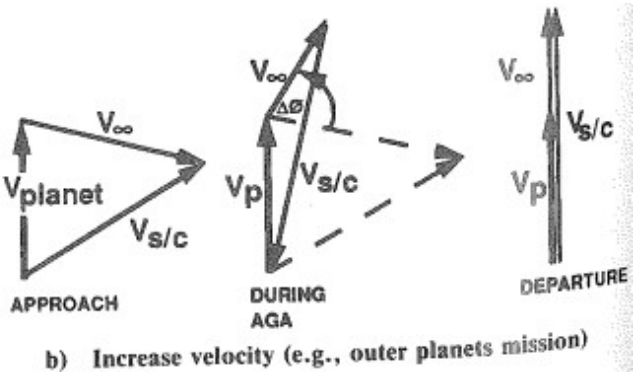

Figure 4.1: Heliocentric velocity coordinates for planet and spacecraft when undergoing an AGA maneuver to increase velocity of the spacecraft [4]

The vectors V_p and $V_{s/c}$ in Fig. 4.1 represent heliocentric velocities of the planet and spacecraft, while V_∞ represents the hyperbolic excess velocity of the spacecraft relative to the planet. Heliocentric velocity refers to the velocity of the body or object around the Sun while hyperbolic excess velocity is the velocity specific to the spacecraft relative to the planet at a very large distance where gravitational influence of the planet is negligible.

To perform an AGA maneuver, the spacecraft approaches the planet with an initial hyperbolic excess velocity, relative to the planet. As the spacecraft enters the atmosphere for the maneuver, it encounters aerodynamic forces of lift and drag while under gravitational influence from the planetary body. This atmospheric passage provides flexibility to modify the flight direction of the spacecraft, with the constraint of velocity will be lost due to drag[21] which will result in heating on the skin of the vehicle. Dynamic pressure is the kinetic energy per unit volume of a fluid flow, defined as q_∞ for free stream conditions.

$$q_\infty = \frac{1}{2}\rho_\infty V_\infty^2 \tag{4.3}$$

Dynamic pressure can be used to simplify the forces of lift and drag, which are defined as:

$$L = q_\infty S C_L \tag{4.4}$$

$$D = q_\infty S C_D \tag{4.5}$$

The lift generated by the spacecraft aeroshell and the gravity of the planet create a centrifugal effect that will change the trajectory and velocity while not requiring fuel. As the vehicle enters the atmosphere, it experiences deceleration dV based off the drag force divided by the mass of the spacecraft [21]. This relation can be further characterized in terms of the aeroshell L/D ratio.

$$dV = -\frac{D}{m}dr = -\frac{L}{(L/D)m}dr \tag{4.6}$$

Velocity losses due to drag in the atmosphere can be minimized by changing the angle of attack of the waverider aeroshell for peak performance throughout the trajectory. Lift can be reduced by changing angle of attack, increasing flight altitude, or both [11]. This will alter the lift and drag coefficients of the aeroshell, thus the L/D ratio which controls the aerodynamic forces experienced during the maneuver. Increasing flight altitude has minimal effects on the performance coefficients, as it changes the magnitude of lift by reducing the ambient density which lift is proportional to and increase the drag coefficients from viscous effects [11]. The time of atmospheric flight is related to the arc length, Θ, traveled at a given radius in the atmosphere. This relationship is described by the following equation.

$$V dt = r d\Theta \tag{4.7}$$

If constant-altitude flight is assumed to be achieved for the bulk of the atmospheric flight, lift must be used to add to gravitational forces to counter excess centrifugal effects [21]. Lift is positive, acting towards the planet as it is augments the gravitational force. This is the reason why the waverider must fly upside-down with respect to the planet's surface, as it is using lift to stay in the atmosphere. This enables the force balance

equation to be rewritten, and the deceleration term to be expressed in terms of the angle of the arc through the atmosphere.

$$L + \frac{v_m m}{r^2} = \frac{mV^2}{r} \tag{4.8}$$

$$dV = -\frac{L}{(L/D)m}dr = -\frac{L}{m}\left[\frac{1}{L/D} - \left(\frac{v_p}{V} - \frac{v_p}{\sqrt{\mu/r}}\right)\right]d\Theta \tag{4.9}$$

This equation can be integrated to express velocity as a function of Θ provided the variation of L/D is known with flight velocity. Dominate variation of aeroshell performance will result from reduced lift requirements as flight velocity is lost to drag, as L/D should be relatively insensitive to changes in Mach number alone during high Mach flight [21]. Assuming a constant L/D, the vehicle will travel through angle Θ for a given altitude, r.

$$\Theta = -\left[\frac{L}{D}\right]_{V_1}\int_{V_1}^{V_2}\frac{dV}{V - (\frac{v}{r}V)} = -\frac{1}{2}\frac{L/D}{V}\left(\frac{V^2}{r} - \left(\frac{\mu}{r}\right)\right) \tag{4.10}$$

This enables atmospheric exit velocity to be written in terms of the entrance velocity, as a function of the angle swept through atmospheric flight [11].

$$V_2 = \sqrt{\exp\left[\frac{-2\Theta}{(L/D)}\right]V_1^2 + \exp\left[\frac{-2\Theta}{(L/D)}\right] - 1}\left(\frac{v}{r}\right) \tag{4.11}$$

As the parameter of interest is the exit velocity as the aeroshell leaves the atmosphere after AGA, the final velocity at an infinite distance from the gravitational well of the planet can be expressed in terms of the relative approach velocity [11].

$$V_{\infty 2} = \sqrt{\exp\left[-\frac{2\Theta}{(L/D)}\right]V_{\infty 1}^2 + \exp\left[-\frac{2\Theta}{(L/D)}\right] - 1}\left(\frac{v}{r}\right) \tag{4.12}$$

As the spacecraft completes the AGA maneuver, it will exit the atmosphere with a new hyperbolic excess velocity. While aerodynamic losses are present due to drag from the portion of atmospheric flight, the gravitational assist from the planet leads to a net gain of heliocentric velocity. This can be coupled with a propulsive burn to further accelerate flight transit times to the outer solar system. The vector relation for hyperbolic exit velocity of the AGA maneuver is equal to the hyperbolic approach velocity before the maneuver minus aerodynamic losses with a propulsive burn (V_{pr}) is characterized below.

$$V_{\infty 2} = V_{\infty 1} - \Delta V_\infty + V_{pr} \tag{4.13}$$

In the above equation, the velocity losses due to drag ΔV_∞ are determined by the following relation found in [4].

$$\frac{\Delta V_\infty}{V_{\infty 1}} = -\frac{\Theta}{(C_L/C_D)}\left[1 + \left(\frac{V_c}{V_\infty}\right)^2\right] \tag{4.14}$$

This equation assumes equilibrium flight conditions (constant L/D) and requiring a slight increase in atmospheric density as velocity decreases during the AGA maneuver. The drag forces present in planetary atmospheres decreases the incoming velocity by the

amount governed by the exponential scale factor $2\Theta/(L/D)$ and turn angle ϕ including the gravity and atmospheric components is given below [11].

$$\phi = \Theta + \sin^{-1}\left(\frac{1}{1+rV^2/\nu}\right) + \sin^{-1}\left(\frac{e^{(2\Theta/U)/(L/D)}}{1+rV^2/\nu}\right) \tag{4.15}$$

CBAERO provides the atmospheric density model for this project, as it has built in tables for all planets. Atmospheric density is critical for calculations of stagnation point convective heating and radiative heating, and with limited assumptions it can be modeled strictly as an exponential equation. Note that B is the inverse constant scale height of Earth's atmosphere, and ρ_0 and R_0 are reference density and altitude values [9].

$$\rho = \rho_0 \exp\left[-\mathbf{B}(r - R_0)\right] \tag{4.16}$$

4.2 Hypersonic Aero-thermodynamic Phenomena

This section discusses relevant hypersonic aero-thermodynamic equations for this report. The waverider aeroshell undergoing an AGA trajectory maneuver will be traveling at very high mach numbers during the atmospheric flight region. As the waverider descends to lower regions of the atmosphere, the density of air will increase leading to stronger drag forces and intense heating due to more interactions with gas molecules. Anytime a supersonic flow is turned into itself, such as a flow over or wedge or compression corner, a shockwave is created [17]. For a body in hypersonic flow with a profile that angles away from the free stream of the flow, an expansion wave will be created at this corner and spread downstream [17]. Relations for oblique shock waves and expansion waves are discussed in this section. Additionally, thermal models for convective and radiative heating in the hypersonic flight environment are presented.

4.2.1 Shock Waves

A shock wave is an extremely thin region of the fluid domain across which large changes in flow parameters like density, pressure, temperature, velocity, viscosity, and other parameters occur. When sufficiently high back pressure is created downstream of the supersonic flow, a standing shock wave will be established along the body profile [17].

The orientations of shock waves that can occur during hypersonic flight are normal shocks, oblique shocks, and curved bow shocks. A normal shock occurs perpendicular (normal) to the direction of the free stream of the flow, while oblique shock waves occur when the body profile is at an angle towards the free stream. A bow shock will occur due to a curved body, and is commonly seen on the blunt faces of capsules or at the tip of a blunted nose during hypersonic flight. As the waveriders discussed in this report originate from a wedge profile which provides an angle towards the free stream, equations for oblique show waves will be discussed.

The geometry of an oblique shock wave can be seen in Fig. 4.2. The angle of the shock is given by the parameter β, while the parameter θ describes the deflection angle of the wedge geometry in the flow field.

Assuming that air behaves as a calorically perfect gas, the ratio of specific heats are constant and the ideal gas law will govern relationships between pressure, density and temperature of the gas. These expressions are seen below.

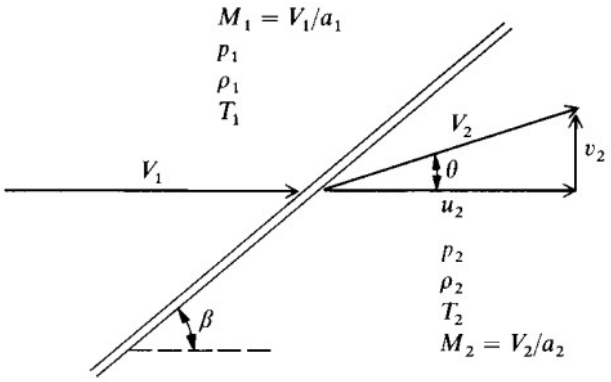

Figure 4.2: Geometry of oblique shock wave [17]

$$\gamma = \frac{c_p}{c_v} \tag{4.17}$$

$$P_\infty = \rho_\infty R T_\infty \tag{4.18}$$

Enthalpy is the total energy of a thermodynamic system, which can be expressed as the following for an ideal gas:

$$h = C_p T \tag{4.19}$$

The methodology for solving the following relations for conditions up and downstream of a shock wave use the three main conservation laws. Assuming a constant area, conservation of mass is given by the following relation:

$$\rho_1 v_1 = \rho_2 v_2 \tag{4.20}$$

The conservation laws of momentum and energy are given by the next two respective relationships:

$$p_1 + \rho_1 v_1^2 = p_2 + \rho_2 v_2^2 \tag{4.21}$$

$$h_2 + \frac{v_2^2}{2} = h_1 + \frac{v_1^2}{2} \tag{4.22}$$

Due to conservation of momentum, the tangential component of the oblique shock wave is conserved and the normal component is what crosses the shockwave and impacts the body. If working with normal shock equations, the trigonometric term with shock angle β is dropped as the whole shock value will be normal to the vehicle body. The normal component of an oblique shock wave is given the relation:

$$M_{1_{\text{normal}}} = M_1 \sin(\beta) \tag{4.23}$$

Using this framework with the normal component of an oblique shock wave, the exact relation for pressure ratio [17] is given by the following:

$$\frac{p_2}{p_1} = 1 + \frac{2\gamma}{\gamma+1}\left(M_1^2 \sin^2\beta - 1\right) \tag{4.24}$$

However, for very high Mach flight which is experienced during the AGA maneuver, the plus and minus 1 terms are extremely small in relation to the other terms, so they can be dropped. This simplifies the pressure relation to:

$$\frac{p_2}{p_1} = \frac{2\gamma}{\gamma+1} M_1^2 \sin^2\beta \tag{4.25}$$

Similar adjustments can be made to the density and temperature ratios for oblique shock waves [17]. The density ratio is expressed as:

$$\frac{\rho_2}{\rho_1} = \frac{\gamma+1}{\gamma-1} \tag{4.26}$$

Using the ideal gas law, (also known as the equation of state), enables us to relate the temperatures across the shock wave as the following:

$$\frac{T_2}{T_1} = \left(\frac{p_2}{p_1}\right)\left(\frac{\rho_1}{\rho_2}\right) \tag{4.27}$$

Pressure distributions are presented in terms of the non-dimensional pressure coefficient, C_p. This relation is defined below and can be determined for the high mach limit behind an oblique shock wave [17] in terms of the ratio of specific heats and shock angle.

$$C_p = \frac{p_2 - p_1}{q_1} = \left(\frac{4}{\gamma+1}\right)\sin^2\beta \tag{4.28}$$

This ratio can also be expressed in the parameters of Mach, β, and γ.

$$\frac{T_2}{T_1} = \frac{2\gamma(\gamma-1)M_1^2\sin^2\beta}{(\gamma+1)^2} \tag{4.29}$$

There is a close relationship between Mach number, the shock angle β, and defelction angle θ, as shown plotted in 4.3. This exact relationship is characterized by the equation:

$$\tan\theta = 2\cot\beta\left[\frac{M_1^2\sin^2\beta - 1}{M_1^2(\gamma + \cos 2\beta) + 2}\right] \tag{4.30}$$

Assuming the small angle approximations in Equation 4.31 and the high mach numbers which correlate to an AGA maneuver, the deflection angle θ can be expressed as:

$$\sin\beta \approx \beta, \quad \cos 2\beta \approx 1, \quad \tan\theta \approx \sin\theta \approx \theta \tag{4.31}$$

$$\theta = \frac{2}{\beta}\left[\frac{M_1^2\beta^2}{M_1^2(\gamma+1)}\right] \tag{4.32}$$

This can be expressed simply in terms of the ratio of shock angle β to deflection angle θ:

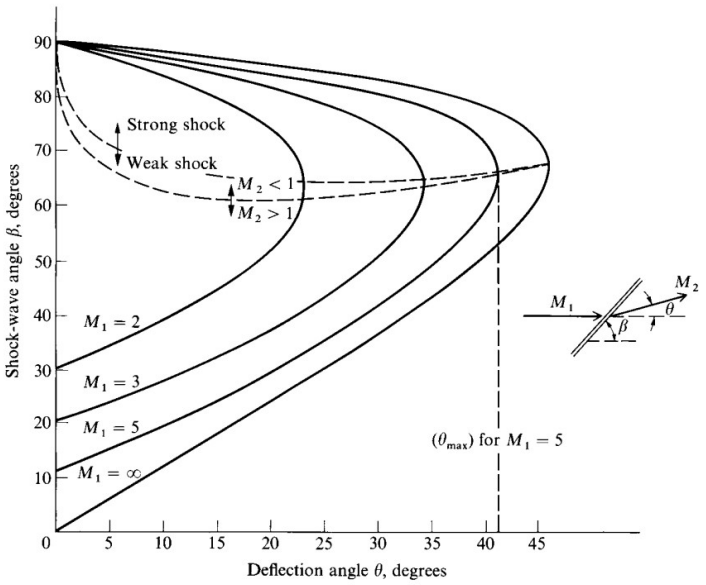

Figure 4.3: Theta beta mach diagram [17]

$$\frac{\beta}{\theta} = \frac{\gamma + 1}{2} \tag{4.33}$$

4.2.2 Expansion Waves

A geometry in the hypersonic flow environment with a profile that angles away from the free stream will be create an expansion wave at this location. For the waverider aeroshell, this phenomena can occur along the top, bottom, or flap region of the waverider geometry depending on the given AoA orientation to the flow. A diagram of an expansion wave can be seen depicted in Fig. 4.4.

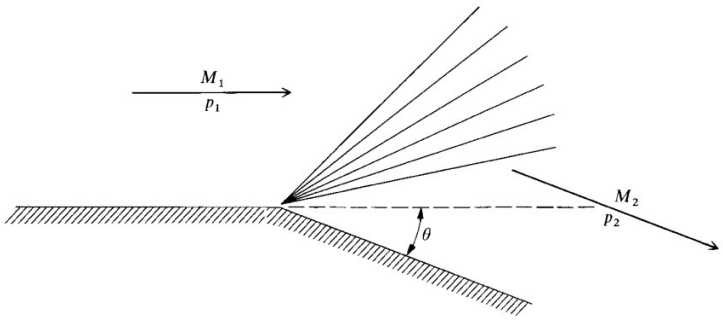

Figure 4.4: Expansion wave geometry[17]

The deflection angle, θ, of an expansion wave is given by the difference in the Prandtl-Meyer function at the given mach numbers upstream and downstream from the deflection corner.

$$\theta = \nu(M_2) - \nu(M_1) \tag{4.34}$$

Where the Prandtl-Meyer function, $\nu(M)$, is defined by the following equation:

$$\nu(M) = \sqrt{\frac{\gamma+1}{\gamma-1}} \tan^{-1} \sqrt{\frac{\gamma-1}{\gamma+1} M^2 - 1} - \tan^{-1} \sqrt{M^2 - 1} \tag{4.35}$$

The relation for deflection angle can be simplified in terms of γ and mach for high mach numbers found in the AGA environment.

$$\theta = \frac{2}{\gamma - 1} - \left(\frac{1}{M_1} - \frac{1}{M_2} \right) \tag{4.36}$$

This simplification for θ enables the pressure ratio across the expansion wave at hypersonic velocities to be expressed as:

$$\frac{p_2}{p_1} = \left(1 - \frac{\gamma - 1}{2} M_1 \theta \right)^{\frac{2\gamma}{\gamma-1}} \tag{4.37}$$

In a similar manner to the oblique shock wave relations, the density and temperature relations can be obtained for upstream and downstream conditions of expansion waves using the ideal gas law and isentropic relations.

4.2.3 Heating Models

The hypersonic flight environment can experience both convective and radiative heating during atmospheric flight, depending on entry velocity. Convective heating on the waverider aeroshell depends on the atmospheric gas composition surrounding the planet [39]. Assuming thermochemical equilibrium of the gas species, the convective heating of the stagnation point is calculated from the following equation. The parameter, k, is dependant on atmospheric composition while h_w is the enthalpy at the wall, which can be neglected when $h_w << h_\infty$. This hot wall correction term is found to be negligible above 100 W/cm^2 assuming radiative equilibrium [18].

$$\dot{q}_{\text{conv}} = k \left(\frac{\rho}{R_n} \right)^{\frac{1}{2}} \left(V^3 \right) \left(1 - \frac{h_w}{h_\infty} \right) \tag{4.38}$$

$$k_{\text{Earth}} = 1.7415 \times 10^{-4} \tag{4.39}$$

Convective heating is known to be strongly influenced by boundary layer development and flow separation. As the radius of curvature increases on the leading edge of a vehicle or blunt face, the boundary layer over the surface becomes thicker and inherently more stable. This change can decrease the convective heat transfer coefficient, as a thicker boundary layer can act as an insulator reducing the heat flux from the hot gas to the surface of the entry vehicle. For leading edges with larger the radii of curvature, the experienced flow separation can be delayed or reduced. The more attached the flow is to the aeroshell, the more uniform the convective heating pattern will be when compared to a sharper leading edge. Hypersonic flow turning over a small radius can create localized hot spots and will drive convective heating rates up. Governing equations specific for aerothermal assumptions in CBAERO software are discussed in Chapter 5, Section 1.

The computation of radiative heating of a body is a complex, nonlinear procedure dependant upon flight speed, freestream density, and body radius [40]. This model

assumes thermochemical equilibrium exists In this equation, K, is a constant that is atmospheric dependant, r_n is the hemispherical nose radius in m, and $f(V)$ is tabulated values that are functions of flight velocities and atmospheric composition [40]. Radiative heating flight velocity parameters [40] can be found for Earth in Table B.1, located in Appendix B.

$$\dot{q}_{\text{rad}} = K r_n^a \rho^b f(V) \tag{4.40}$$

At very high Mach numbers, atmospheric gases will dissociate and become a partial ionized plasma. Radiative heating rates for Earth, Venus, and Mars become approximately equal at these entry velocites [7]. The following values are accepted for air:

$$\begin{aligned} K &= 4.736 \times 10^4, \\ a &= 1.072 \times 10^6 V^{-1.88} \rho^{-0.325}, \\ b &= 1.22. \end{aligned} \tag{4.41}$$

Radiative heating on hypersonic vehicles is primarily influenced by the shock layer front of the blunt leading edge and becomes critically relevant as velocities exceed 11 km/s. Shock layer thickness and standoff distance are key factors governing the radiative heat flux to the walls of the aeroshell. A gas bubble will occur in front of the stagnation region, consisting of slower moving fluid at a higher temperature before the leading edge of the aeroshell. This stagnation region is where the gas is ionized and heated to extremely high temperatures from compression and friction of the hypersonic flight environment. Most all radiation heating comes from within the subsonic gas bubble that sits in front of the leading edge of the vehicle. A sonic line must attach where the flow turns from subsonic at the stagnation point to supersonic where the curvature changes. Beyond the high temperature subsonic bubble, radiation heat flux should cool off quickly. The subsonic bubble is volumetric, with higher radiative heat flux values occurring from larger volumes. Increasing the radius of curvature makes the shock thicker, thus leading to higher absorption and emission of radiation within the subsonic gas bubble. A larger radius tends to result in a greater shock standoff distance from the vehicle wall, which can affect the view factor, distribution, and intensity of radiative heating. While radiative heat flux generally increases with radius as compression and friction drive high gas temperatures, this heat flux may eventually level off or decrease due to geometric spreading and absorption within the shock layer across the blunt body or aeroshell.

Chapter 5:

Computational Analysis with CBAERO

CBAERO software is utilized for all computational analysis of this report. This program is predictive tool of the aerodynamic and aero-thermodynamic environments of general vehicle configuration [41]. CBAERO is based on accepted engineering level analysis for the estimation of both aerodynamic and aerothermal environments, and can be used for prediction of convective and radiative heating environments [34].

5.1 Physics Assumptions and Governing Equations

The geometry definition in CBAERO requires a surface mesh of the aeroshell OML for each waverider configuration input to the solver. For hypersonic Mach numbers, the inviscid solution is based on independent panel methods [34] and uses the Modified-Newtonian formulation for this analysis. This independent panel method provides the pressure at each surface triangle, and the entropy at each panel is taken equal to the post normal shock entropy [41]. The known value of pressure and entropy at each panel fixes the thermodynamic state at the edge of the boundary layer, and a CEA lookup code is used to calculate remaining thermodynamic properties such as enthalpy and temperature [41]. An equilibrium air model is used to define thermodynamic properties and relationships.

The surface streamline pattern for supersonic and hypersonic flows uses the following approximation to find the surface velocity magnitude [34]:

$$\vec{V}_{\text{surface}} = \hat{n} \cdot \vec{V}_{\infty} \cdot \hat{n} \tag{5.1}$$

This approximation defines the entire surface velocity flow field, with $\hat{n}$ representing the local surface normal and $\vec{V}_{\infty}$ defining the free stream velocity vector. This independent panel method will only provide scalar thermodynamic properties, as there is no direction for surface velocity given it is a magnitude. The streamline pattern is traced over the entire vehicle in reverse until the stagnation point is reached [41]. Streamlines are generated until every node and triangle in the mesh has a nearby streamline from which the distance to the stagnation point or attachment line can be calculated [34]. The ordinary differential equations for 3D streamlines are constrained to the vehicle surface and solved over given surface triangle element until the edge is reached [42].

After definition of the inviscid surface flow field, streamline patterns, stagnation point, and attachment lines, the viscous solution over the acerage of the vehicle can be estimated [42]. The running lengths from either the stagnation point or attachment lines are calculated using streamline patterns, with a laminar flat plate reference enthalpy method solving for skin friction coefficient [42].

In CBAERO, the convective heating correlation of Tauber is used to predict the heating at the stagnation point and along attachment lines [41]. For a Newtonian flow

field, this relationship is inversely proportional to the square root of the local surface curvature [42].

$$\dot{q} \propto \frac{du}{ds} \propto \frac{1}{\sqrt{R}} \tag{5.2}$$

Radiative heating is similarly based upon the correlation found by Tauber-Sutton [34], matching Equation 4.40 found in Chapter 4, section 2.3 of this report. To reiterate, that relation is:

$$\dot{q}_{\text{rad}} = K r_n^a \rho^b f(V) \tag{5.3}$$

From these calculated heat rates, an energy balance is assumed for a non conducting wall to be equal the sum of the convective and incident shock-radiative heating for any triangle on the surface [41]. As convective heating depends on final wall temperature, this non-linear relationship must iterated at each triangle [41] over the surface of the aeroshell.

$$\dot{q}_{\text{conv}} + \dot{q}_{\text{rad}} = \sigma \cdot \varepsilon \cdot T_{\text{wall}}^4 \tag{5.4}$$

5.2 Simulation Setup

To run the simulation in CBAERO, the mesh file must first be loaded into the program. CBAERO is able to read Nastran ".bdf" files, but the general purpose viewer in the software, SURFVIEW, must be utilized to create and save a native CBAERO ".msh" file [43]. The command SURFVIEW is used in terminal before the name of the mesh, and the extension must be removed for it to load into the program. The SURFVIEW tool allows scaling, translation, and rotation of the meshes [43]. The mesh must be oriented correctly with the SURFVIEW tool for the simulation to run properly. The correct orientation for proper simulation results is a top down view of the aeroshell OML with the leading edge of the vehicle nose facing to the left, as this side of the waverider will experience the flow first. The aeroshells should be oriented with the flap facing up, mirroring how it would dive into the atmosphere during the entry portion of the maneuver.

Different numbered zones will represent each face of the surface mesh, and the center face of the geometry where the .step file was cut in half should be suppressed. This region is selected by the zone under the Tag Regions menu, and is seen highlighted in blue on the surface of the aeroshell in Fig. 5.1. Once the correct zone is tagged, suppression of this face is toggled by the right hand menu. After running the simulation, the solution will be reflected about the y-axis of the vehicle, so this region will never encounter the flow. This process of properly orienting the waverider geometry and suppressing the center face in SURFVIEW must be completed for all configurations. The new surface mesh is then saved as a merged file and renamed for simulation setup. This orientation is seen in Fig. 5.2 for the elliptical waverider configuration.

The CBSETUP command is then used to initiate the simulation parameters. Under the view menu option, the wire frame and draw CG are selected to visualize the mesh and location of the center of gravity (CG). Under the view settings for wake, the edges, triangle wire, and triangle shading should be turned on. The setup menu option then allows for specification of solver settings, allowing for the bases, wakes, and aerodynamics

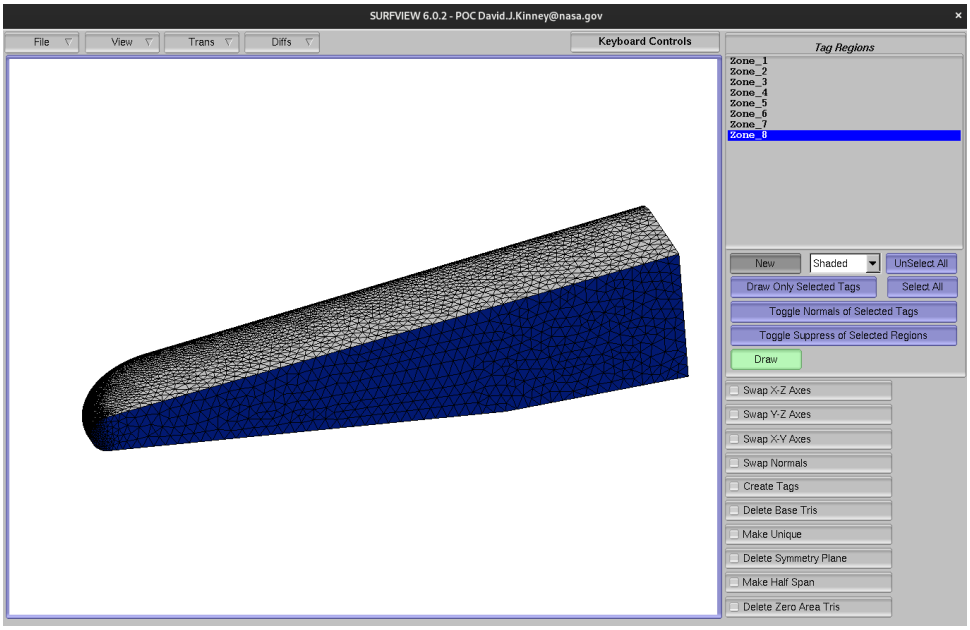

Figure 5.1: Tagged zone in SURFVIEW of half span geometry for suppression

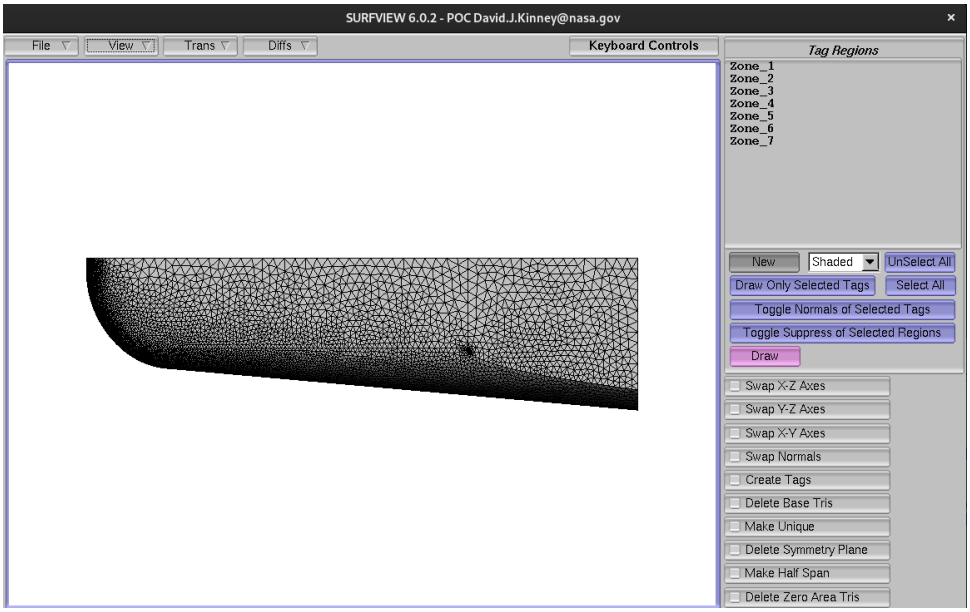

Figure 5.2: Required mesh orientation in SURFVIEW with suppressed central face

to be setup in the software. To correctly set up the simulation, "auto find base triangles" should be selected to automatically find the base regions of the current model [43]. To set up the wakes in the simulation, select autofind VSP wake edges and create VSP wake surface tris. Under the CBAERO defined wakes, auto find wake surface tris, create wake surface tris, and intersect surface tris must be selected. The high speed aerodynamic solver method is set to modified Newtonian for this project. The finalized cbsetup window for the elliptical waverider configuration with can be seen in Fig. 5.3.

The simulation parameter file with extension .cbaero is what controls the specification of solver settings, and the values can be set directly within the file if these settings were not not configured in the cbsetup window. The reference area, chord length, span,

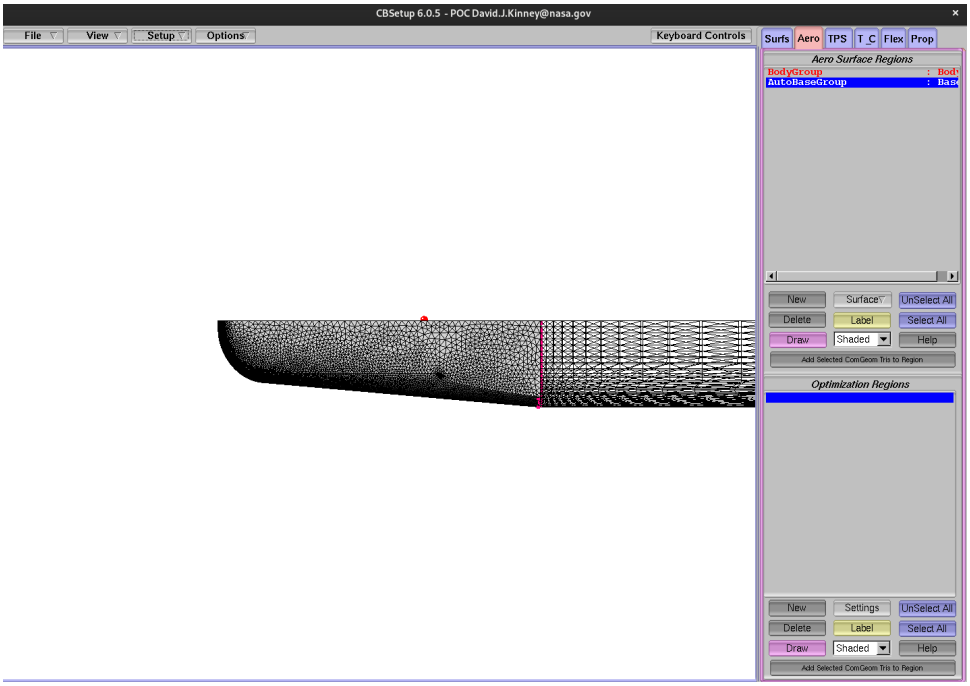

Figure 5.3: Finalized CBSetup window displaying CG, wake edges, and the triangle wake on the elliptical waverider configuration

and CG must be input for each half span aeroshell mesh. After input of the CG values, the red dot displaying the CG in cbsetup should be fixed to the correct location of the vehicle body. The flow type is set to be laminar and the scale factor is adjusted to 0.001 as the mesh is exported in mm. Identical parameter distributions for each aeroshell OML configuration was used, with the specific parameter inputs of Mach number, dynamic pressure, and AoA is seen in Fig. 5.4

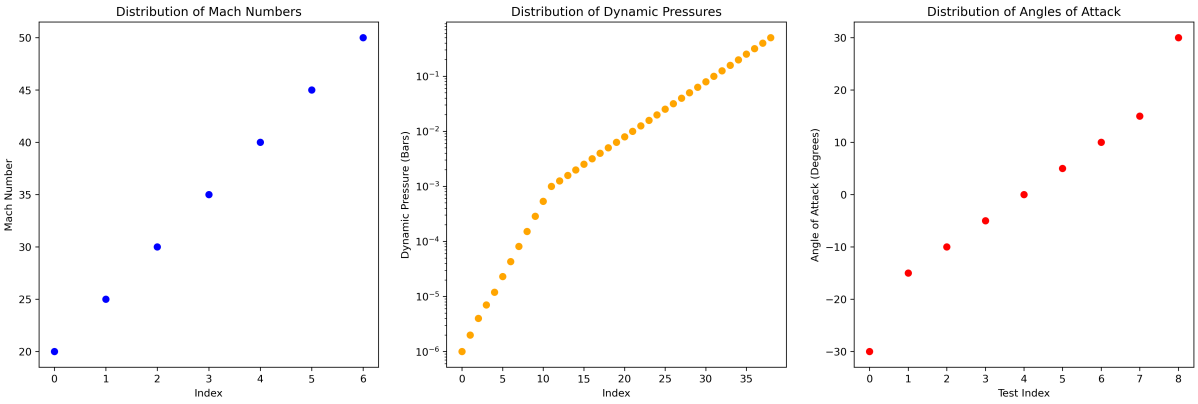

Figure 5.4: CBAERO simulation distributions of Mach number, dynamic pressure, and AoA

After the simulation is completely set up, the command cbaero is used to run the simulation in the Linux command line. For all simulations, the command -nofree is used to remove FMF assumptions and keep the solution strictly laminar. The command -2d is used on all waverider variants for better heating estimates as the stagnation point will not be assumed as a single radial point which corresponds to a single surface triangle of the mesh. Instead, this command allows for the simulation to account for a two

dimensional constant front face of the vehicle, which is the case for all leading edges of the aeroshell configurations. The constant denoted "front nose section" on the elliptical configuration represents this 2D cylindrical leading edge; while it is much shorter than the rectangular nose configurations, it still is constant for a length of 0.25m and requires the -2d callout find the best estimate for surface heating. The command -omp is used followed by a number to allocate multiple cores within the central processing unit of the computer running the simulation. Using all such commands followed by the name of the meshed file without a file extension runs the simulation. The software will viscously iterate throughout all defined Mach numbers, dynamic pressures, and AoA until solutions are found for each combination of parameters. This process will create an complete aerodatabase (ADB) for the different waverider configurations. After the ADB finishes compiling, the command cbviewer can be used in the terminal to enable a variety of plots to be visualized on the skin of the aeroshell OML. Many aerothermal performance parameters including streamlines, wall states, edge states, and surface heating can be visualized as a contour map along the waverider configurations.

Fellow graduate student Anton Kulinich replicated a sample AGA trajectory maneuver through Earth's atmosphere in Genesis Flight Mechanics Simulation and Trajectory software [44], seen plotted below in Fig. 5.5.

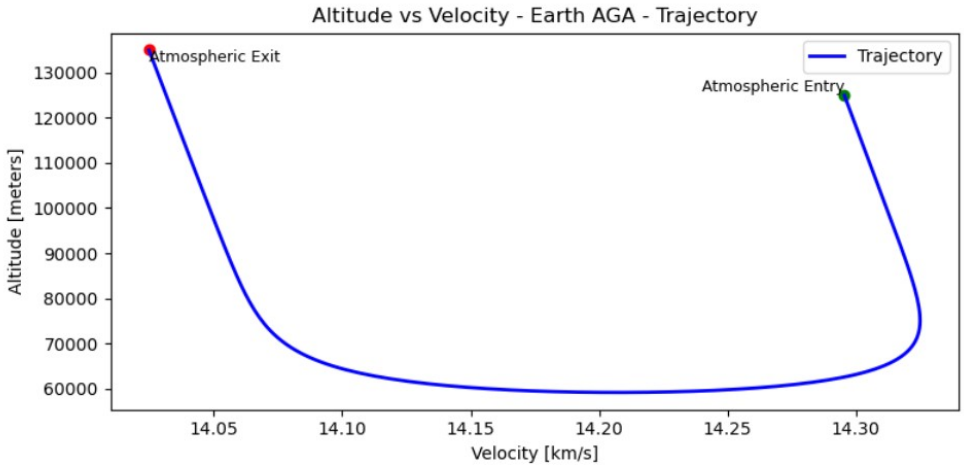

Figure 5.5: Reference AGA flight trajectory

Note that this sample Earth AGA trajectory profile is preliminary and was crafted around optimization of transit time reduction to distant TNOs without regard for the aerothermal environment experienced by the waverider aeroshell. It provides a baseline to understand the AGA flight environment. Traditionally the design of the trajectory should be crafted from the aerothermal performance of the vehicle in the relevant flight environment, with close consideration of mission and system requirements. Four case study locations are selected, with three occurring in the continuum flow regime from the sample trajectory and one in the rarefied flow.

5.3 Results

The results are presented for selected locations along the reference trajectory and are the focal point of the discussion section. These cases were selected to show snapshots

of performance throughout different flight altitudes and velocities along the reference trajectory for the various aeroshell configurations. The first case is selected at 110 km to demonstrate estimates of early atmospheric flight conditions as the waverider dives towards Earth during the AGA maneuver. As this case occurs in the FMF regime, a DSMC simulation tool would be needed to verify and validate the results. The other three cases represent flight conditions in the continuum flow regime. These cases can be validated with CFD, as the Knudsen number is below 0.003 for configurations with $R_n = 0.15$m. The three continuum cases are selected to show entry and exit flight conditions in this flow regime, and the lowest altitude along the AGA trajectory. Tables 5.1 and 5.2 show close correlations between the selected altitudes and velocities along the actual trajectory and the comparative values generated in the ADB for various waverider configuration performance.

Table 5.1: Flight conditions along the AGA reference trajectory

Case Number	**Altitude**	**Time**	**Velocity**	**Mach**	**Dynamic pressure**
1	110.39 km	10 s	14305.08 m/s	46.85	0.0001213 bars
2	63.55 km	60 s	14302.86 m/s	46.32	0.2015 bars
3	59.15 km	86 s	14205.07 m/s	44.88	0.34707 bars
4	67.34 km	120 s	14085.73 m/s	46.65	0.11805 bars

Table 5.2: Correlating conditions in ADB

Case Number	**Mach**	**Dynamic pressure**
1	45	0.0001520 bars
2	45	0.1991240 bars
3	45	0.315534 bars
4	45	0.125661 bars

5.3.1 Aerodynamic Performance

In this conceptual level analysis, all results showed that the elliptical nosed aeroshell provided more performance benefits to the waverider than the variety of trim configurations for the square nosed aeroshell. Aerodynamic performance worsened for all configurations as the blunt nose radius was increased. The elliptical nose configuration had highest trend for L/D with peak values found to be over 1.5 at an AoA of 15° in the continuum region of atmospheric flight. In the early atmosphere, L/D performance for the elliptical configuration was found reaching a maximum of one, depicted in Fig. 5.6. The C_p on the nose of all vehicles was found to range between 1.9 and 1.95 across the entire ADB. The contour map of C_p is displayed for the second case at 63.55 km for the $R_n = 0.1$m elliptical aeroshell configuration in Fig. 5.7. The computed streamlines can be seen in red on the half span geometry as the complete solution is reflected across the y-axis of the aeroshell for each configuration at varying AoA. The C_p contour map of the rectangular configuration is visualized next for case 3 conditions in Fig 5.8 at zero AoA. This figure is followed by a close up view of the streamlines plotted on the C_p contour map for the $R_n = 0.1$m strake model case 2 conditions in Fig. 5.9. The contour map of wall pressure on the $R_n = 0.1$m wedgerider configuration is visualized in Fig. 5.10

for case 2 at 5° AoA. Like the found C_p values, wall pressure profile distributions closely matched in magnitude for all waverider configurations at each selected case along the reference trajectory.

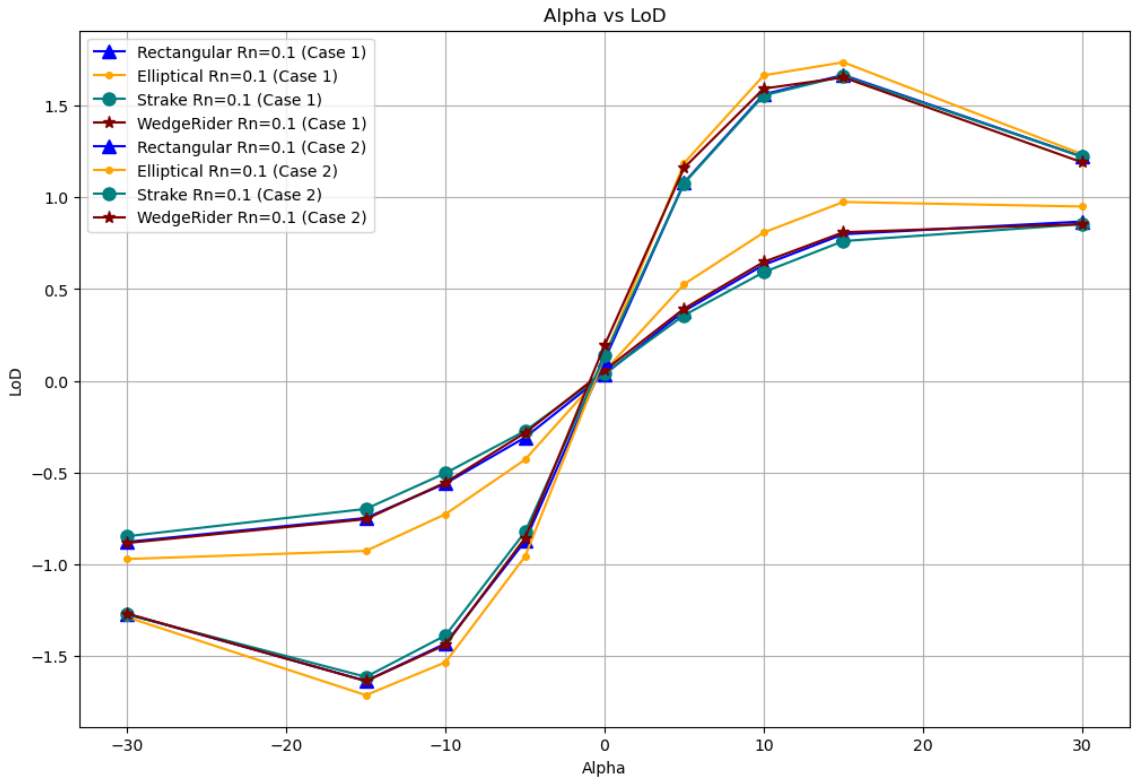

Figure 5.6: L/D v AoA for case 1 and case 2

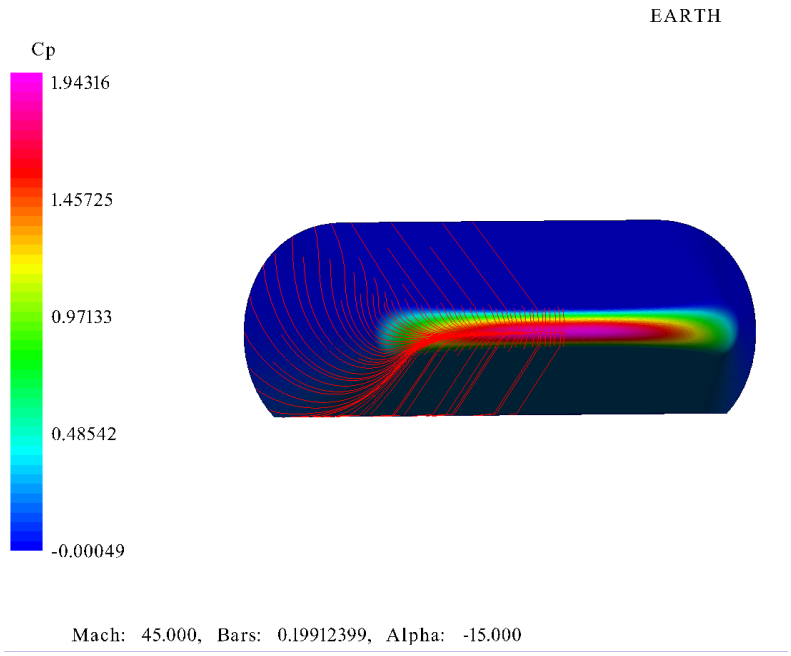

Figure 5.7: Case 2 contour map of C_p on $R_n = 0.1$m elliptical aeroshell at $-15°$ AoA

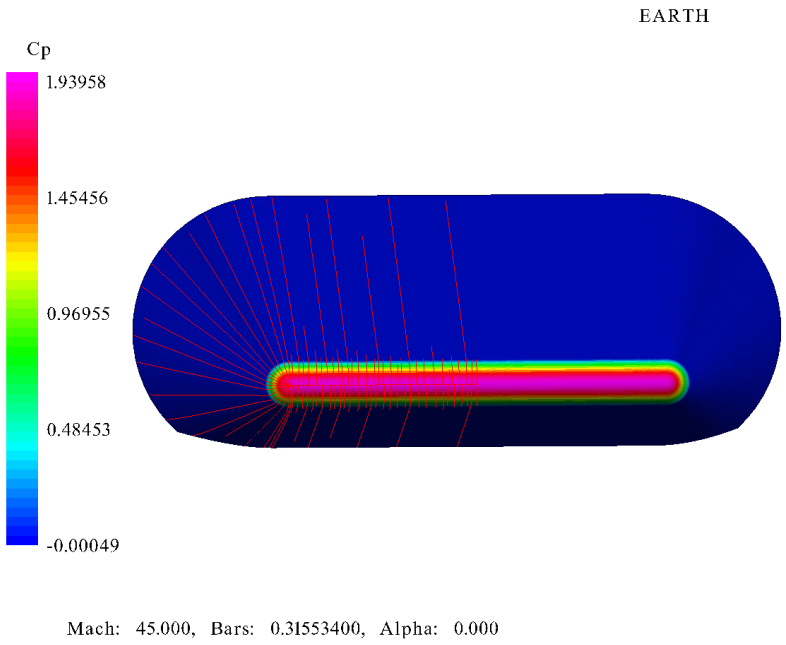

Figure 5.8: Case 3 contour map of with streamlines and C_p on the $R_n = 0.1$m rectangular aeroshell at 0° AoA

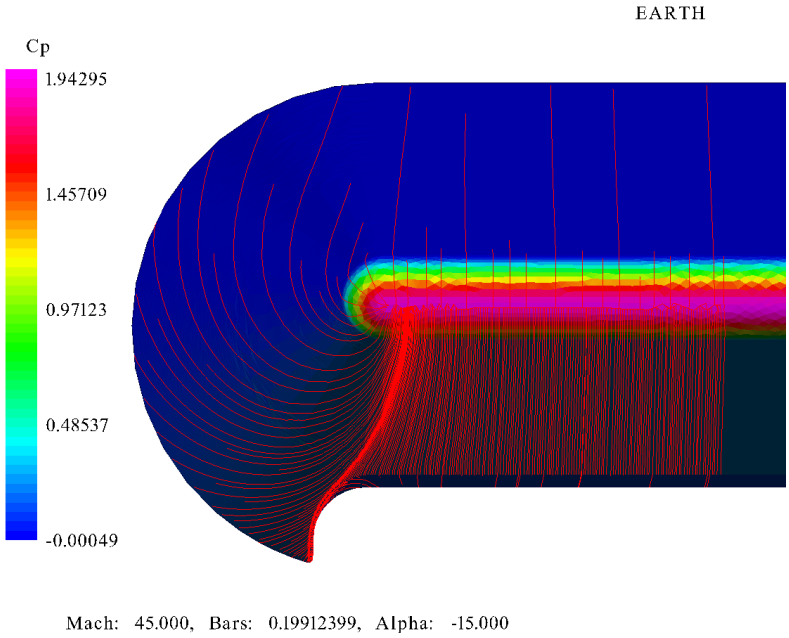

Figure 5.9: Case 2 close up view of contour map with streamlines and C_p on the $R_n = 0.1$m strake aeroshell at $-15°$ AoA

All waverider configurations with smaller blunted leading edges had higher heating rates and better aerodynamic performance due to lower CD values. Increasing the nose radii on the vehicle increased the drag, but lessened the heat load experienced as expected. Minimal variance was seen in the coefficient of lift across all waverider configurations at all altitudes, while drag experienced noticeable changes for different configurations while at different altitudes. The variation in drag is what ultimately affects the L/D performance across the different configurations.

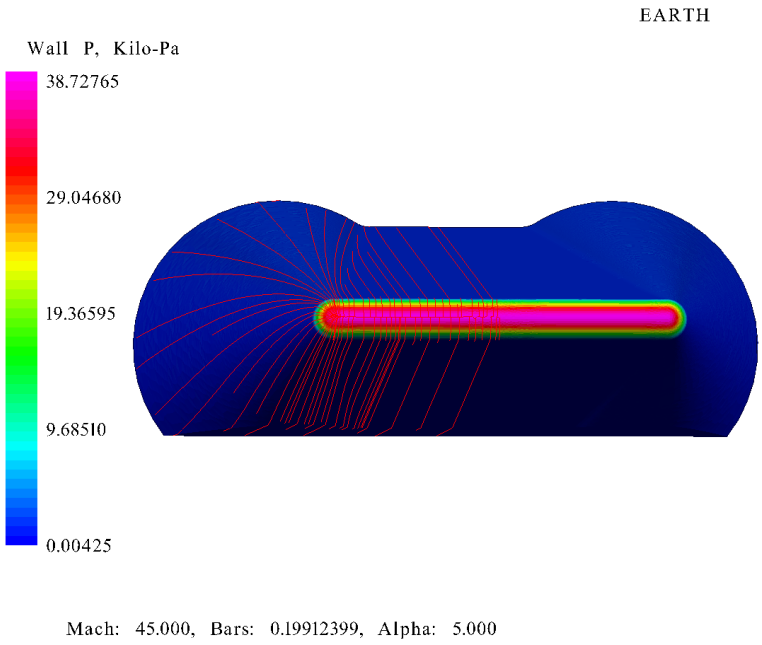

Figure 5.10: Case 2 contour map of wall pressure on the $R_n = 0.1$m wedgerider aeroshell at 5° AoA

Differences in aerodynamic performance of the waveriders are most notable between case 1 at 110 km and the cases in the continuum flow regime. As noted for all waverider configurations across the range of flight altitudes, little variance was seen in the coefficient of lift, as shown in Fig. 5.11.

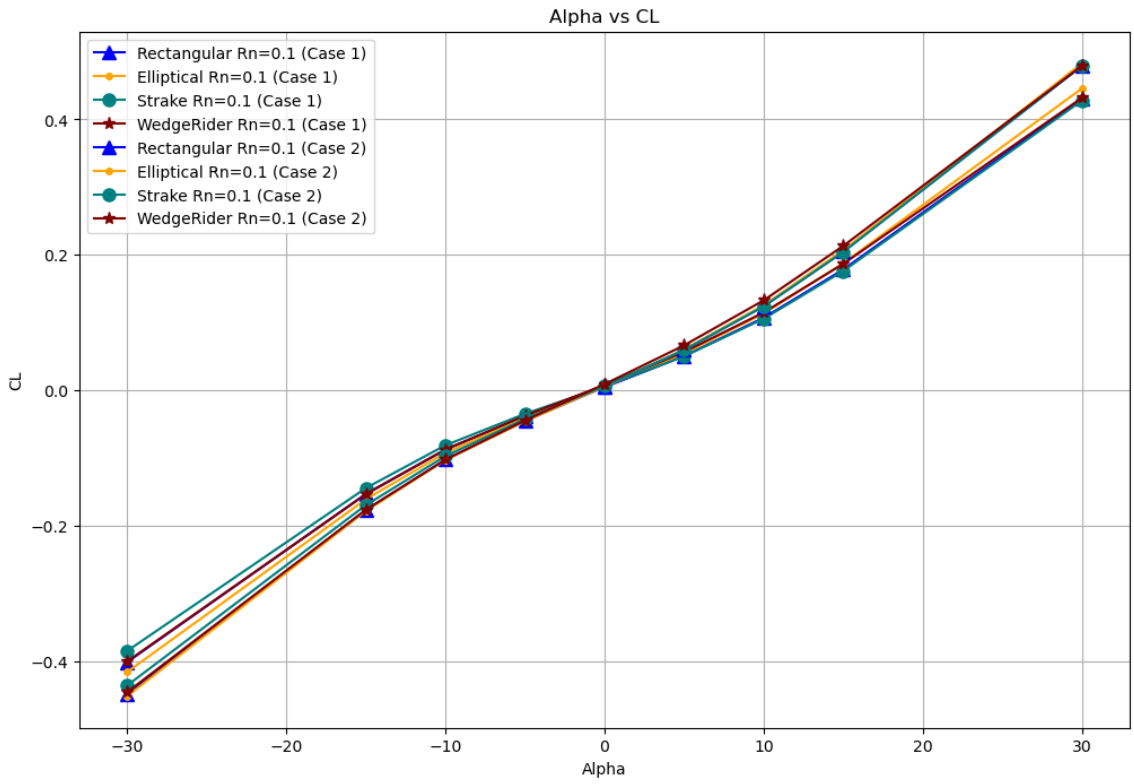

Figure 5.11: C_L v AoA for case 1 and case 2

Drag was more noticeable at different altitudes and across the varying configurations, with the C_D values are higher than in early atmospheric conditions. The elliptical nose configuration is seen to provide less drag when compared to other aeroshells as depicted in Fig. 5.12. Case 1 is see to have the higher distribution of C_D values, while case 2 has nearly identical results for all waverider configurations. The comparison of C_L and C_D between case 1 and case 2 is shown in Fig. 5.13. The aerodynamic performance of all rectangular nose configurations is fairly similar. The wedgerider showed to have slightly higher lift between an AoA of 5° and 15° resulting from the central high pressure region, showing slight improvement over the strake and rectangular on the L/D curve seen in Fig. 5.6.

Controllability of the various waverider configurations is not of interest in this aerothermal analysis, but the pitching moment coefficient is included in the results. The C_m of all configurations ranges from -0.08 to 0.06 across the range of AoA in the ADB for aeroshells with $R_n = 0.1$m. Little variance is seen between flight and altitude conditions in case 1 and case 2. The strake model is seen to have the lowest C_m, with performance of the elliptical model closely following. This relation is seen plotted in Fig. 5.14.

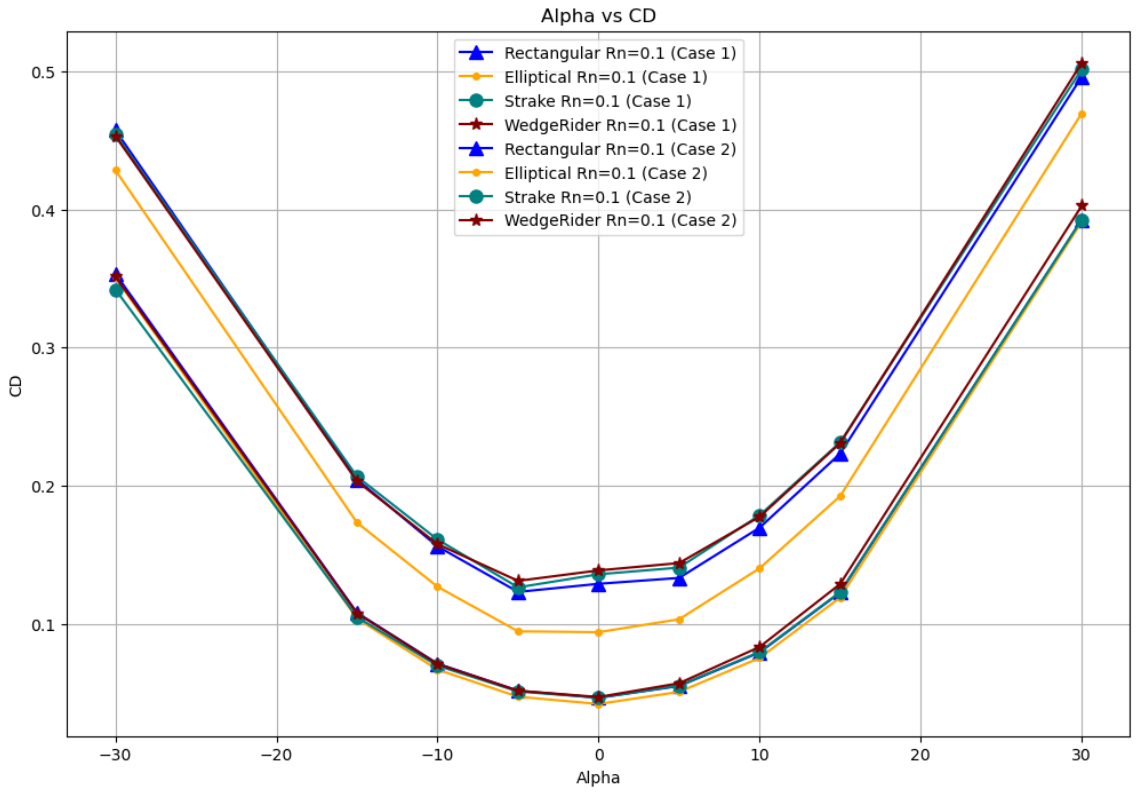

Figure 5.12: C_D v AoA for case 1 and case 2

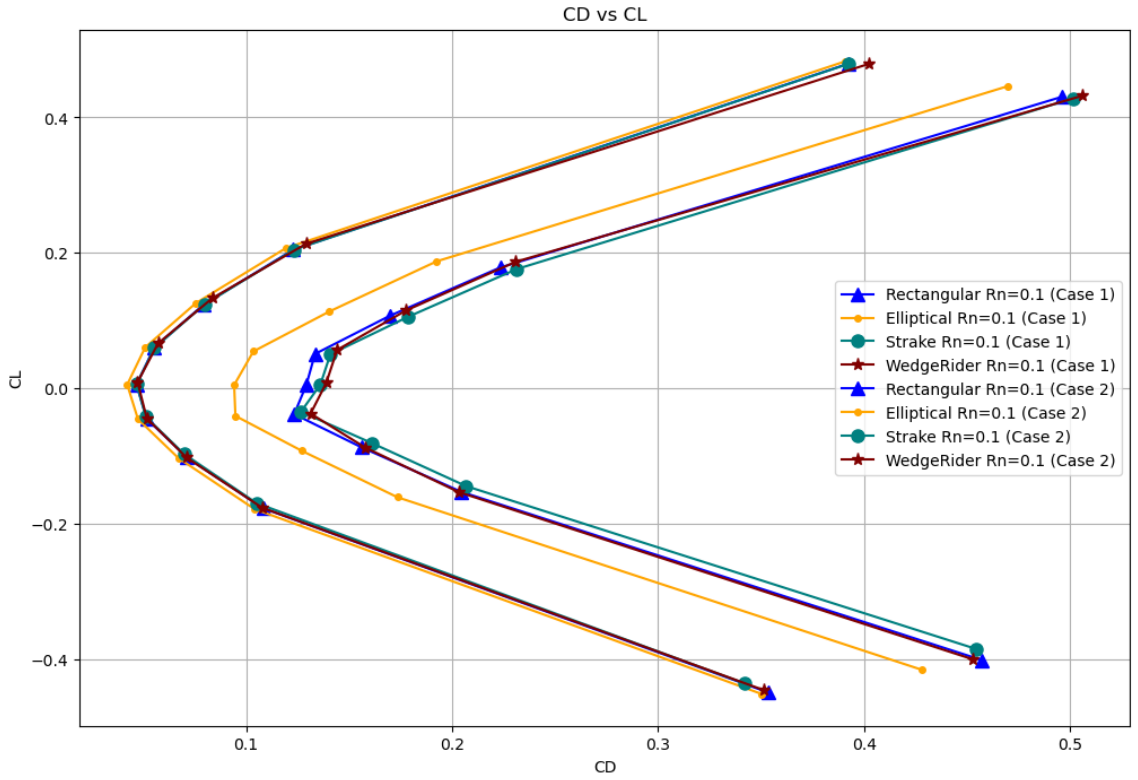

Figure 5.13: C_L v C_D for case 1 and case 2

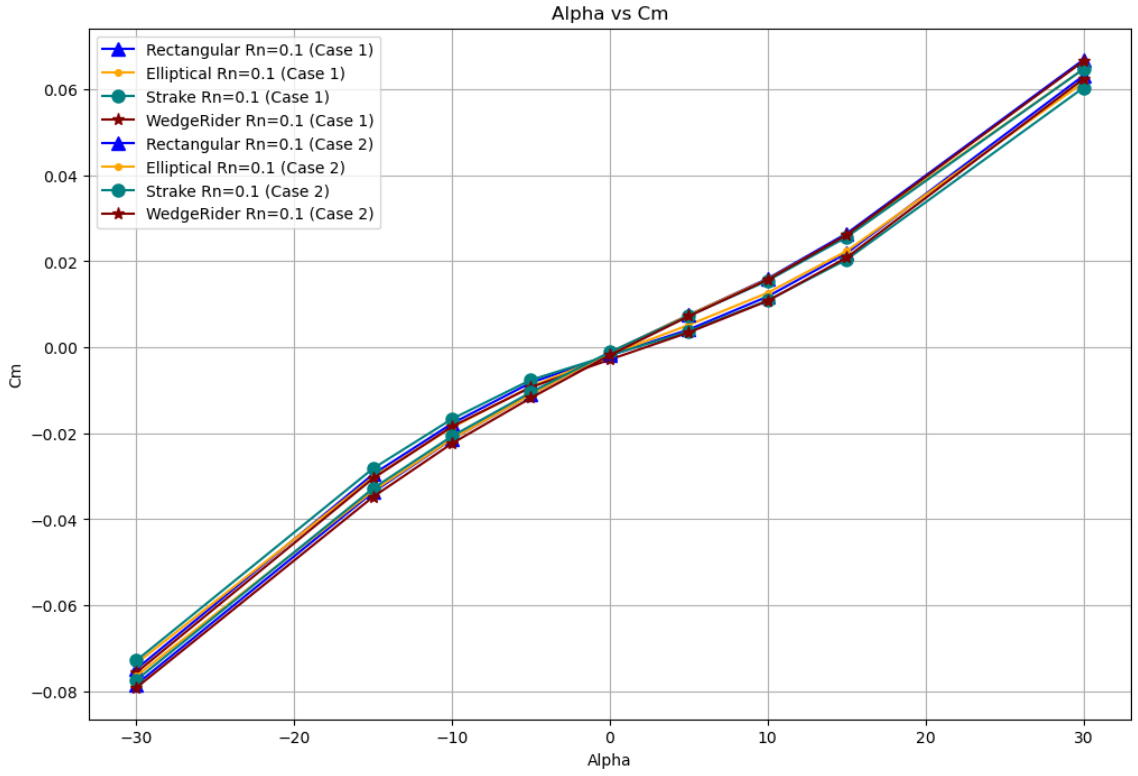

Figure 5.14: C_m v AoA for case 1 and case 2

5.3.2 Thermal Performance

Conceptual estimates of thermal performance showed the elliptical model had the lowest total heating for all waverider configurations. Trends indicated that the elliptical aeroshell configuration experienced slightly higher convective heating rates than the rectangular nose configurations for a given nose bluntness, but the elliptical configuration experienced significantly less radiative heating. Case 3 had the highest stagnation heating along the reference AGA trajectory from flight in the densest region of continuum flow at the lowest altitude. This result is expected, as convective heating will fall off with the square root of density assuming a fixed velocity. Contour plots of total heating rate estimates for the elliptical nose configuration at the extreme bluntness values studied in this report are depicted in Fig. 5.15 and 5.16.

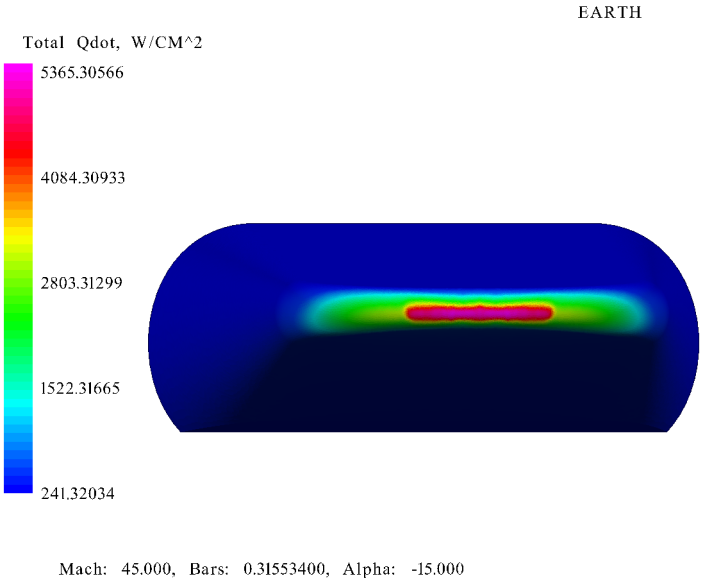

Figure 5.15: Case 3 total heat map for elliptical aeroshell with $R_n = 0.1$m at $-15°$ AoA

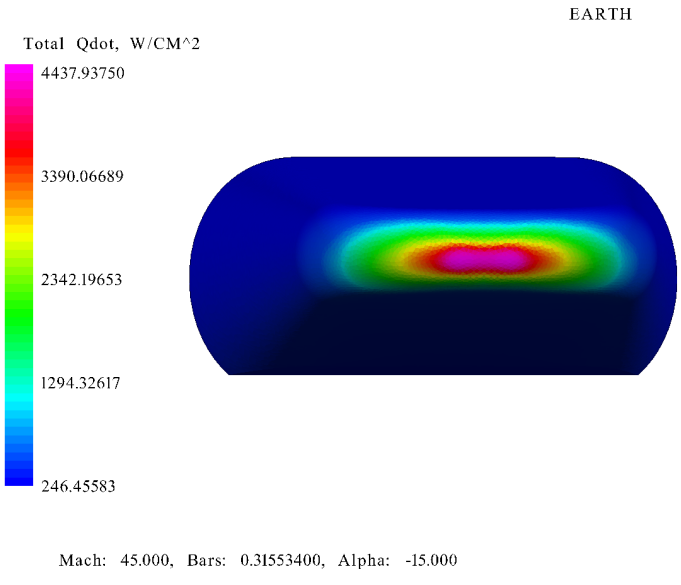

Figure 5.16: Case 3 total heat map for elliptical aeroshell with $R_n = 0.25$m at $-15°$ AoA

A contour plot of total heating on the $R_n = 0.1$m strake model is depicted in 5.17 for case 3. While uncertainties and fluctuations are present in the heating estimates, the trends indicate that the strake configuration had the second lowest heat rate at $-15°$ AoA. All waverider configurations will be required to maximize aerodynamic performance through the AGA trajectory maneuver and will likely maintain a similar AoA orientation throughout the continuum flow regime. The corresponding wall temperature profile of the strake configuration is shown in 5.18; calculated from the total heat rate as expressed in Equation 5.4. The 10 mm fillet on the tip of the strakes has higher heating rate and wall temperatures than the rest of the vehicle profile besides the nose, as indicated by the light blue-green hue on the contour map.

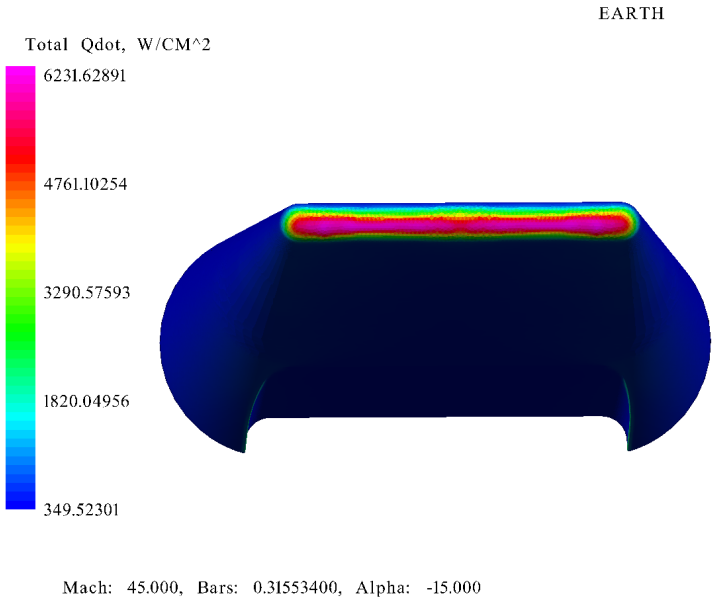

Figure 5.17: Total heating contour map for strake aeroshell with $R_n = 0.1$m at $-15°$ AoA

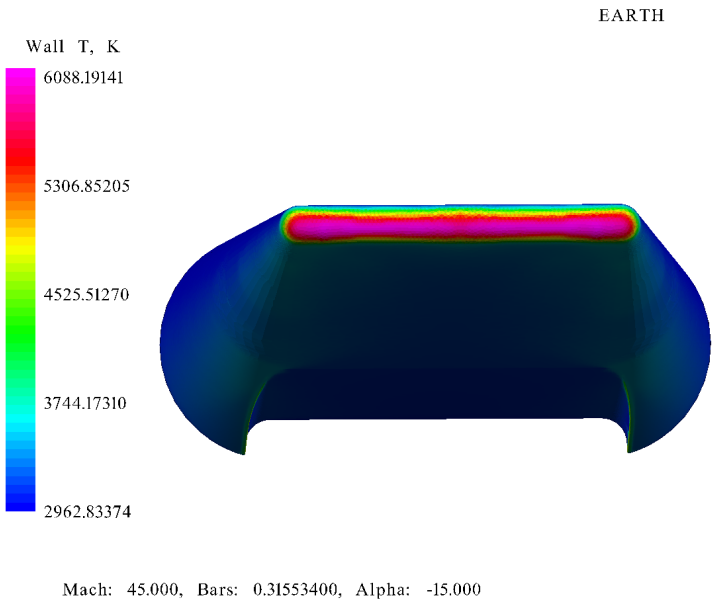

Figure 5.18: Wall temperature map for strake aeroshell with $R_n = 0.1$m at $-15°$ AoA

The heating rate should decrease for all aeroshell configurations as the blunt nose radius increased, inversely proportional to aerodynamic performance. Heating rates in early atmospheric flight was found to be significantly lower, with convective heat rates dominating when compared to flight in the lowest altitude along the trajectory. For case 2 and 4 in the 64-68 km range where the waveriders enter and exit the continuum flow regime, total heat rates for aeroshell configurations with $R_n = 0.1$m ranged from 2500 to 4500 W/cm^2. Radiative heat flux is significant but accounts just less than half the total heat rate. Case 3 at 59.15 km had the highest heat flux values which ranged from 5365 to 6450 W/cm^2 for aeroshell configurations with $R_n = 0.1$m. For this specific case, radiation heating accounted for more than half the heat flux experienced by all waverider configurations with a rectangular nose, and heat fluxes ranged from 6200 to 6450 W/cm^2 at 15° AoA. The elliptical waverider with the same nose bluntness experienced a heat flux value of 5365 W/cm^2 (seen in Fig. 5.15) which is a reduction of more than 850 W/cm^2. Estimates for the convective heating rate displayed all configurations had relatively uniform trends, but radiation heating rates had more fluctuations across the waverider configurations. The fluctuations become noticeable in the continuum region and had bigger oscillations as the magnitude of total heat flux increased.

Plots comparing total heating rate for all selected cases of the four waverider configurations having bluntness values of $R_n = 0.1$m and $R_n = 0.25$m are depicted in Figures 5.19, 5.21, 5.23, and 5.25. Comparing bluntness values of $R_n = 0.1$m and $R_n = 0.25$m show the extreme upper and lower bounds of heating rates across all aeroshell configurations, verifying that heating rate decreases with increasing the waverider leading edge nose radii. The large oscillations in total heating values seen in Fig. 5.21, 5.23, and 5.25 are primarily due to estimates of radiative heating rates. Fluctuations in the radiative heat rate are seen to be most extreme case 3, where variations exceed 500 W/cm^2. Results show radiation heating becomes critically relevant for flight in the continuum regime as seen in case 2 and 4, accounting for nearly half the total heat rate on the aeroshell for square nosed waverider configurations. Case 3 results see the radiation heat rate higher than convective except for the elliptical aeroshell, as convective heat flux remains larger than radiative. Estimates of the radiative heat rate for the $R_n = 0.1$m elliptical aeroshell is much lower than all other vehicles with the same nose radii and performs the best out of all the configurations.

Figures 5.20, 5.22, 5.24, and 5.26 are included to show convective heating rates, which is the dominate heat transfer mode until the continuum flight regime. While oscillatory behavior exists in the convective heating results, these fluctuations do not exceed 200 W/cm^2 over the range of AoA. Trends displayed that convective heating increases with higher AoA values for the elliptical configuration while the inverse tended to occur for rectangular nose configurations. Apparent reasons for these trends in the results are discussed in the next chapter.

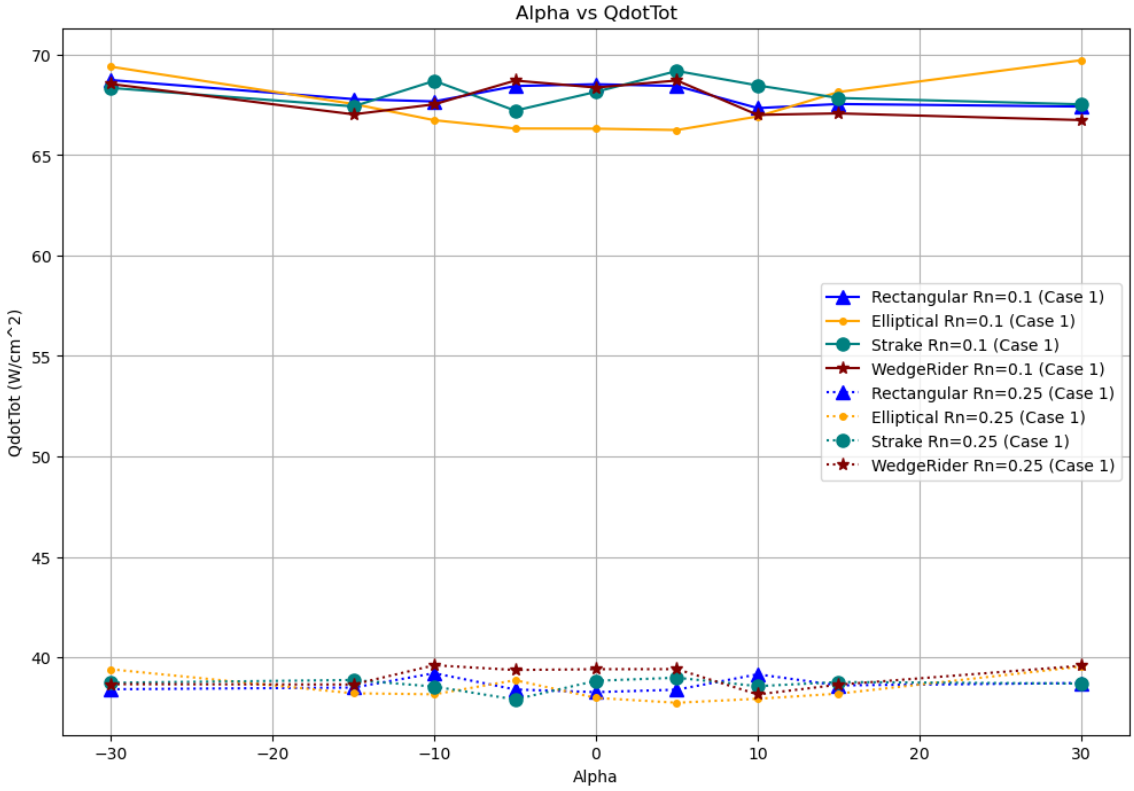

Figure 5.19: Case 1 total heating for waveriders with nose bluntness $R_n = 0.1$ and $R_n = 0.25$

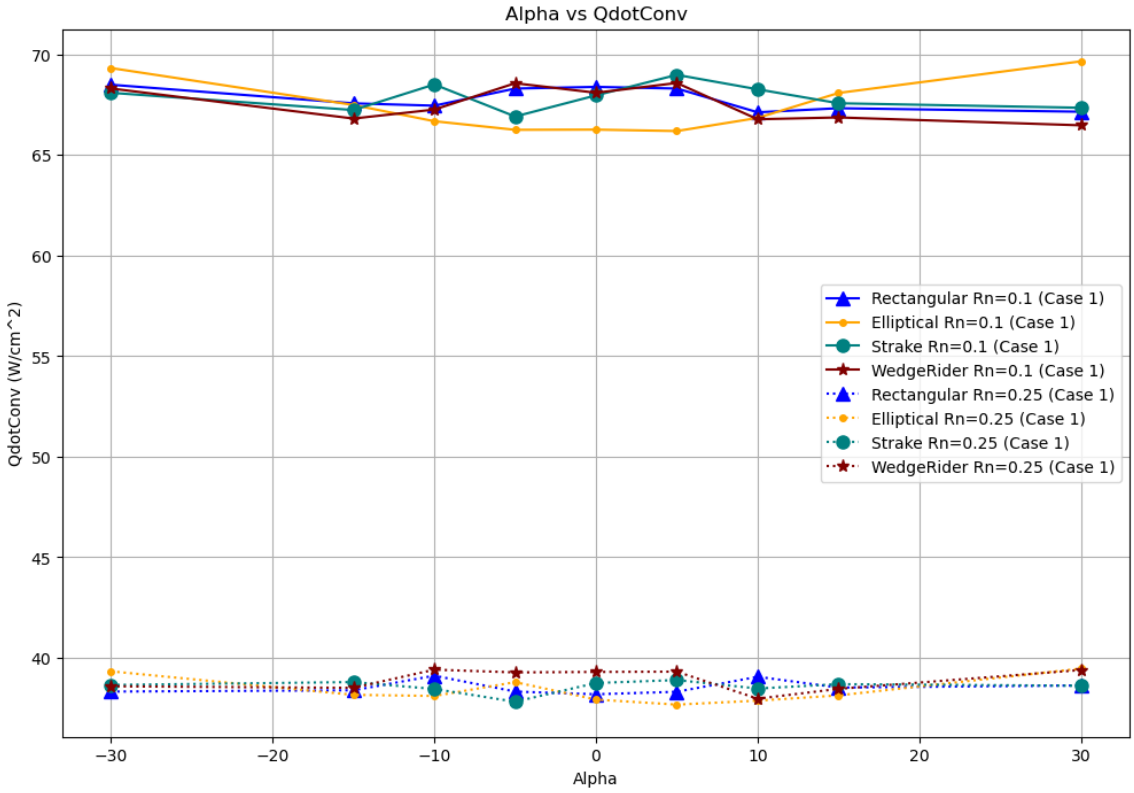

Figure 5.20: Case 1 convective heating

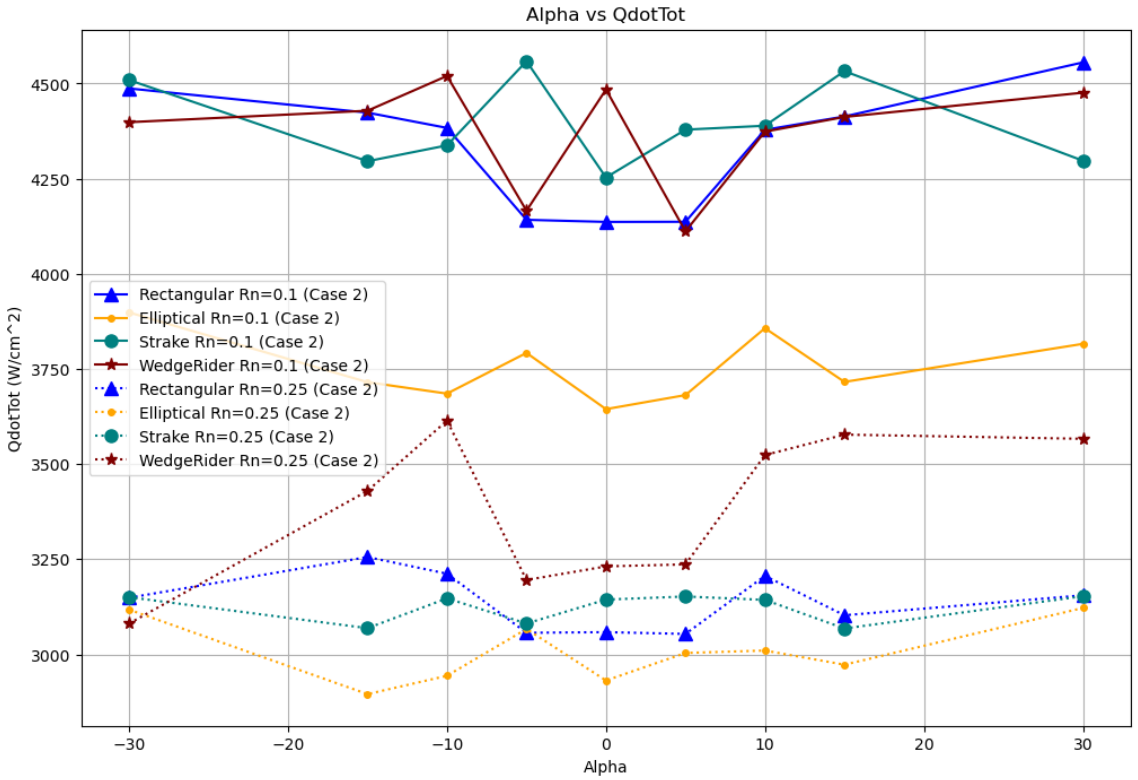

Figure 5.21: Case 2 total heating for waveriders with nose bluntness $R_n = 0.1$ and $R_n = 0.25$

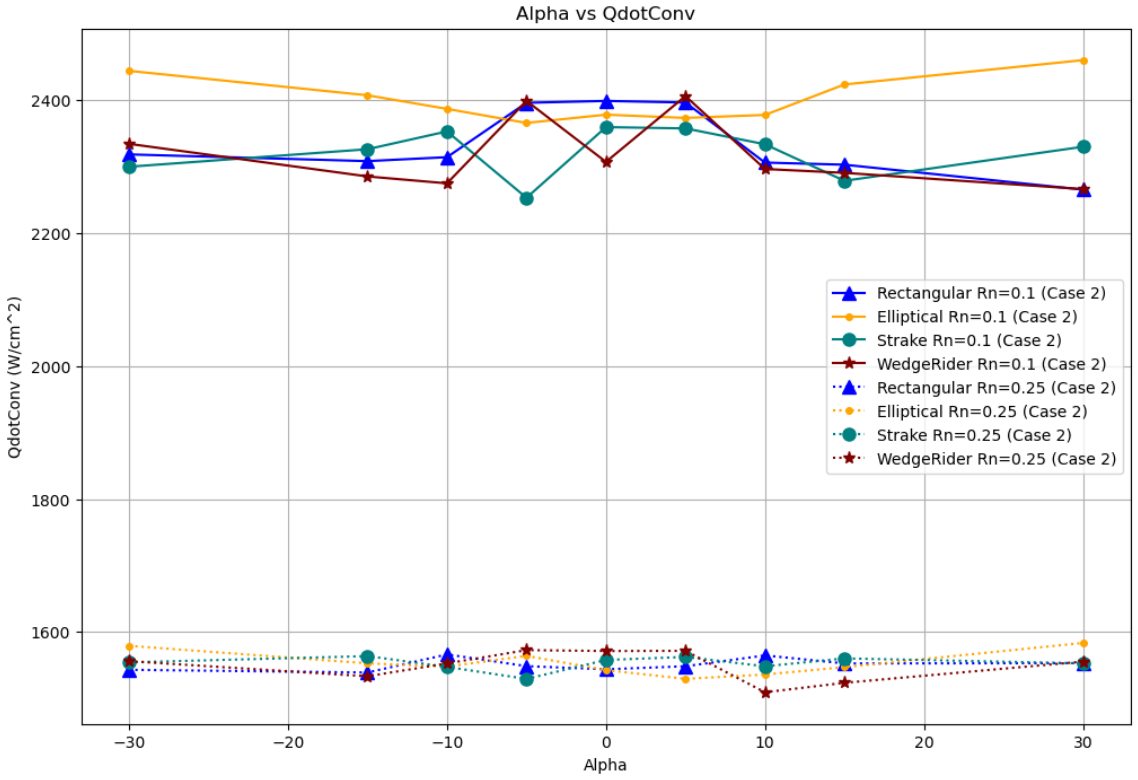

Figure 5.22: Case 2 convective heating

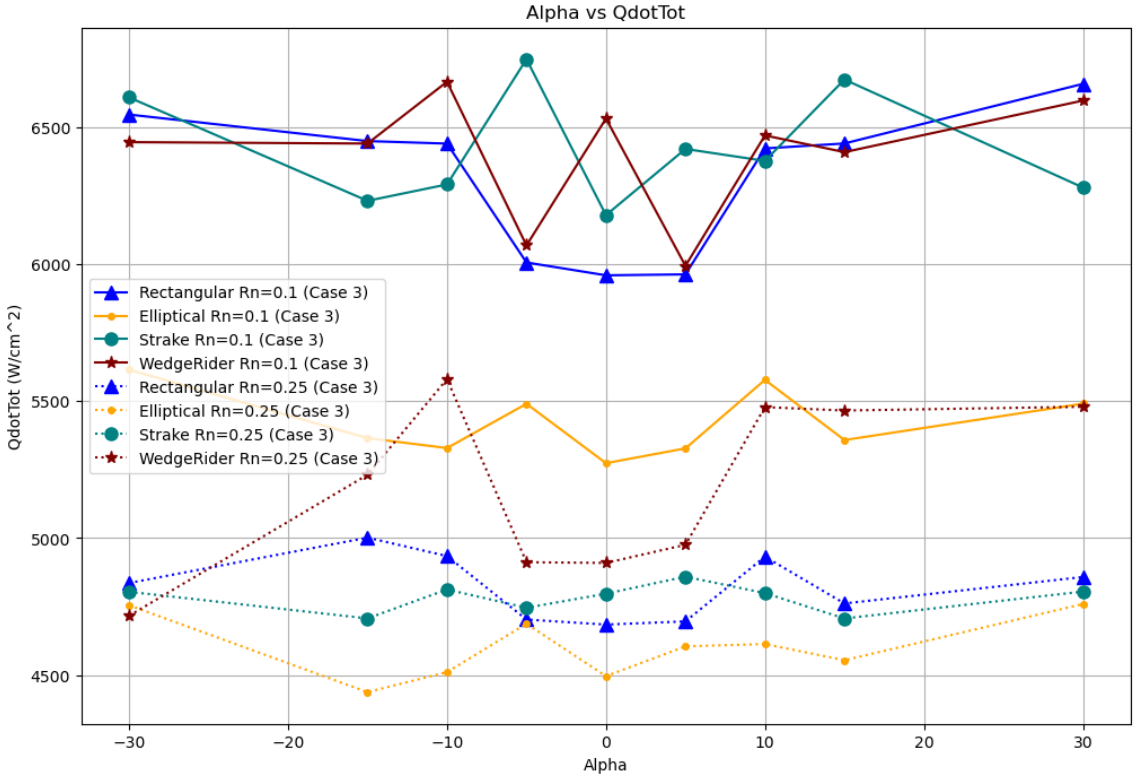

Figure 5.23: Case 3 total heating for waveriders with nose bluntness $R_n = 0.1$ and $R_n = 0.25$

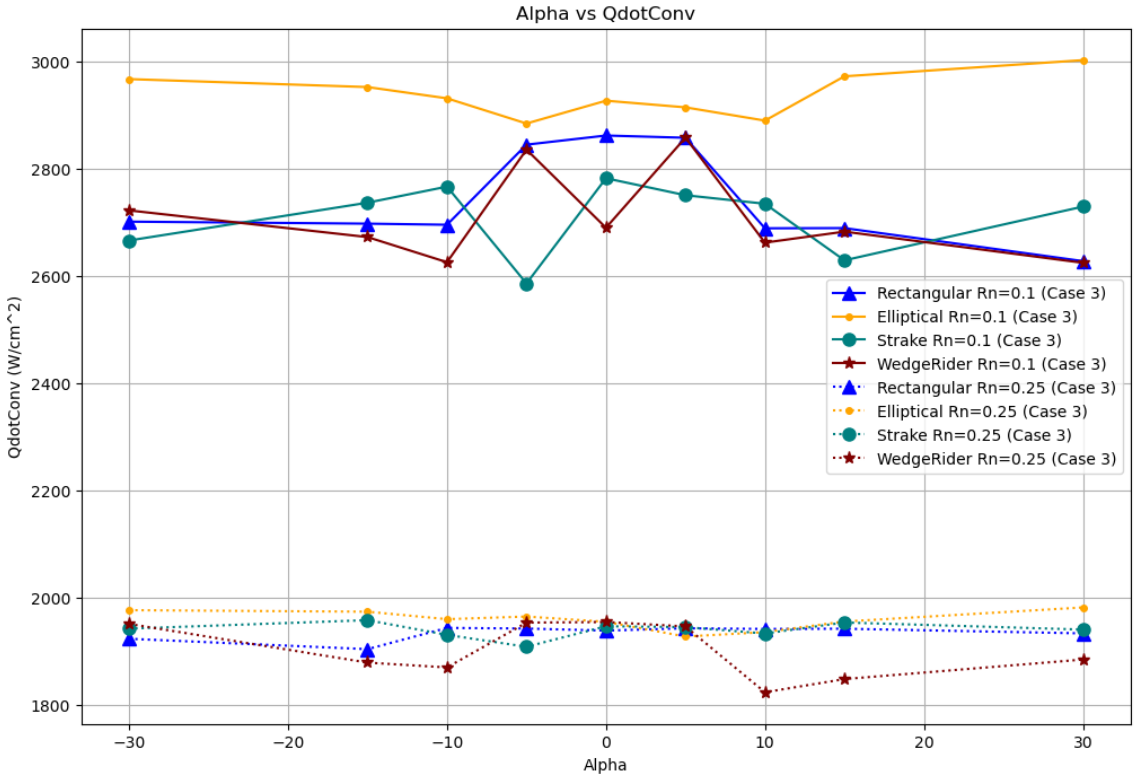

Figure 5.24: Case 3 convective heating

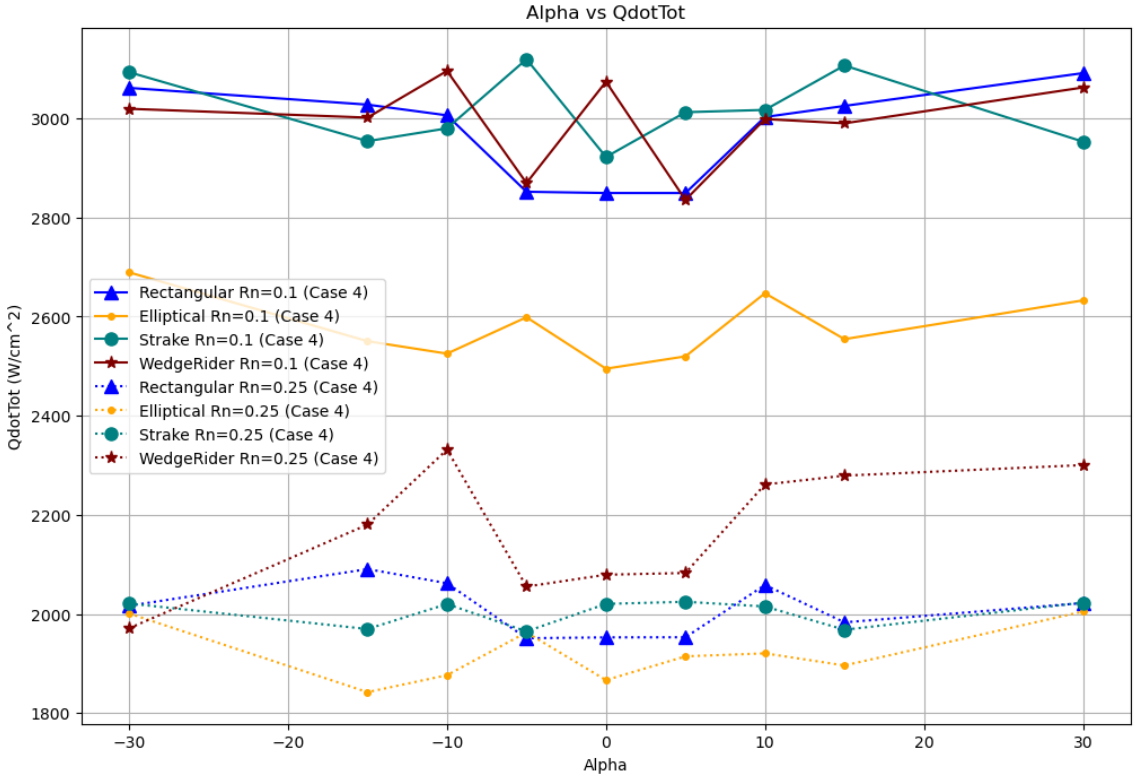

Figure 5.25: Case 4 total heating for waveriders with nose bluntness $R_n = 0.1$ and $R_n = 0.25$

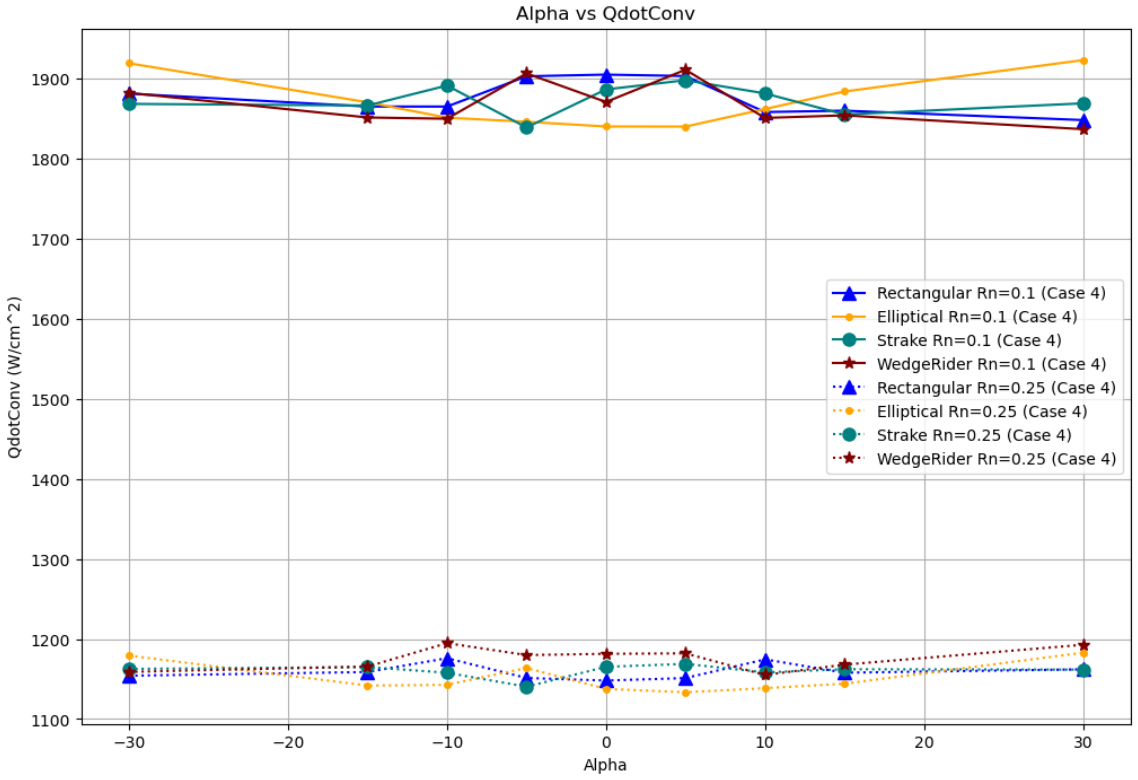

Figure 5.26: Case 4 convective heating

Chapter 6:

Discussion

6.1 Major Findings and Comparisons

6.1.1 Aerodynamic Performance

Results from the aeroshell configurations showed the elliptical nose vehicle had the best L/D performance and overall thermal performance of the four waverider configurations along the reference AGA trajectory. Expected by Tauber's relations, overall heating and stagnation point temperature values all decreased as the bluntness of the vehicle nose increased. As the nose bluntness of the waveriders increased, the aerodynamic performance was impacted due to higher drag values, which was another expected result.

The Modified Newtonian formulation was used for all simulation results in this report. Newtonian impact theory is consistently used by industry experts for the continuum flow regime, confirmed by Prabhu in personal communications. This formulation should provide closely accurate pressure solutions for the aerodynamics and stagnation point estimations, thus predictions of hypersonic aerodynamic performance are assumed to be closely realistic. The streamline traces showed flow symmetry on the waverider configurations at zero AoA. The C_p results of the Modified Newtonian formulation were bench marked for generic sphere and cylinder cases at Mach 30 with professional collaboration from Saunders and Prabhu at NASA Ames, finding close agreement in C_p values between CBAERO and HyperCFD. Additionally, a CBAERO benchmark case was ran on the SHARP-L1 model with different aerodynamic solvers for a variety of nose bluntness values across a small range of AoA. While this study is not discussed in this report, it was completed for professional work with AMA to verify and validate the engineering tools used for analysis. While this internal study used slightly different flight conditions and the aerodynamic formulation method of Tangent cone real gas versus Newtonian for the benchmark case, the L/D curve for R_n = 1mm closely matched the one found in literature [29], as seen in Fig. 6.1.

Kolodziej's conference proceedings on the SHARP-L1 demonstrator also displayed the aerodynamic performance of lift and drag coefficients. Another verification case looking at C_L vs C_D is presented in 6.2, done for research professionally with AMA. While the difference in the blunted nose radii is quite significant when compared to the smallest R_n of 100 mm in this report, a variety of nose bluntness values are seen over a smaller AoA range from 0° to 20°. The plot used to benchmark performance provided in literature by Kolodziej was generated from high fidelity CFD code ran at Mach 16, with a comparison between the UPS CFD code and the hypersonic CFD code GASP [29]. While hypersonic flight conditions are not identical, aerodynamic results seen by Kolodziej in Fig. 6.2 show similar agreement to trends and values found for flight in the continuum flow regime in Fig. 5.12. The AoA range is from 0° to 25° in Kolodziej's study, versus −30° to 30° in the ADB's generated for this report.

Drag values for waverider configurations in this report are observed to be higher than findings by Kolodziej, but this result is expected as drag will increase with nose bluntness. Wave drag will dominate at hypersonic speeds when compared to skin friction,

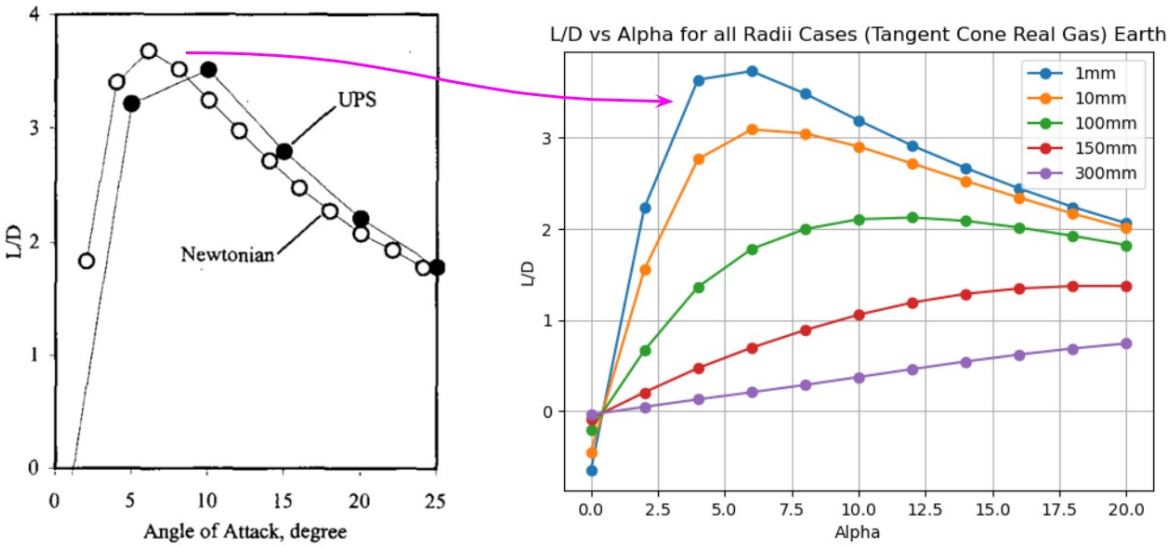

Figure 6.1: L/D comparison between literature [29] and SHARP-L1 rectangular nose models with increasing nose bluntness

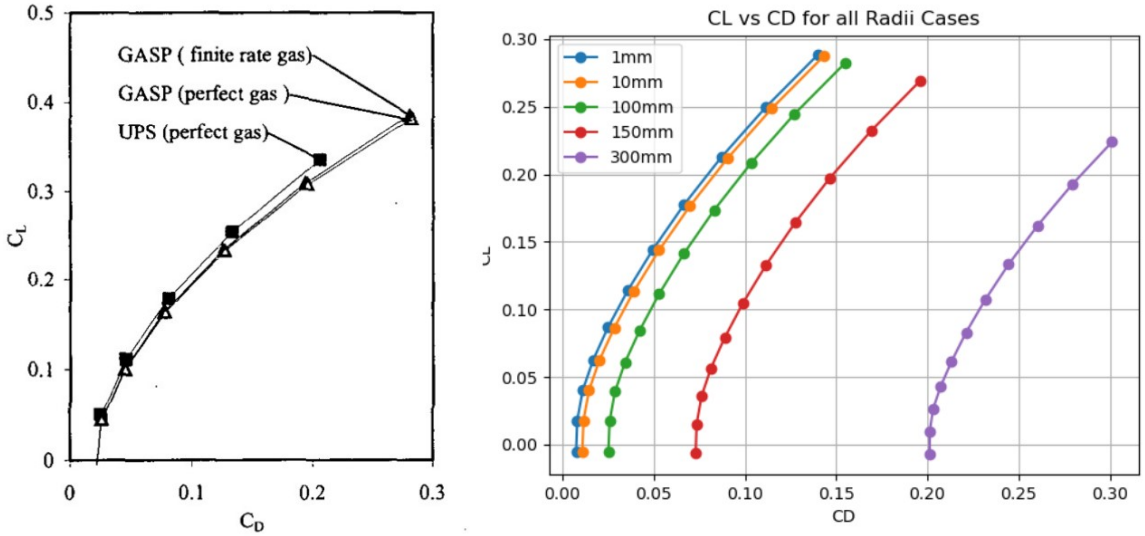

Figure 6.2: 1 mm SHARP-L1 aerodynamic performance [29] compared to blunted rectangular nose aeroshell

and more wave drag occurs with a blunter nose showing consistency with results. To provide a closer benchmark case, the flight conditions and AoA range should explicitly match the case denoted in literature. Case 3 is displayed in Fig. 6.3 with all waverider configurations CD values at upper and lower bounds for nose bluntness value. For flight in the continuum flow regime, drag losses were observed to be linear with increasing bluntness. Drag estimates found for case 1 in the FMF regime are seen to be higher, which is an expected result. Newtonian results should be higher in the rarefied regime, as Hotshot-type wind tunnel testing determined the drag coefficient of a sphere transitioning from continuum to FMF should increase drastically from 0.9 to 2 depending on free stream Knudsen number [45]. This result was observed in case 1 C_D distribution for all waverider configurations as shown in Fig. 5.12. This result was more apparent in the rectangular

nose configurations, increasing the C_D by 0.1 compared to 0.05 increase for the elliptical configuration.

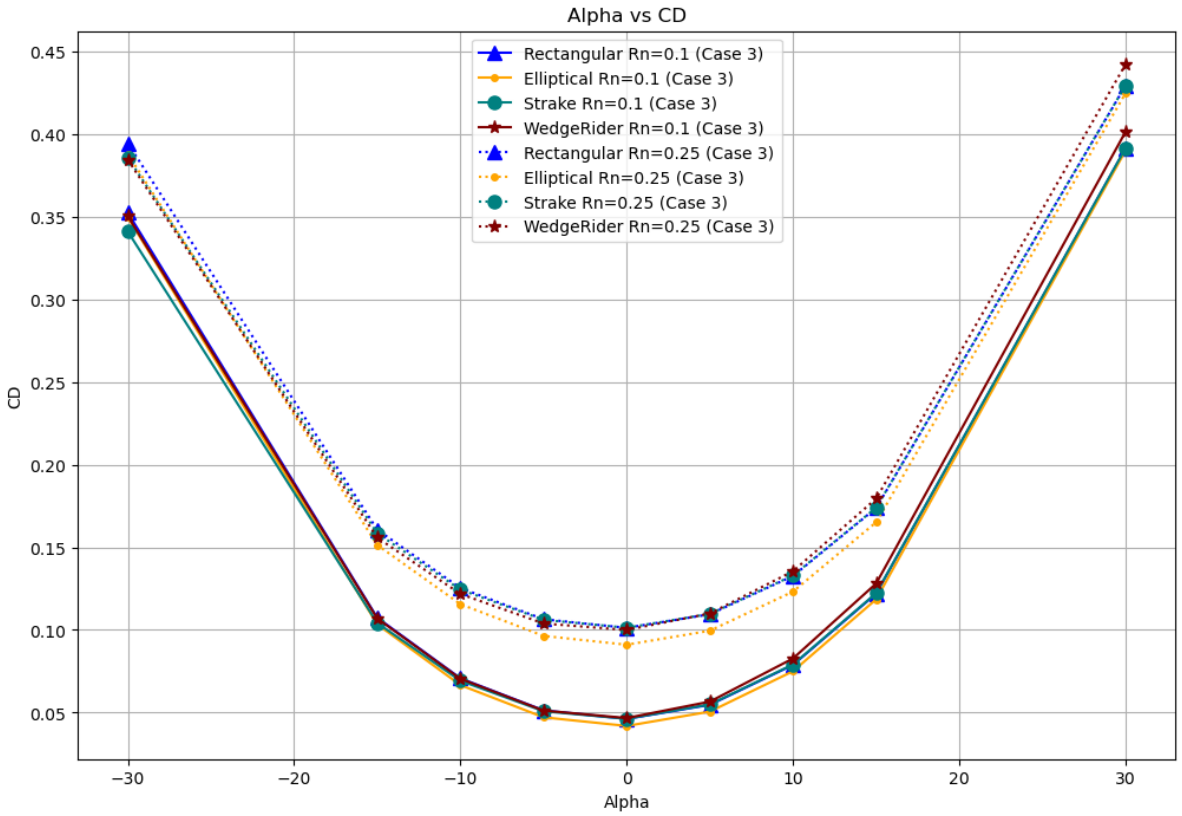

Figure 6.3: Case 3 C_D profile for all configurations upper and lower nose bluntness bounds

The coefficient of lift plotted determined by Kolodziej finds close agreement as maximum values are slightly just below 0.4 [29], which similarly occurs at 25° as seen in Fig. 6.2. The high pressure surface of the wedgerider slightly increased C_L which influenced L/D for certain positive AoA values. However, this waverider had the largest reference and surface area for all configurations, which leads to higher drag forces. All results found for C_L across the waverider configurations with varying nose bluntness throughout the trajectory flight conditions were found to be slightly above 0.4 at an AoA of 30°, showing agreement to what should be expected for a wedge-cone waverider aeroshell derivative.

6.1.2 Thermal Performance

Sharp leading edges in hypersonic flow lead to extreme heating, and the convective heating rate falls off by $1/R_n^{1/2}$ as the radius of curvature increases on the leading edge of the waverider. This trend is clearly apparent across all aeroshell configurations as the R_n increases, and results from thicker boundary layer development reducing the convective heat transfer coefficient and delayed flow separation. Convective heating on the corner of the rectangular nose configurations should be higher, as the hypersonic flow is turning over a small radius. Convective heating concentrations are observed to be higher on the contour plots of the square nose configurations, being more pronounced on the $R_n = 0.1$m configuration seen in Fig. 6.4

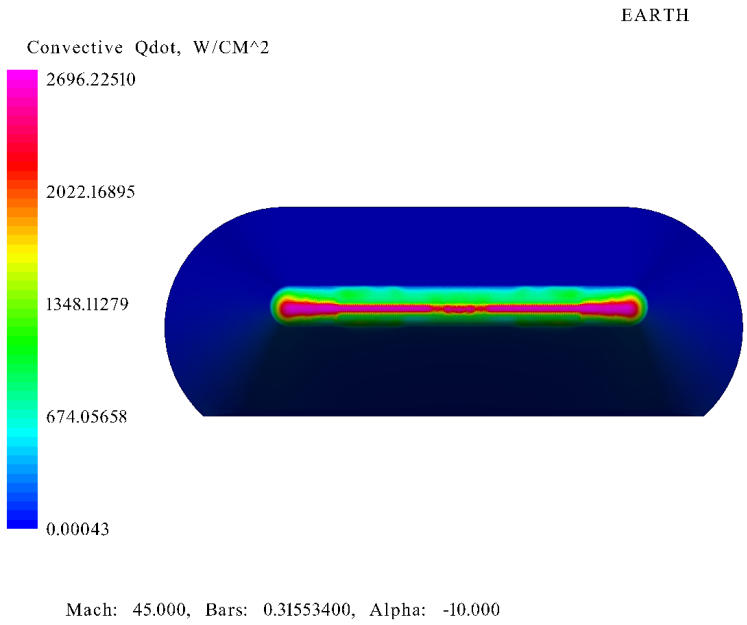

Figure 6.4: Case 3 convective heat map for rectangular aeroshell with $R_n = 0.1$m at $-10°$ AoA showing heating concentration

Radiation heating generally increases with radius of curvature and is worse for bigger vehicles due to the volumetric subsonic bubble on the leading edge of the vehicle. Radiation heating rates are seen to be smallest with elliptical nose vehicle, which is in agreement to theoretical expectations. With the rectangular and elliptical waverider configurations having the same leading edge radius, the curved leading edge seen in the elliptical model should result ins smaller radiation heating values. The elliptical nose turns away from the stagnation region faster, thus a smaller subsonic gas bubble is expected on the leading edge of this configuration. The smallest nose radii elliptical vehicle had the least amount of radiative heating, which is opposite to the findings for convective heating. Contour plots of radiative heating reflected expected thermal flux distribution on the nose of the aeroshell, as seen for the elliptical configuration in Fig. 6.5.

Even with the fluctuations in results, trends still displayed evidence that convective heat flux increases with higher AoA values for the elliptical configuration while the rectangular nose configurations had convective heat flux increase at zero AoA. For the elliptical configuration, the flow sees a much blunter shape at zero AoA, driving convective values lower. This observation is the opposite for rectangular nose configurations, as the flow sees blunter shape at high AoA. Rectangular configuration convective heat flux values are seen higher near zero AoA for all rectangular configurations, while radiative heating is generally observed to fall off at zero AoA. This result makes sense, as the rectangular configuration sees a blunter face at higher AoA thus has larger radiative heating. Radiative heating values will drop off rapidly, but convective heating remains apparent.

In discussion with Prabhu, radiative heating estimates from CBAERO seemed high given the flight conditions. Radiative heating will be critically relevant, as velocities of 14 km/s are well above the 11 km/s level where the fraction of heating due to radiation will increase sharply. If one were to initially disregard radiative heat flux, convective heat flux is seen to range between 2600 and 3000 W/cm^2 for all configurations in the stagnation

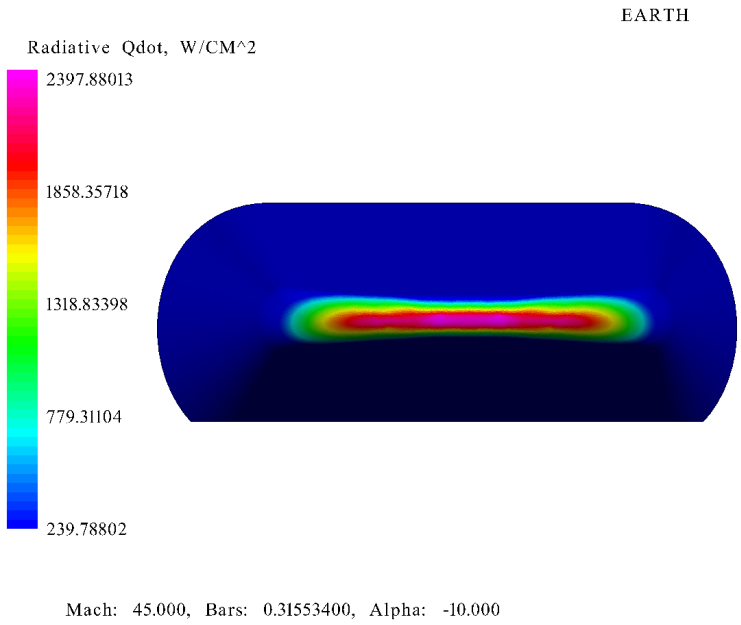

Figure 6.5: Case 3 radiative heat flux map for elliptical aeroshell with $R_n = 0.1$m at $-10°$ AoA

region at the leading edge of the aeroshell. To fight heating, a high density material would be required on the leading edge, moving the vehicle CG forward. A heavier vehicle nose would improve stability, but this can lead to further complications for materials and aeroshell controllability issues.

Heat rates up to 3 kW/cm^2 are not a problem for the state of the art woven TPS known as Heatshield for Extreme Entry Environments Technology (HEEET), developed at NASA Ames Research Center. Woven TPS like HEEET comes in single or dual layers, and can support a broader mission design space for both entry angle and velocity while providing superior robustness at a modest penalty in mass [46]. However, radiative heat flux will also be a significant factor at these velocities. TPS sizing may prove to be challenging but within limits of the current state of the art materials. As the TPS will vary in thickness, Gary Allen expressed that a critical requirement is the bone line temperature of the glue which fastens the material to the aeroshell must stay below 250°C. Manufacturing capabilities present limits on total thickness of woven material [46], but existing technology and the ability to couple other TPS materials or active cooling methods should enable the aeroshell to survive the AGA maneuver given heat flux predictions.

6.2 Limitations and Uncertainties

CBAERO is a great engineering analysis software for understanding the aerothermal environment of general vehicle configurations. All CBAERO simulations are run with strictly laminar flow and the callout -nofree to eliminate assumptions made in the FMF regime. This eliminates excess heating in the low density regime when it does not exist, as collisions with molecules on the aeroshell are few but still significant enough to decrease the kinetic energy of the vehicle. Uncertainties in C_L should be expected at low density and high AoA. Higher C_D values are expected in the rarefied regime, so implementation

of two codes is required to accurately model the complete flight envelop.

A quality surface mesh is required for this solver to return accurate results, as it uses an independent panel method which integrates the streamlines over all panels. Accuracy limitations will arise from an unsymmetrical surface mesh of the aeroshell which affect computational results, but just meshing the half span geometry and reflecting the results across the y-axis proved to significantly help fluctuations seen in early computational studies. A fine mesh is required on the blunt nose leading edge of all aeroshells as this is the location of the stagnation region. As the AoA changes, the stagnation point will shift by the same amount, so this region of the vehicle needs sufficiently high mesh resolution around it. CBAERO selects a centroid of a single surface triangle as the stagnation point of the vehicle, which can cause fluctuations in heat flux if this assumed stagnation point ends up being on a node or edge of the surface mesh. If the stagnation point occurs at a node or edge of the mesh, the solver must pick the closet triangle, which can be pinpointed in the cbviewer interface when exploring the simulation results.

Convective heating estimates were significantly more uniform when using the -2d callout when compared to early simulations. This callout allows CBAERO to assume a 2D stagnation point along the leading edge of the aeroshell instead of attempting to find a single front most point on a spherical leading edge given the AoA. Even with the -2d command, CBAERO still recognizes a stagnation point to be a single panel of the aeroshell. The selection of the stagnation region and triangle on the mesh is what drives the convective heating correlations. This implies that predicted heating values will always have some degree of fluctuation depending on how the stagnation point shifts around the aeroshell OML as AoA changes until the solver is anchored to high fidelity results.

Radiation heating estimates from CBAERO have large fluctuations in the continuum regime, especially at the point of lowest altitude, highest density flight at case 3. While radiative heating would be critically relevant at this flight velocity and altitude, it accounts for more than half the total heat rate due to the solvers assumptions on the size of stagnation region. These estimate values cannot be accepted with confidence without being benchmarked with NEQAIR and anchored to high fidelity results. In discussion with Prabhu, radiation heating estimates provided by CBAERO seem high, as the subsonic bubble on the scale of these waverider configurations are not large and should cool off very quickly.

All computational results are estimates due to the mathematical assumptions made by the source code, but a limited number of high fidelity CFD solutions could be used to anchor the aerothermal behavior founds in CBAERO. By running a few CFD cases with similar free stream conditions, correction factors can be calculate for each surface triangle [34]. As CPU requirements are minimal for CBAERO, the anchoring process can reduce computational requirements with the interpolation of correction factors to the Mach, dynamic pressure, and AoA space resulting in close correlation with high fidelity models.

Chapter 7:

Conclusions and Future Recommendations

7.1 Conclusion

The elliptical configuration had the best aerothermal performance of all waverider configurations considered in this report. This aeroshell with a nose radii of $R_n = 0.1$ had the lowest C_D, which lead to the highest L/D performance at over 1.5. This peak performance occurred at an AoA above 5° through a value of 20°. The heat rate proved to be lower by more than 850 W/cm^2, with a value of roughly 5365 W/cm^2. Comparative convective heating rates were seen to be slightly higher for the elliptical configuration, but radiative and overall heating proved to be much less than all rectangular nose waverider configurations. While there was minimal differences between the performance of the rectangular waverider configurations, the wedgerider model had the best aerodynamic performance from an AoA of 5° to 15° and the strake model experienced lower heat flux values for the expected AoA along the reference trajectory.

As noted previously, the reference AGA trajectory assumes a constant L/D ratio of 1.5 and enables a transit time reduction of 7 years due to the achieved turn angle ϕ. While Henning's example AGA technology demonstration mission required a maximum vehicle L/D of 3.015 for effectiveness [12], a 7 year transit reduction with an aeroshell having a L/D ratio of 1.5 seems incredibly promising for scientific missions. However, the design of this reference trajectory should be crafted from understanding the dynamic aerothermal performance of the vehicle along the flight corridor. L/D is a critical optimization parameter for AGA aeroshell design, and will drive mission efficiency. Aeroshell sensitivities are critical to understand, as trade offs include balancing hypersonic aerodynamic performance while sustaining survivable heating conditions. Velocity can be maximized through efficient aerodynamic aeroshell design while TPS mass fractions can be lowered by minimizing the heat flux and total heat load throughout the AGA maneuver.

7.2 Recommendations for Future Work

The performance of additional waverider geometries should be considered in continued work on the subject. Other aeroshell models and design inspiration for waveriders should be explored or updates can be made on existing models. The wedgerider waverider model did not fully capture the benefits of a contracting wedge geometry due to the increased height of the conical sides, so this profile should be explored with The elliptical nose waverider proved to have the best aerothermal performance, so vehicle trim options like strakes or other novel configurations to improve lift should be explored. Additional waverider design inspiration from Lewis should be explored across concave and convex aeroshell variants. The performance of a waverider configuration that stems from a spherical nose with blunted leading edges should also be considered in tangent with elliptical nose configurations.

Future work with CBAERO can explore utilization of a smaller, more specific ADB across continuum flight regimes. This ADB was focused on capturing all points along the reference AGA trajectory. Conceptual limitations are present with CBAERO as it solves for streamline distributions over surface mesh panels, but this software has minimal computational requirements, is quite user friendly, and provides solid engineering level estimates. With further CBAERO analysis, the focus should narrow in on results for the continuum flight regime to closely check dependency on Mach, dynamic pressure, and AoA.

Access to high fidelity codes could enable anchoring of CBAERO data, and selecting a few points along the continuum flow regime could provide weighting to anchor a complete database. A full high fidelity model could be generated using both DSMC and CFD tools. This would enable proper aeroshell benchmarking and aerothermal anchoring to engineering estimates found by CBAERO.

To improve accuracy in aerodynamic performance results, tools can be used to splice the DSMC simulation space and continuum region. A bridging function can be applied to the coefficient of drag that blends continuum and FMF regimes, which would improve certainty for low density atmospheric flight along the trajectory. Two different high fidelity codes would be required to blend these regimes, but it would result in a smooth C_D distribution with altitude.

Results from this conceptual study indicate that Earth AGA could be feasible for rapid interplanetary transit, but this must be confirmed with high fidelity tools. Once high fidelity aerodynamic performance results are obtained, the AGA trajectory maneuver can be crafted from dynamic coefficient values in the ADB for a given waverider configuration. This analysis was performed for Earth's atmosphere, but it should be expanded to include Venus and Mars as these planets showed more benefits to the AGA trajectory maneuver. The aerothermal environment of the planet of interest will dictate entry and exit corridors that allow a successful AGA maneuver for a given waverider geometry. The aeroshells can then be dynamically flow through a reference trajectory of the specified planetary atmosphere to determine peak heat flux and total heat load for a desired trajectory, which enables selection of TPS material and sizing. Accurate prediction of the AGA environmental conditions avoids over designing or under designing TPS and enables aeroshell weight optimization while meeting mission requirements for thermal management. Once accurate entrance and exit criteria can be mapped for the given waverider geometry, the benefits of AGA trajectories for rapid interplanetary transit missions can be determined.

References

[1] NASA Office of Inspector General, "NASA's Management of the Artemis Missions," Office of Audits, November 2021, Report No. IG-22-003.

[2] Han, H., Li, X., and Qiao, D., "Aerogravity-assist capture into the three-body system: A preliminary design," *Acta Astronautica*, Vol. 198, 2022, pp. 26–35.

[3] Carroll, A., "Evaluation of Fast Transits to Trans-Neptunian Objects Using the Powered Jupiter Gravity Assist & Aerogravity Assist Techniques: Interplanetary Study," *Proceedings of the 21st International Planetary Probe Workshop (IPPW)*, Williamsburg, Virginia, June 2024, pp. 8–14.

[4] Randolph, J. E. and McDonald, A. D., "Solar System "Fast Mission" Trajectories Using Aerogravity Assist," *Journal of Spacecraft and Rockets*, Vol. 29, No. 2, Mar-Apr 1992, pp. 223–232, Jet Propulsion Laboratory, California Institute of Technology, Pasadena, California 91109.

[5] Johnson, W. R. and Longuski, J. M., "Design of Aerogravity-Assist Trajectories," *Journal of Spacecraft and Rockets*, Vol. 39, No. 1, Jan-Feb 2002, pp. 23–30.

[6] Armellin, R., Lavagna, M., Starkey, R. P., and Lewis, M. J., "Aerogravity-Assist Maneuvers: Coupled Trajectory and Vehicle Shape Optimization," *Journal of Spacecraft and Rockets*, Vol. 44, No. 5, Sep-Oct 2007, pp. 1051–1059.

[7] Lohar, F. A., Misra, A. K., and Mateescu, D., "Optimal Atmospheric Trajectory for Aerogravity Assist with Heat Constraint," *Journal of Guidance, Control, and Dynamics*, Vol. 18, No. 4, Jul-Aug 1995, pp. 723–730.

[8] Lu, Y. and Saikia, S. J., "Titan aerogravity-assist maneuvers for Saturn/Enceladus missions," *Acta Astronautica*, Vol. 176, 2020, pp. 262–275.

[9] Edelman, P. J. and Longuski, J. M., "Optimal Aerogravity-Assist Trajectories Minimizing Total Heat Load," *Journal of Guidance, Control, and Dynamics*, Vol. 40, No. 10, Oct 2017, pp. 2697–2701.

[10] Guo, S.-Q., Liu, W., Zhang, C.-A., Liu, Y., and Wang, F.-M., "Aerodynamic optimization of hypersonic blunted waveriders based on symbolic regression," *Aerospace Science and Technology*, Vol. 144, 2024, pp. 108801.

[11] Lewis, M. J. and McDonald, A. D., "Design of Hypersonic Waveriders for Aeroassisted Interplanetary Trajectories," *Journal of Spacecraft and Rockets*, Vol. 29, No. 5, Sep-Oct 1992, pp. 653–660.

[12] Henning, G. A., Edelman, P. J., and Longuski, J. M., "Design and Optimization of Interplanetary Aerogravity-Assist Tours," *Journal of Spacecraft and Rockets*, Vol. 51, No. 6, Nov 2014, pp. 1849–1856.

[13] Horvath, T. J., Berry, S. A., and Merski, N. R., "Hypersonic Boundary/Shear Layer Transition for Blunt to Slender Configurations – A NASA Langley Experimental Perspective," *RTO AVT Specialists' Meeting on "Enhancement of NATO Military Flight Vehicle Performance by Management of Interacting Boundary Layer Transition and Separation"*, NATO Research and Technology Organization, Prague, Czech Republic, Oct 2004, Published in RTO-MP-AVT-111.

[14] Adams, J. C., "Atmospheric Re-Entry," *Engineering Department at Purdue University*, 2003, Physics, Environmental Science, Engineering.

[15] Bertin, J. J. and Cummings, R. M., "Critical Hypersonic Aerothermodynamic Phenomena," *Annual Review of Fluid Mechanics*, Vol. 38, 2006, pp. 129–157.

[16] Park, S.-H., Neeb, D., Pilyushchev, G., Leyland, P., and Gülhan, A., "A study on heat flux predictions for re-entry flight analysis," *Acta Astronautica*, Vol. 187, Oct 2021, pp. 271–280.

[17] Anderson, J. D., *Hypersonic and High-Temperature Gas Dynamics, Second Edition*, American Institute of Aeronautics and Astronautics, 2006, AIAA Education Series.

[18] "Aerothermodynamic Course - Lecture Proceedings on Stagnation Point Heating, Distributed Heating and Trajectory Effects, Advanced Topics, and Thermal Protection Systems - TFAWS 2012," Online, 2012, Available at: https://tfaws.nasa.gov/TFAWS12/Proceedings.

[19] Tauber, M. E., "A review of high-speed, convective, heat-transfer computation methods," *NASA Technical Publication*, 1989, NASA Ames Research Center, Moffett Field, CA, USA. Publicly available technical report: NASA-TP-2914, A-89042, NAS 1.60:2914.

[20] Fadgyas, M. C., Pricop, M. V., Niculescu, M. L., Cojocaru, M. G., and Dumitrache, A., "Semi-empirical relations for pressure distributions in hypersonic regime," *AIP Conference Proceedings*, Vol. 1978, No. 370007, 2018, pp. 1–6.

[21] Anderson, J. D., Lewis, M. J., Kothari, A. P., and Corda, S., "Hypersonic waveriders for planetary atmospheres," *Journal of Spacecraft and Rockets*, Vol. 28, No. 4, Jul-Aug 1991, pp. 401–410.

[22] Lewis, M. J., "Osculating Cone Waveriders: A Flexible Methodology for Hypersonic Vehicle Design," Technical report, Department of Aerospace Engineering, University of Maryland, College Park, Maryland 20742, USA.

[23] Böhrk, H., Dittert, C., Weihs, H., Thiele, T., and Gülhan, A., "Sharp Leading Edge at Hypersonic Flight: Modeling and Flight Measurement," *Journal of Spacecraft and Rockets*, Vol. 51, No. 5, Sep 2014, pp. 1753–1760.

[24] Li, S., Wang, Z., Huang, W., Xu, S., and Yan, L., "Aerodynamic performance investigation on waverider with variable blunt radius in hypersonic flows," *Acta Astronautica*, Vol. 137, 2017, pp. 362–372.

[25] Lewis, M. J., "Sharp Leading Edge Hypersonic Vehicles in the Air and Beyond," *SAE Transactions*, Vol. 108, No. Section 1: JOURNAL OF AEROSPACE, 1999, pp. 841–851.

[26] Zhao, Z., Huang, W., Yan, L., and Yang, Y., "An overview of research on wide-speed range waverider configuration," *Progress in Aerospace Sciences*, Vol. 113, 2020, pp. 100666.

[27] Kinney, D. J., "Configuration Based Aerodynamics (CBaero)," NASA Ames Research Center, 2023, Release Type: U.S. Release Only. Reference Number ARC-15819-1. [Software]. Available: NASA Software Catalog.

[28] Kinney, D. J., Bowles, J. V., Yang, L. H., and Roberts, C. D., "Conceptual Design of a 'SHARP'-CTV," *35th AIAA Thermophysics Conference*, No. AIAA 2001-2887, American Institute of Aeronautics and Astronautics, Anaheim, California, Jun 2001, pp. 1–18.

[29] Kolodziej, P., Bowles, J., Brown, J., Cornelison, C., Lawrence, S., Loomis, M., Merriam, M., Rasky, D., Tam, T., Wercinski, P., Hodapp, A., Keese, D., Pilcher, M., Tucker, R., Bogdanoff, D., Chapman, G., Gage, P., Palmer, G., Venkatapathy, E., Bowling, D., Holt, D., and Yates, L., "SHARP-L1 Technology Demonstrator Development: An Aerothermodynamic Perspective," *34th AIAA Thermophysics Conference*, No. AIAA 2000-2687, Denver, CO, June 2000, pp. 1–13.

[30] Starkey, R. P., Reuster, J. G., Lewis, M. J., and Kolodziej, P., "Configurational Analysis of the SHARP-L1 Re-Entry Vehicle," *41st Aerospace Sciences Meeting and Exhibit*, No. AIAA 2003-1099, American Institute of Aeronautics and Astronautics, Reno, Nevada, January 2003, pp. 1–10.

[31] Parcero, K., Allen, G., Witkowski, A., McKee, S., and Torres, L., "Planetary Mission Entry Vehicles Quick Reference Guide Version 4.0," Special Publication 20220010761, Analytical Mechanics Associates; Databasis Engineering; Ames Research Center, August 2022.

[32] Nowlin, S. and Thimons, L., "Surviving the Heat: The Application of Phenolic Impregnated Carbon Ablators," *Conference Session B9, Paper #3131*, University of Pittsburgh, Swanson School of Engineering, 2013, pp. 1–10.

[33] Geuzaine, C. and Remacle, J.-F., "Gmsh: a three-dimensional finite element mesh generator with built-in pre- and post-processing facilities," *International Journal for Numerical Methods in Engineering*, Vol. 79, No. 11, 2009, pp. 1309–1331.

[34] Kinney, D. J., "Aerothermal Anchoring of CBAERO Using High Fidelity CFD," *AIAA Reno Conference*, American Institute of Aeronautics and Astronautics, Reno, NV, Jan. 2007, pp. 1–28, Conference Paper.

[35] LeBeau, G. J. and III, F. E. L., "Application highlights of the DSMC Analysis Code (DAC) software for simulating rarefied flows," *Comput. Methods Appl. Mech. Engrg.*, Vol. 191, 2001, pp. 595–609.

[36] "Data Parallel Line Relaxation Code (DPLR), Version 4," NASA Ames Research Center, 2023, Reference Number ARC-16021-1A. Release Type: U.S. Government Purpose Release. [Software]. Available: NASA Software Catalog.

[37] "NEQAIR v15.x, Nonequilibrium Radiative Transport and Spectra Program," NASA Ames Research Center, 2023, Reference Number ARC-15262-1B. Release Type: U.S. and Foreign Release. [Software].

[38] Allen, G., Wright, M. J., and Gage, P., "The Trajectory Program (Traj): Reference Manual and User's Guide," Tech. Rep. NASA/TM-2004-212847, NASA Ames Research Center, 2005.

[39] Sutton, K. and Randolph A. Graves, J., "A General Stagnation-Point Convective-Heating Equation for Arbitrary Gas Mixtures," NASA Technical Report NASA TR R-376, NASA Langley Research Center, Hampton, Va., Nov. 1971, L-7885, 117-07-01-01.

[40] Tauber, M. E. and Sutton, K., "Stagnation-point radiative heating relations for earth and Mars entries," *Journal of Spacecraft and Rockets*, Vol. 28, No. 1, 1991, pp. 40–42.

[41] Kinney, D. J., Garcia, J. A., and Huynh, L., "Predicted Convective and Radiative Aerothermodynamic Environments for Various Reentry Vehicles Using CBAERO," *44th AIAA Aerospace Sciences Meeting and Exhibit*, No. AIAA 2006-659, Reno, Nevada, January 9-12 2006.

[42] Kinney, D. J., "Aero-Thermodynamics for Conceptual Design," *42nd AIAA Aerospace Sciences Meeting and Exhibit*, No. AIAA 2004-31, Reno, Nevada, January 5-8 2004.

[43] Kinney, D. J., *CBAERO 4.1+ User's Manual*, NASA Ames Research Center, Moffett Field, California, September 2012, CBM-2008-9.

[44] NASA, "Design and Integration Tools: Genesis Flight Mechanics Simulation and Trajectory Design Tool v0.3.0," Johnson Space Center, n.d., MSC-27061-1.

[45] Masson, D. J., Morris, D. N., and Bloxsom, D. E., "Measurements of Sphere Drag from Hypersonic Continuum to Free-Molecule Flow," Research Memorandum RM-2678, The RAND Corporation, 11 1960.

[46] Gage, P., Prabhu, D., Allen, G., and Beerman, A., "Overview of Mission Sizing For Heatshield for Extreme Entry Environments Technology (HEEET) Materials," NASA Technical Memorandum HEEET-1004, Rev. A, NASA, 5 2014.

Appendix A:

Waverider Main Dimensions and Comparisons

Table A.1: Rectangular nose geometric dimensions

Parameter	$R_n = 0.1$	$R_n = 0.15$	$R_n = 0.2$	$R_n = 0.25$
Reference area (m^2)	11.09	11.674	12.263	12.861
Total chord (m)	4.9	4.95	5.0	5.05
Total span (m)	2.747	2.848	2.948	3.0488
Base height (m)	0.997	1.098	1.198	1.2988
Nose length (m)	0.09019	0.135	0.1804	0.2255
Centroid, (x,y,z)	(-3.023, 0.0156, 0)	(-2.9447, 0.014562, 0)	(-2.8794, 0.013724, 0)	(-2.823, 0.01301, 0)

Table A.2: Elliptical nose geometric dimensions

Parameter	$R_n = 0.1$	$R_n = 0.15$	$R_n = 0.2$	$R_n = 0.25$
Reference area (m^2)	10.535	11.04	11.55	12.066
Total chord (m)	4.895	4.943	4.991	5.039
Total span (m)	2.632	2.722	2.812	2.902
Base height (m)	0.9964	1.096	1.196	1.296
Nose length (m)	0.0954	0.1431	0.1909	0.2386
Shoulder length (m)	0.6954	0.743	0.791	0.8386
Centroid, (x,y,z)	(0.6374, 0.01593, 0)	(0.56254, 0.01497, 0)	(0.5029, 0.01416, 0)	(0.4516, 0.01349, 0)

Table A.3: Strake model geometric dimensions

Parameter	$R_n = 0.1$	$R_n = 0.15$	$R_n = 0.2$	$R_n = 0.25$
Reference area (m^2)	11.09	11.674	12.263	12.861
Total chord (m)	4.9	4.95	5.00	5.05
Total span (m)	2.747	2.848	2.948	3.0488
Base height (m)	1.124	1.098	1.198	1.2988
Nose length (m)	0.09019	0.135	0.1804	0.2255
Strake length	2028.33	2029.31	2029.31	2028.33
Centroid, m (x,y,z)	(-3.0057, 0.0239, 0)	(-2.9296, 0.02226, 0)	(-2.8659, 0.02086, 0)	(-2.81097, 0.01966, 0)

Table A.4: Wedgerider model geometric dimensions

Parameter	$R_n = 0.1$	$R_n = 0.15$	$R_n = 0.2$	$R_n = 0.25$
Reference area (m^2)	11.695	12.284	12.877	13.479
Total chord (m)	4.9	4.951	5.0	5.051
Total span (m)	2.998	3.099	3.200	3.301
Base height (m)	1.130	1.218	1.306	1.395
Flap length (m)	2.156	2.258	2.359	2.461
Flap wedge (m)	0.9538	0.947	0.9421	0.9384
Tail wedge (m)	0.7275	0.699	0.6714	0.6446
Centroid, m (x,y,z)	(-4.16, 0.03, 0)	(-4.05, 0.03, 0)	(-4.01, 0.03, 0)	(-3.95, 0.03, 0)

Table A.5: Waverider configurations with $R_n = 0.1\,m$

Configuration	**Reference area (m^2)**	**Total chord (m)**	**Total span (m)**	**Base height (m)**	**Nose length (m)**	**Centroid, (x,y,z)**
Rectangular	11.09	4.9	2.747	0.997	0.09019	(-3.023, 0.0156, 0)
Elliptical	10.535	4.895	2.632	0.9964	0.0954	(0.6374, 0.01593, 0)
Strake	11.09	4.9	2.747	1.124	0.09019	(-3.0057, 0.0239, 0)
Wedgerider	11.695	4.9	2.998	1.130	N/A	(-4.16, 0.03, 0)

Table A.6: Waverider configurations with $R_n = 0.15\,m$

Waverider configuration	**Reference area (m^2)**	**Total chord (m)**	**Total span (m)**	**Base height (m)**	**Nose length (m)**	**Centroid, (x,y,z)**
Rectangular nose	11.674	4.95	2.848	1.098	0.135	(-2.9447, 0.014562, 0)
Elliptical nose	11.04	4.943	2.722	1.096	0.1431	(0.56254, 0.01497, 0)
Strake model	11.674	4.95	2.848	1.098	0.135	(-2.9296, 0.02226, 0)
Wedgerider model	12.284	4.951	3.099	1.218	N/A	(-4.05, 0.03, 0)

Table A.7: Waverider configurations with $R_n = 0.2\,m$

Waverider configuration	**Reference area (m^2)**	**Total chord (m)**	**Total span (m)**	**Base height (m)**	**Nose length (m)**	**Centroid, (x,y,z)**
Rectangular nose	12.263	5.0	2.948	1.198	0.1804	(-2.8794, 0.013724, 0)
Elliptical nose	11.55	4.991	2.812	1.196	0.1909	(0.5029, 0.01416, 0)
Strake model	12.263	5.0	2.948	1.198	0.1804	(-2.8659, 0.02086, 0)
Wedgerider model	12.877	5.0	3.200	1.306	N/A	(-4.01, 0.03, 0)

Table A.8: Waverider configurations with $R_n = 0.25\,m$

Waverider configuration	**Reference area (m^2)**	**Total chord (m)**	**Total span (m)**	**Base height (m)**	**Nose length (m)**	**Centroid, (x,y,z)**
Rectangular nose	12.861	5.05	3.0488	1.2988	0.2255	(-2.823, 0.01301, 0)
Elliptical nose	12.066	5.039	2.902	1.296	0.2386	(0.4516, 0.01349, 0)
Strake model	12.861	5.05	3.0488	1.2988	0.2255	(-2.81097, 0.01966, 0)
Wedgerider model	13.479	5.051	3.301	1.395	N/A	(-3.95, 0.03, 0)

Appendix B:

Radiative heating velocity functions for Earth

Table B.1: Radiative heating velocity functions for Earth

$V, m/s$	$f_E(V)$
9000	1.5
9250	4.3
9500	9.7
9750	19.5
10000	35
10250	55
10500	81
10750	115
11000	151
11500	238
12000	359
12500	495
13000	660
13500	850
14000	1065
14500	1313
15000	1550
15500	1780
16000	2040